UNIVERSITÀ DEGLI STUDI DI TRIESTE

XXXI Ciclo di Dottorato in Fisica

Ab Initio Investigation of Self-Assembled Nanostructures for Catalytic Applications

PhD STUDENT:
Fatema Yahya Mohamed

PhD SUPERVISOR:
Prof. Maria Peressi

PhD COORDINATOR:
Prof. Livio Lanceri

Academic year 2017 - 2018

Acknowledgment

Firstly, I would like to give special thanks to my advisor, Prof. Maria Peressi, for the continuous support throughout my graduate studies. I am grateful for her patience, kindness, encouragement, and immense knowledge. Her guidance helped me in all the time of research and writing of this thesis.

My sincere thanks must also go to the whole experimental group at TASC Laboratory of IOM-CNR located in Trieste. In particular, I am grateful to the group leader Dr. Erik Vesselli and to also Manuel Corva for the close and continuous collaboration since the beginning of my PhD. Also, I am grateful to Dr. Nicola Seriani from the CMSP research group at ICTP, for the useful discussion and for being available all the time.

I am very grateful to my colleague and friend Virginia Carnevali, thanks for all of the support you have given me, and for all the fun we have had in the last four years. Also I sincerely thank all my friends at ICTP. In particular, Narjes Ansari and Sukanya Ghosh for the useful discussion and for their support when I was writing my PhD thesis.

Last but not the least, I would like to express my gratitude to my family: my mum, my sisters, and my brothers for supporting me spiritually throughout the period the PhD studies. It was their love and care that raised me up again when I got weary. Special thanks to my friends Onuorah Ifeanyi and Intisar Ahmed, thank you for listening, and being there whenever I needed a friend.

Abstract

This work is focused on the characterization of different nanostructures self-assembled on appropriate substrates and on the preliminary investigation of their potential catalytic performance using quantum mechanical simulations based on *ab-initio* Density Functional Theory. The investigation is carried on in close comparison with recent experimental data.

The systems under investigation include metallic platinum nanoclusters and hybrid ordered structures with organic molecules, assembled on regular 2D templates, which could prevent syntering and deactivation of the catalysts. The interaction of such nanostructures with carbon mono- and di-oxide molecules is addressed, studying in particular CO oxidation on platinum nanoclusters and CO_2 activation on organic molecules.

Firstly, the growth of platinum nanoclusters on different regions of the moiré pattern of graphene on Ir(111) is investigated: a stronger pinning of the graphene beneath and in the vicinity of the adsorbed clusters explains their higher stability in specific regions of the moiré, named *hcp*, from the registry of the center of the carbon hexagon of graphene with the underlying substrate. Remarkably, the steadiness of the metallic aggregates depends on their size: larger nanoclusters are more stable than very small ones (containing few atoms only), but this is not sufficient to guarantee their stability upon CO interaction. In fact, nanoclusters of about 20-30 atoms are affected by a deep restructuring under an increasing flux of the reactant [1].

Metal Phtalocyanines can be considered in a biomimetic approach to efficiently model single atom catalysts. The self-assembling of such molecules, in particular iron Phtalocyanines (FePcs) forms regular arrays of catalytically active single atoms at their centers. Efficient templates, in addition to the moiré pattern of graphene on Ir(111) previously mentioned, are oxide surfaces such as $Al_2O_3/Ni_3Al(111)$. The molecule-surface and molecule-molecule interactions induce a regular molecular array on this surface, with molecular vacancies forming a hexagonal lattice with the same periodicity of the substrate. For high molecular coverage, multilayers with the same structure but alternate chirality are formed, even before the completion of the first monolayer [2].

The self-assembled FePcs pattern can be controlled by dosing metal deposition on the $Al_2O_3/Ni_3Al(111)$ surface. In presence of Cu clusters, that likely fill the oxygen vacancies at the surface making the alumina surface potential smoother, the FePcs fully cover the oxide template and form uniform long range ordered structure with an almost square periodicity. The size of the Cu clus-

ters affects the structural stability of the molecular array. Scanning Tunneling Microscopy images show the presence of a few molecules with a dark protrusion at their center, not observed while depositing FePcs on the pristine oxide. The comparison between simulated and experimental images and energetic arguments suggest that they are demetalated phthalocyanines (Pc's) [3].

The catalytic activity of FePcs was exploited with respect to the interaction with CO_2. Tuning the chemical environment of FePc molecules, for instance oxidizing a graphene substrate, CO_2 can be activated through an electron transfer from the FePc [4].

In summary, this thesis shows that the atomic-scale study of nanostructured catalysts allow to understand the mechanisms governing their self-assembling and their activity, opening the way to a full control of their stability and performance.

Contents

Introduction

The aim of this thesis is to characterize different nanostructures self-assembled on appropriate substrates and investigate their potential catalytic performance, using quantum mechanical simulations and comparing them with experimental data. We considered in particular two different kinds of nanostructures: metallic platinum nanoclusters and hybrid ordered structures with organic molecules (iron phthalocyanines, FePc's) deposited on a regular template. I focus on the interaction of such nanostructures with carbon mono- and di-oxide molecules, studying in particular CO oxidation on platinum nanoclusters and CO_2 activation on organic molecules.

Nanoclusters are finite agglomerates consisting of a (few to large) number of atoms with size of a few nanometers [5]. These nanoclusters may consist of identical atoms of one or two or more different species. They exhibit important structural, electronic, and chemical properties which are distinct from those of individual atoms and molecules or bulk matter [6, 7].

The very high surface to volume ratio and the low coordination sites (as kinks, edges and steps) are primary reasons for the unique reactivity of metal nanclusters. Those unique properties make them very suitable for activating molecules for further processes, and opening reaction paths with lower reaction barriers.

Nanoparicles have unique properties, due to a very high active surface-to-volume ratio and high concentration of low coordination sites (kinks, edges and steps) that make them very suitable to activate molecules for further processes, opening reaction paths with low energy barriers [8]. Their catalytic activity can increases by decreasing the size. For selective catalytic applications, a uniform regular distribution of nanostructures with precise geometric shapes and size is extremely important. The use of appropriate support has a fundamental role for the growth of well-ordered pattern of metallic particles. In this work, both supported graphene and oxide templates were considered. In addition to act as catalytic centers, nanoclusters can be used to tune the self-assembly of organic molecules, which in turn act as a catalytic centers.

The present work is based upon Density Functional Theory (DFT) calculations using the Quantum ESPRESSO package. It is part of a joint theoretical/experimental investigation. The experimental work has been performed by the group leaded by Dr. Erik Vesselli and hosted at TASC Laboratory of IOM-CNR located in Trieste, where the structures have been grown and characterized using scanning tunnelling microscopy (STM), X-ray photoelectron spectroscopy

(XPS), and Sum-Frequency Generation (IR-Vis SFG) vibrational spectroscopy. Dr. Nicola Seriani (from ICTP) collaborated in the study of FePc molecules.

During the period of this thesis, I performed only the theoretical/numerical part of the joint investigation. The present written report includes also a detailed description of the experimental results at the beginning of each chapter, in order to facilitate the comparison between theory/experiment and the interpretation and rationalization of the results.

The PhD thesis is composed of five chapters: one for the computational approach, and the others for the results. Each of them, in turn, consists of three parts: an introduction, a summary of the experimental results, and a third part reporting our theoretical investigations and the comparison with the experiments.

Chapter 1 (*Computational Approach*). In this chapter I describe the theoretical method to calculate with atomistic quantum mechanical simulations of the electronic and structural properties of realistic systems, given their composition. In particular I describe the fundamental theorems of DFT which allow to find the ground state properties of a system. Then, I list and discuss some technicalities of the Quantum ESPRESSO code.

Chapter 2 (*Carbon Monoxide on Pt Nanoclusters Supported on Graphene*): In this chapter I investigate the adsorption of CO on Pt nanoclusters grown in a regular pattern on graphene/Ir(111). The growth of graphene on Ir(111) induces moiré structures and chemical corrugation of the graphene, due to the lattice mismatch with the underlying Ir substrate. The moiré pattern shows three distinct regions (named *HCP*, *FCC*, and *TOP* regions) resulting from different local configurations of the carbon network with the Ir substrate. Firstly, I characterize the moiré pattern of graphene on Ir(111). Then I study the adsorption of monomers and small clusters of different metals like Cu, Ir and Pt on the substrate. *FCC* and *HCP* regions are identified as preferential adsorption regions. I mainly focus on the growth details and binding mechanism and aggregation of Pt nanoclusters on the moiré structure of graphene.
After the characterization of the Pt nanoclusters, I study their interaction with carbon monoxide. I show the effect of the Pt size and morphology on CO adsorption, and the influence of the adsorbed molecule on the cluster.

Chapter 3 (*Iron Phthalocyanines on Alumina Film*). I investigate the self-assembled structure of FePc's on $Al_2O_3/Ni_3Al(111)$ substrate. The structure of a thin film of aluminum oxide (Al_2O_3) grown on $Ni_3Al(111)$ was determined in previous works [9–11]. The unit cell of the oxide film is hexagonal and contains some special sites giving rise to two ordered superstructures. One is the "dot" structure corresponding to a oxygen vacancy reaching the metal substrate, with the same periodicity of the oxide film. The other is the so-called "network" structure, with two additional sites per unit cell. I started by investigating the electronic and structural properties of a single molecule on different adsorption sites, extending the study to high molecular coverage. I show how the

molecule-substrate interaction governs the self-assembly of the molecular layer. Furthermore, I explore the details characterization of the monolayer and multilayers structure formed on the oxide template.

Chapter 4 (*Effect of Copper Clusters on the FePc Molecular Assemblies*). In this chapter I discuss the self-assembly of FePc molecules on Cu clusters adsorbed on Al_2 O_3 /$Ni_3Al(111)$ substrate. The site dependent adsorption of the molecule control the self assembly of the molecular layer. In this chapter I will show the possibility of tuning the formed molecular layer on pristine alumina, by pre-deposited Cu cluster on the alumina substrate.

Chapter 5 (*Binding of CO_2 on Iron Phthalocyanines*). In this chapter I investigate the catalytic performance of FePc molecules on CO_2 activation. The oxidation of graphene on the metal substrate through oxygen adsorption, and the impact of this process on CO_2 activation is described in this Chapter. I will demonstrate how the presence of oxygen in the system affects the electronic configuration of the FePc molecule, allowing the activation of CO_2 molecules.

Chapter 1

Computational approach

In this chapter we are going to describe in details how to calculate using computer the electronic properties of realistic system. One of the most widely used methods is the Density Functional theory (DFT). DFT allows to make specific predictions of experimentally observable phenomena for real materials and to design new materials.
We will initially present the basis concepts of the ab initio Density Functional Theory, in particular with the Kohn-Sham approach, which nowaday is the most used method in electronic structure calculations. Then, we will continue with the description of some computational details of Quantum ESPRESSO, a widely used, open source, state-of-the-art code for such kind of calculations.

1.1 The Born-Oppenheimer approximation

In this section, we consider the treatment of a system that consists of nuclei and electrons. The nuclei is considered as points in space at given coordinates, these points has a mass and charge. One of the tool to determine the properties of electrons around the nuclei is the quantum theory. Our system is made of a number of nuclei (N_I), each nucleus has charge ($Z_I e$) and mass (M_I), and numbers of electrons with charge -e and mass m. The hamiltonian H of this system can be written as:

$$H = T_e(\{\mathbf{p}\}) + T_n(\{\mathbf{P}\}) + W_{ee}(\{\mathbf{r}\}) + W_{NN}(\{\mathbf{R}\}) + W_{eN}(\{\mathbf{r}\}) \tag{1.1}$$

where T_e and T_N are the kinetic energies of electrons and nuclei respectively, V_{ee} is the electron-electron interaction, V_{eN} the electron-nucleus interaction and V_{NN} the nucleus-nucleus interaction. We notice that $\{\mathbf{r}\}(\{\mathbf{R}\})$ and $\{\mathbf{p}\}(\{\mathbf{P}\})$ is a compact way to write all the coordinates and momenta of electrons (nuclei). Considering the electrostatic interation and neglecting any relativistic term, we can write the various terms in H as:

$$T_e(\{\mathbf{p}\}) = \sum_{i=1}^{N} \frac{p_i^2}{2m} \quad , \qquad T_N(\mathbf{P}) = \sum_{I=1}^{N_I} \frac{P_I^2}{2M_I} \tag{1.2}$$

$$V_{ee}(\mathbf{r}) = \frac{1}{2} \sum_{i \neq j} \frac{e^2}{|\mathbf{r}_i - \mathbf{r}_j|} \quad , \qquad V_{NN}(\mathbf{R}) = \frac{1}{2} \sum_{I \neq J} \frac{Z_I Z_J e^2}{|\mathbf{R}_I - \mathbf{R}_J|} \tag{1.3}$$

$$V_{eN}(\mathbf{r},\mathbf{R}) = \frac{1}{2}\sum_{i=1}^{N}\sum_{I=1}^{N_I}\frac{Z_I e^2}{|\mathbf{r}_i - \mathbf{R}_I|} \tag{1.4}$$

Solving the Schrödinger equation, $H\Psi_{tot} = E_{tot}\Psi_{tot}$, associated to H is in general very complicated. If the system evolves in a way that no energy exchange between electrons and nuclei takes place, then the dynamics of nuclei and that of electrons can be handled separately according to the Born-Oppenheimer approximation. The use of this approximation is made possible by the fact that nuclei have a much larger mass than the electrons (about 1836 times heavier). In this way it is possible to write an electronic hamiltonian H_{el} that depends only on the electron coordinates and has the nuclei positions as parameters. The eigenvalues problem to be solved becomes now:

$$H_{el}\Psi_{tot}(\{\mathbf{r}\};\{\mathbf{R}\}) = E_{tot}(\{\mathbf{R}\})\Psi_{tot}(\{\mathbf{r}\};\{\mathbf{R}\}) \tag{1.5}$$

where

$$H_{el} = T_e + V_{ee} + V_{eN} + V_{NN} \tag{1.6}$$

The energy $E(\{\mathbf{R}\})$, which is a *potential energy surface* in a high-dimensional space, is responsible of the dynamics of nuclei.
Forces F_I on the atoms I are calculated as quantum mechanical expectation values of the spatial derivatives of the Hamiltonian using the theorem of Hellmann-Feynman [12], from the relation:

$$F_I = \frac{\partial E(\{\mathbf{R}\})}{\partial \mathbf{R}_I} = -<\Psi(\{\mathbf{r}\};\{\mathbf{R}\})\left|\frac{\partial H_{el}}{\partial \mathbf{R}_I}\right|\Psi(\{\mathbf{r}\};\{\mathbf{R}\})> \tag{1.7}$$

1.2 Density functional Theory

Solving the Schrödinger Equation (1.5) for N interacting electrons is a formidable task, and it needs further simplification to be handled in an effective way. Different methods have been proposed in order to solve this problem. Nonetheless, Density functional Theory (DFT) is till one of the most used and powerful in ab-initio calculations. The DFT reduces the problem of many interacting electrons to a problem of independent electrons in an effective potential. In this way the dimensionality of the problem is reduced from the original $3*N$ space variables (N number of electrons) to 3. DFT is based on the theorems by Hohenberg and Kohn in 1964 [13] and on the Kohn-Sham equations in 1965 [14].

1.2.1 The Hohenberg-Kohn (HK) Theorems

The theorems of Hohenberg and Kohn have general validity for a many-particle system with arbitrary interaction and in particular for the electron gas with Coulomb interaction in an external potential originating from the atomic nuclei. The theory is based upon two theorems.

(i) **The HK theorem I**:

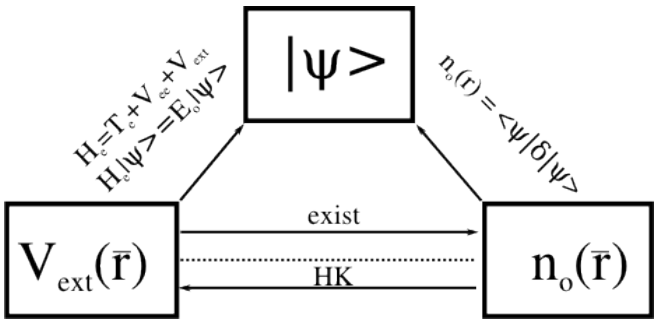

Figure 1.1: Schematic diagram of the first Hohenberg-Kohn theorem. From the usual solution of the Schrödinger equation it is evident that we can determine the many body wave function (Ψ) once we know the external potential V_{ext}, Then we can also $n_o(\mathbf{r})$. the ground state density $n_o(\mathbf{r})$ determines the V_{ext} in a unique way and this goes under the name of Hohenberg-Kohn (arrow labeled "HK")) [13].

For any system of interacting particles in an external potential V_{ext}, this potential is determined uniquely by the ground state density $n_0(\mathbf{r})$, a part from a constant.

(ii) **The HK theorem II**:

For any external potential V_{ext}, it is possible to define the energy of the system as a functional of the density $n(r) : E = E[n(r)]$.
Morever, the ground state energy of the system is the minimum value of this functional and the density that minimizes it, keeping the number of electrons N constant, is the ground state density $n_0(r)$. Let us now consider again the electronic hamiltonian given in Equation (1.6) putting $V_{eN} = V_{ext} = \sum_i v_{ext}(\mathbf{r}_i)$. Then we can write the functional as:

$$E[n] = F[n] + \int d\mathbf{r} v_{ext} n(\mathbf{r}) + E_{NN} \tag{1.8}$$

where $F[n] = T_e[n] + V_{ee}[n]$ is a functional independent from V_{ext} and common to every interacting electronic system.
In principle all ground state properties are determined from the minimization of the functional $E[n]$. The main issue in this approch is that the Hohenberg-Kohn theorems don't give any prescription for the explicit determination of the universal functional $F[n]$.
This problem can be solved by using the approach of **Kohn-Sham** [14], that is the method actually used in electronic structure calculations.

1.2.2 Kohn-Sham (KS) approach

The idea of Kohn and Sham is to replace the many-body system of interacting electrons with a more easily soluble auxiliary system.
To do this, Kohn and Sham assumed that the ground state density of the original system is equal to that of some non-interacting system. Then, the energy functional in Equation (1.8) can be written in the form:

$$E[n] = T_s[n] + \int dr v_{ext}(r) n(\mathbf{r}) + E_{Hartree}[n] + E_{NN} + E_{xc}[n] \tag{1.9}$$

where $T_s[n]$ is the kinetic energy functional of the auxiliary system and $E_{Hartree}[n]$ is the classical Coulomb interaction energy of the electron density $n(r)$ interacting with itself and can be written as:

$$E_{Hartree}[n] = \frac{e^2}{2} \int d\mathbf{r} d\mathbf{r'} \frac{n(\mathbf{r})n(\mathbf{r'})}{|\mathbf{r}\text{-}\mathbf{r'}|} \tag{1.10}$$

All many-body effects of exchange and correlation are grouped into the exchange-correlation energy $E_{xc}[n]$, which is defined as:

$$E_{xc}[n] = T[n] - T_s[n] + V_{ee}[n] - E_{Hartree}[n] \tag{1.11}$$

For the system of $N = N^{\uparrow} + N^{\downarrow}$ independent electrons, the ground state is obtained filling each of the N^{σ} one-electron orbitals $\Psi_i^{\sigma}(\mathbf{r})$ with the eigenvalues of the auxiliary hamiltonian (σ is the spin variable). The density in this case is:

$$n(\mathbf{r}) = \sum_{\sigma=\uparrow,\downarrow} n^{\sigma}(\mathbf{r}) = \sum_{\sigma=\uparrow,\downarrow} \sum_{i=1}^{N^{\sigma}} |\Psi_i^{\sigma}(\ \mathbf{r})|^2 \tag{1.12}$$

and

$$T_s[n] = \frac{1}{2} \sum_{\sigma=\uparrow,\downarrow} \sum_{i=1}^{N^{\sigma}} |\overrightarrow{\nabla} \Psi_i{}^{\sigma}(\mathbf{r})|^2 \tag{1.13}$$

To obtain the Schrödinger-like equations governing the orbitals of the auxiliary system, we proceed minimizing Equation (1.9) with respect to the density $n^{\sigma}(\mathbf{r})$. This leads to the Kohn-Sham equations:

$$H_{KS}^{\sigma} \Psi_i{}^{\sigma}(\mathbf{r}) = \epsilon_i{}^{\sigma} \Psi_i{}^{\sigma}(\mathbf{r}) \tag{1.14}$$

where

$$H_{KS}^{\sigma} = -\frac{\hbar^2}{2m} \nabla^2 + v_{eff}^{\sigma}(\mathbf{r}) \tag{1.15}$$

and

$$v_{eff}^{\sigma}(\mathbf{r}) = v_{ext}(\mathbf{r}) + e^2 \int d\mathbf{r'} \frac{n(\mathbf{r'})}{|\mathbf{r}\text{-}\mathbf{r'}|} + v_{xc}^{\sigma}[n] \tag{1.16}$$

The last term $v_{xc}^{\sigma}[n]$, that includes all the non classical electron interactions, is defined as:

$$v_{xc}^{\sigma}[n] = \frac{\delta E_{xc}[n]}{\delta n^{\sigma}(\mathbf{r})} \tag{1.17}$$

Then we have reduced the interacting many body problem to the computation of independent-particle in Equation (1.14) which must be solved self-consistently with the resulting density Equation 1.12.
Untill this point no approximations have been done, hence if we knew the exact functional $E_{xc}[n]$, the Kohn-Sham equations would leed to the exact ground state density and to the energy Equation (1.9) for the interacting system.

1.2.3 Exchange-correlation (XC) functional

The KS equations successfully maps the original interacting many-body system onto a set of independent single-particle equations and makes the problem much easier. In the meantime, without knowing the exact form of the XC energy functional $E_{xc}[n]$, the KS equations are unsolvable. There are approximate formulae for it which are fitted to Quantum Monte Carlo data for the electron gas [15]. These formulae are obtained within certain approximations; the most popular is the Local Density Approximation (LDA), which is based on the hypothesis that the local XC contribution to the energy is a function only of the electron density in that point. In this case, we express the XC energy as if it was simply equal at each point in space to the XC energy density of an homogeneous electron gas:

$$v_{xc}(\mathbf{r}) = \frac{\delta E_{xc}[n]}{\delta n(\mathbf{r})} = \int f_{XC}^{LDA}(n(\mathbf{r}))n(\mathbf{r})d\mathbf{r} \tag{1.18}$$

where f_{XC}^{LDA} is the LDA functional, using f_{XC} that are exact for a homogeneous electron gas (HEG). LSDA gives very good results, for a system with uniform or slowly varying densities and, remarkably, gives also good results for systems with rapidly varying densities, such as surfaces.
Another approach is the Generalized Gradient Approximation (GGA), which writes the local XC contribution to the energy as a function of the density in that point and its derivatives with respect to space coordinates. In the present work the exchange-correlation energy and potentials have been calculated within GGA in the formulation by Perdew, Burke and Ernzerhof (PBE [16]).

1.2.4 Solving Kohn-Sham Equations

To find the ground state of the system under investigation, the KS equations must be solved consistently because the effective potential presented in the KS equations (Equation 1.16) and the electron density $n(r)$ are closely related. This is usually done numerically through some self-consistent iterations as shown in Figure 1.2. The process starts with an initial guess of the electron density, usually a superposition of atomic electron density, then the effective KS potential is calculated and the KS equation is solved with single-particle eigenvalues and wavefunctions, a new electron density is then calculated from the wavefunctions.
After this, the self-consistent conditions can be the change of total energy or electron density from the previous iteration or total force acting on atoms is less than some chosen small quantity, or a combination of these individual conditions.
If the self-consistency is not achieved, the calculated electron density will be mixed with electron density from previous iterations to get a new electron density. A new iteration will start with the new electron density.
This process continues until self-consistency is reached. After the self-consistency is reached, various quantities can be calculated including total energy of the system, Hellmann-Feynman forces, stress, electron Density of States (DoS) etc..

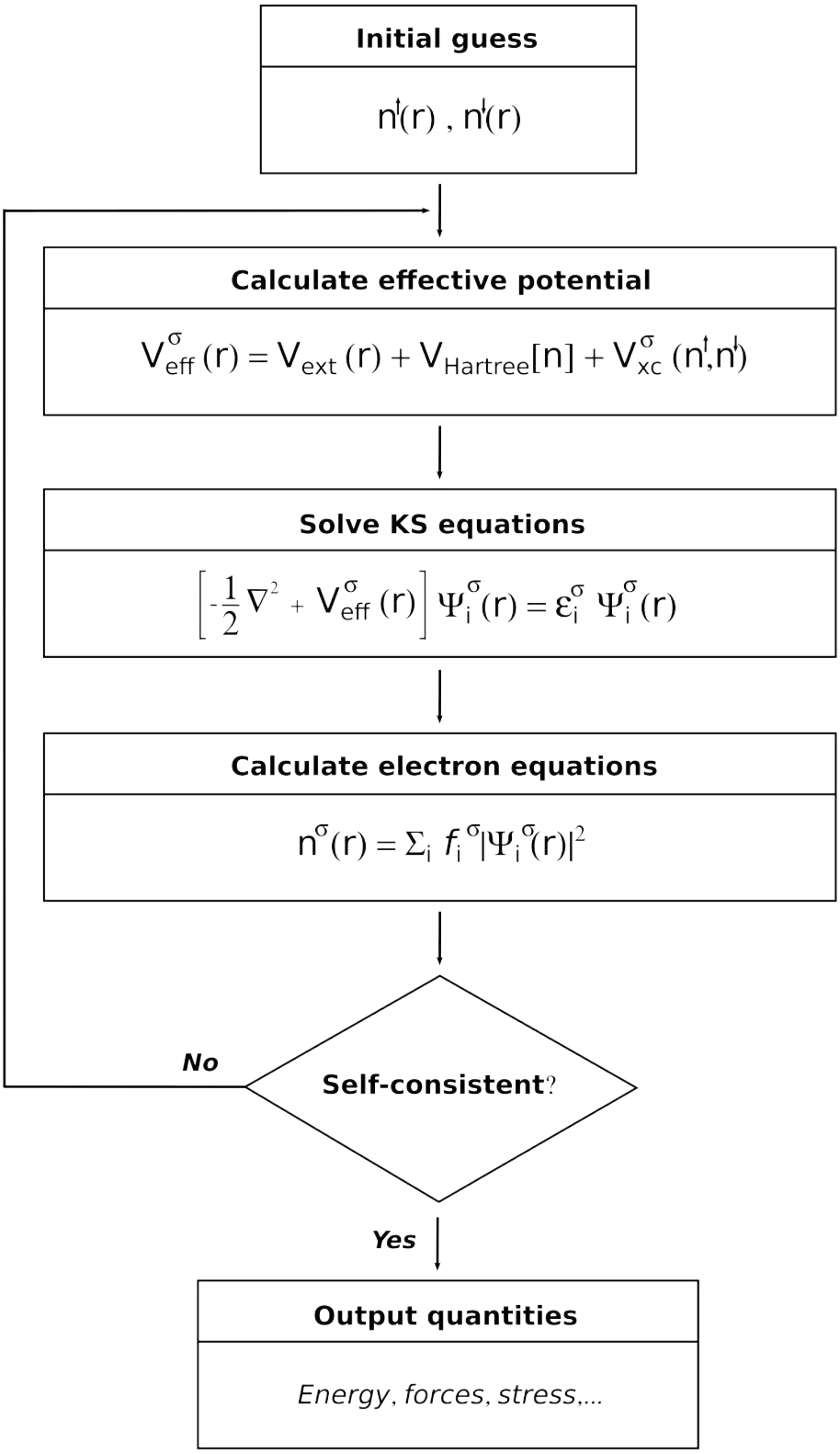

Figure 1.2: Schematic diagram of the self-consistent loop for the solution of the KS equations [20].

1.2.5 DFT+U method

For a few systems such as magnetic oxides of the 3d transition metals, the usual Density Functional approximations even in the spin-polarized versions fail to give the correct prediction for the ground state. For instance, Local Spin Density Approximation (LSDA) approaches predict FeO to be metallic ground state, instead the ground state is known to be an insulator [17]. The reason of these failures has been found to be the inability of these simple DFT schemes to take into account the strong interactions (strong on site Coulomb repulsion) between very localized d-states [18, 19], because of the orbital-independent potentials in L(S)DA and GGA approximations.
In order to properly describe these strongly correlated systems, orbital-dependent potentials should be used for d electrons. One of the method to incorporate the strong electron-electron correlations between d electrons is to add a term into the Hamiltonian which takes explicitly into account these interactions. This approach is called LDA+U or GGA+U, according to the approximation used for exchange and correlation.
The main idea of LDA+U is to separate electrons into two subsystems: the delocalized s and p electrons which could be described by using an orbital-independent one-electron potential GGA (LDA), and the localized d or f electrons for which the Coulomb d−d interactions should be taken into account, by using an orbital dependent term. the Hamiltonian of the system can be written in slightly different forms, one of which is [17]:

$$E^{LDA+U} = E^{LDA} + \sum_I \left[\frac{U}{2} \sum_{m,\sigma \neq m',\sigma'} n_m^{I\sigma} n_{m'}^{I\sigma'} - \frac{U}{2} n^I (n^I - 1) \right] \tag{1.19}$$

where n is the atomic orbital occupation, I refer to the ion, m is the orbital, σ for the spin. The U term (Hubbard term) [17] mimics the strong correlation between d-electrons and the interaction is designed to favour integer occupation numbers of the d-orbitals. This correction forces the system towards integer occupancies, which leads to the opening of the HOMO/LUMO gap in insulators. The Hubbard term is usually added only to the atomic species that need a correction.
The only difficulty in this method is the actual choice of the U parameter. It is possible to calculate it in a self-consistent way [17]. In ref [29] a Hubbard parameter $U = 3.7\ eV$ was chosen, in order to reproduce experimental photoemission spectra of FePc molecules by Brena et al. [30]. In our work, we have chosen values of U between 1 and 4 eV to see how strongly the results deviate from those of the simple spin-paired DFT-GGA and to correctly reproduce the experimental STM images, without pursuing a self-consistent treatment (see chapter 3, 4, and 5 for more details).

1.3 Vibrational frequencies

Phonons in crystals [31] are extended vibrational modes, propagating with a wave-vector $\mathbf{q}$. They are characterized by a vibrational frequency $\omega(\mathbf{q})$ and by the displacements of the atoms. The $\mathbf{q}$ wave-vector is the equivalent of the

Bloch vector for the electronic states and is inside the first Brillouin zone. For a system with N atoms in the unit cell, there are $3N$ phonons for a given $\mathbf{q}$. The dynamical matrix contains information on the vibrational properties of a crystal.

It is possible to derive the vibrational frequencies associated with the deviations of the ions from their equilibrium positions using Density Functional Perturbation Theory (DFPT) [32, 33]. The perturbation is induced by small displacements of the nuclei from their equilibrium positions, which result in changes in the external potential V_{ext} , the wave functions of the KS equations and hence the electron charge density. Second-order perturbation of DFT total energy is obtained by expanding the DFT total energy with respect to the changes in the wave functions to first order and external potentials up to second order. Details of calculations are shown in [33]. The dynamical matrix for periodically repeated system is defined as:

$$D_{ij}(\mathbf{q}) = \sum_{R'} e^{-i\mathbf{q}.\mathbf{R}} \frac{\partial^2 E}{\partial u_i(\mathbf{R}+\mathbf{R}')\partial u_j(\mathbf{R})} \tag{1.20}$$

The dynamical matrix contains information on the vibrational properties of a crystal: phonon frequencies are the square roots of its eigenvalues, while the atomic displacements $u(\mathbf{R})$ are related to its eigenvectors. The dynamical matrix is calculated with respect to $u(\mathbf{R})$ for each atom in each direction ($i, j = 1, 2, 3$, corresponding to x, y and z directions), and then by solving the equation

$$D(\mathbf{q})\vec{\varepsilon} = M\omega_{\mathbf{q}}^2\vec{\varepsilon} \tag{1.21}$$

which gives the phonon frequencies $\omega_{\mathbf{q}}$ of the phonon's with wave vector $\mathbf{q}$, where M is a diagonal matrix with the atomic masses.

1.4 Quantum ESPRESSO suite of codes

Ab initio calculations are principally based on DFT within the Kohn-Sham scheme.
We will use Quantum ESPRESSO (opEn Source Package for Research In Electronic Structure, Simulation, and optimization) [21]), which is a suite of codes based on pseudopotentials to represent the electron-ion interactions and using plane waves (PWs) as basis set for the expansion of the KS orbitals.
The basic computations that Quantum ESPRESSO (QE) can perform are:

- calculation of the ground state energy of the system through the self consistent solution of the KS equations
- structural optimizations of the atomic coordinates using Hellmann-Feynman force (structures were optimized by carrying out ionic relaxation using Broyden-Fletcher-Goldfarb-Shanno (BFGS) method).

In addition, several utilities for data-processing are available, allowing e.g. to calculate the Density of States (Dos), Scanning Tunneling Microscopy (STM) images, Lowdin charges, Planar averages, etc..
Now we are going to describe some of the computational details that characterize the QUANTUM ESPRESSO code.

Pseudopotentials

The main idea underneath the concept of pseudopotentials (PPs) is the replacement of one problem with another.
Since core states don't contribute in a significant manner to chemical bonding and to solid-state properties, it is reasonable to assume that these states are frozen near the atomic nuclei (frozen core approximation).
The problem is solved considering a new system composed only by valence electron that interact with ionic cores (nuclei+core electrons) through some effective potential. The fundamental step in the PPs theory consists in constructing new *Pseudo*potentials so as to reproduce in the more possible accurate way the true behavior of the valence electrons. The PPs have to replace the divergent Coulomb potential near the nuclei with a fictitious softer one due to the ionic cores. So that solving the new KS equations with the pseudopotential(PP), results in the wave-functions that are smoother than the true ones near the nuclei and without wiggles that would be caused by the condition of orthonormality with the core states.
This approach is useful, because it reduces the number of plane waves on which it is necessary to expand the valence states and decreases the computational cost of the calculation.
There are several classes of PPs. The Norm-conserving Pseudopotentials (NCPPs) [22] are constructed from all the electrons in the atom. For number of atoms (e.g. Oxygen, Nitrogen and the 1st row transition metals) these NCPPs are still hard, and they need plane waves with large wave vector to be well described.
For this purpose Vanderbilt [23] developed a new type of PPs, termed ultrasoft (US), that are much softer in the core region than NCPPs. In our work we used Vanderbilt ultrasoft PPs with PBE exchange-correlation functional. Example of USPP is shown in Figure 1.3.

Plane Wave Basis Set

Many electronic structure codes including Quantum ESPRESSO use periodic Boundary Conditions (PBC) that are the natural Boundary Conditions for the description of periodic systems, such as crystals. The use of PBC is also convenient for the implementation of PWs as basis set.
The periodicity is given by the dimensions of the simulation cell and, as a consequence, the Bloch theorem is valid also for non-periodic systems, such as surfaces, because this type of systems can be inserted in properly chosen supercells.
In this way it is possible to write the KS orbitals of Equation 1.14 as

$$\Psi_{i,\mathbf{k}}(\mathbf{r}) = \sum_{G} C_{i,\mathbf{k}+\mathbf{G}} \Phi_{\mathbf{k}+\mathbf{G}}(\mathbf{r}) \tag{1.22}$$

where the $\Phi_{\mathbf{k}+\mathbf{G}}(\mathbf{r})$ are PWs of the form:

$$\Phi_{\mathbf{k}+\mathbf{G}}(\mathbf{r}) = \frac{1}{\sqrt{V}} \exp^{i(\mathbf{k}+\mathbf{G}).\,\mathbf{r}} \tag{1.23}$$

where, V is the volume of the simulation cell, $\mathbf{k}$ is a Bloch vector in the first Brillouin Zone (BZ), $\mathbf{G}$ is a vector of the reciprocal lattice and i is a band index.

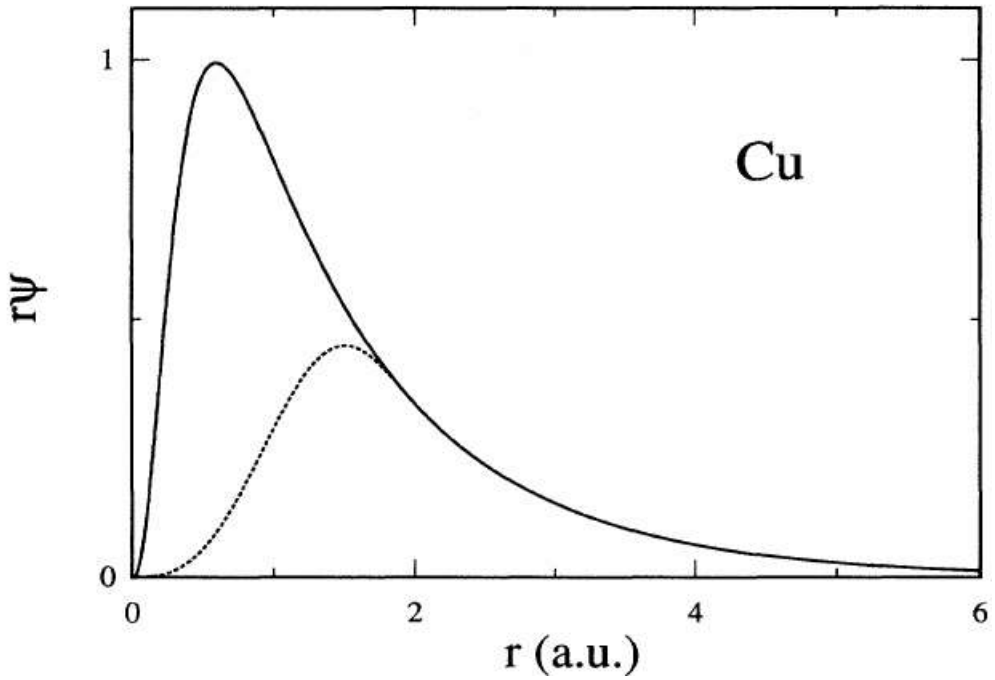

Figure 1.3: All-electron(solid) and Pseudo (dashed) radial wave functions of the 3d orbital of Cu. [24]

At this point, it is evident that PWs are the simplest basis set on which we can expand the eigenstates of H_{KS}, and that they allow to transform the KS equations in a matrix diagonalization problem given by:

$$\sum_{\mathbf{G}} (< \Phi_{\mathbf{k+G}} | H_{KS} | \Phi_{\mathbf{k+G}} > - \epsilon_{i,\mathbf{k}} \delta_{\mathbf{G},\mathbf{G}}) C_{i,\mathbf{k+G}} = 0 \tag{1.24}$$

The number of PWs in a real calculation cannot be infinite in Equation 1.22 and is fixed imposing a kinetic energy cutoff (for analogy with the free electron case) by means of the parameter E_{cut}:

$$\frac{\hbar^2 |\mathbf{k+G}|^2}{2m} < E_{cut} \tag{1.25}$$

The convergence of the results to the true values is controlled in a simple way by this parameter: the larger is E_{cut}, the better the accuracy. The periodic repetitions of the simulation cell due to the PBC can give rise to unwanted interactions of the system with its periodic images, that can be minimized using large enough supercells, but at the expense of an increasing computational cost (with PW basis set empty space is treated equally to the regions of interest).

Brillouin Zone Sampling

During the self-consistent process for the solution of KS equations, quantities such as the electron density have to be calculated by means of an integration over the **Brillouin Zone**:

$$n(\mathbf{r}) = \frac{V}{(2\pi)^3} \sum_{\sigma} \sum_{i} \int_{B.Z.} d\mathbf{k} \; f_{i,\mathbf{k}} |\; \Psi_{i,\mathbf{k}}(\mathbf{r})|^2 \tag{1.26}$$

where $f_{i,\mathbf{k}}$ is the occupation number of the state, $\Psi_{i,\mathbf{k}}$ and the sum in i is over the bands.
The integration is carried out exploiting the so-called special $\mathbf{k}-$points method [25, 26] that allows to approximate the integral with a sum over few properly selected k-points.
In our calculation we will use the method of Monkhorst and Pack [27] where the special $\mathbf{k}-$points are chosen in a uniform grid and then the number can be easily scaled with the dimension of the simulation cell (the size of the BZ is inversely proportional to the size of the simulation cell).

1.4.1 DoS and STM imaging

A useful post processing quantity that can be calculated with QE is the DoS, which provides a counting of the states with energy E:

$$\mathrm{DoS}(E) = \int_{B.Z.} d\mathbf{k}\ \delta(\epsilon(\mathbf{k}) - E) \tag{1.27}$$

where $\epsilon(\mathbf{k})$ is a generic eigenvalue of the KS equations seen as a function of $\mathbf{k}$.
To understand the character of the bonds between different atoms, or to understand the distribution of the electrons in the system it is useful to introduce a quantity that gives information also in the real space. This is the Projected Density of States (PDoS):

$$\mathrm{PDoS}(\alpha, E) \propto \int_{B.Z.} d\mathbf{k}\ |< \Phi^{at}_{\alpha} |\ \Psi_{\mathbf{k}} >|^2\ \delta(\epsilon(\mathbf{k}) - E) \tag{1.28}$$

where Φ^{at}_{α} is the atomic orbital with quantum number α centered on the atom of interest. Another important quantity that is used for the simulation of the STM images is the Integrated Local Density of States (ILDoS):

$$\mathrm{ILDoS}(\mathbf{r}) = \int_{B.Z.}^{\epsilon_F + V_{bias}} dE\ \mathrm{LDoS}(\mathbf{r}, E) \tag{1.29}$$

and

$$\mathrm{LDoS}(\mathbf{r}, E) = \int_{B.Z.} d\mathbf{k}\ |\Psi_{\mathbf{k}}(\mathbf{r})|^2\ \delta(\epsilon(\mathbf{k}) - E) \tag{1.30}$$

where ϵ_F is the Fermi energy of the system and V_{bias} represents the electrostatic potential energy difference between the tip of the microscope and the sample. In the Tersoff-Hamann approximation [28], where the tip is modeled as a spherical potential well and only the s-wave solution is considered, it is possible to demonstrate that the tunneling current I between the tip and the sample is proportional to the ILDoS:

$$I \propto ILDoS(\mathbf{r}) \tag{1.31}$$

There are two different types of STM images that can be realized: one is termed at constant-height and the other at constant-current.
A constant-height STM image is simulated, first fixing the value of the height z of the tip above the sample, and then calculating, for each point in a grid in the xy plane of the sample, the corresponding value of the ILDoS.
On the contrary, a constant-current STM image can be constructed, first fixing

the value of the current I and so defining an ILDoS isosurface in the three-dimensional space, and then searching, for each point in a grid in the sample plane, the corresponding value of the height z that meets the chosen isosurface (see Figure 1.4). In our work we will simulate constant-current images.

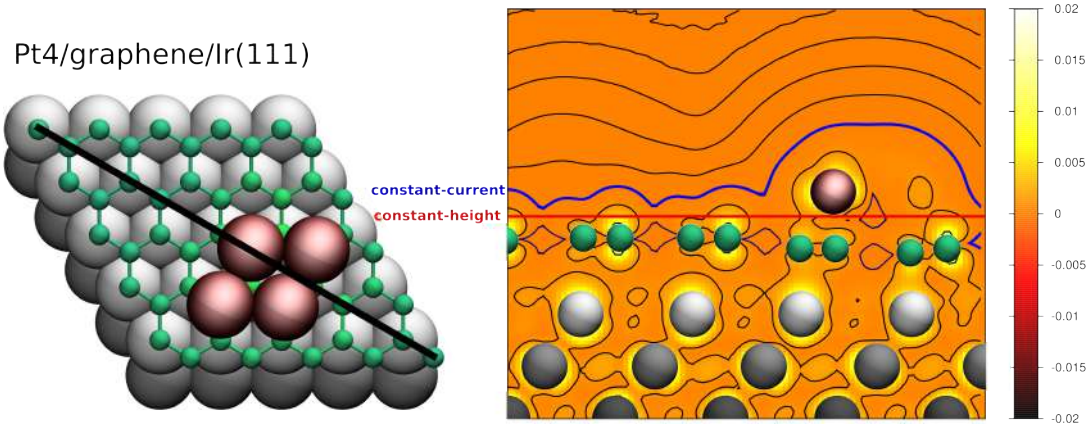

Figure 1.4: Left side Is the top view for 4 Pt atoms adsorbed on graphene/Ir(111), solid black line is the direction of the cut for which ILDos (right side) was sketched. **Right panel** ILDoS isosurfaces ($V_{bias} = 0.20\ eV$) on a plane perpendicular to the surface of the system. There are two ways to simulate STM images: at constant-height where the value of the height z is fixed (solid red line) and at constant-current where the value of the ILDoS isosurface is fixed (solid blue line). For the latter case (the one used in our work) the algorithm searches the chosen isosurface starting, for each point in the xy plane grid, from high z values and then going to lower z values until the chosen isovalue is found (black arrows).

Chapter 2

CO on Pt nanoclusters supported on graphene

2.1 Introduction

The peculiar properties of metal nanoclusters are used to study the catalytic oxidation of different molecules [34]. In the case of Pt, the concave sites are found to be most active sites for the oxygen reduction, while isolated single Pt atoms play an important role in CO oxidation and in water−gas shift reactions [35, 36]. Moreover, it is shown that few Pt nanoparticles supported on SnO and Al_2O_3 show highly active and selective catalysts for the oxidation of propane [6].

One of the interesting scientific and technological challenges associated with the use of nanoclusters as catalysts is understanding the role of the composition and atomic-scale structure of those nanoclusters in producing the best catalytic activity. Another challenge is to synthesize these particles with maximum control over the composition and structure. A promising strategy in this direction is to use a template that would help in growing regular arrays of nanoclusters. Regular arrays of supported clusters are more preferable than the random ones, because the identical environment of each cluster (e.g. distances from their neighbors) produces a uniform response to external stimulation.

Metal nanoclusters can be grown on a support like oxide films or carbon derivatives (such as: amorphous carbon, graphite, and graphene). Acommon problem in the use of clusters as catalysts is that one has to work with low cluster densities to avoid coalescence of randomly arranged clusters. The cluster bonding to the substrate should be strong enough to warrant their stability at the temperature of operation and at the same time weak enough not to destroy them as entities themselves. Appropriate support can be used for the growth of the cluster in a regular manner, keeping them anchored and far apart one from each other, preventing sintering that would destroy the peculiar properties of the nanoparticles [37, 38]. Such arrays or cluster superlattices would allow one to address single clusters to obtain a large amplitude of response resulting from the additive superposition of all single clusters, and characteristic for a cluster of well-defined size in a specific environment as needed in catalysis. Moreover, to obtain a collective coherent response characteristic of a large interacting ensemble of clusters as in optics. In the graphene case, due to the difference in lattice constant between graphene and Ir(111), the combined system shows a larger

periodicity and presents some modulations both in the geometry and in the electronic structure. These modulations are referred in the literature as moiré pattern. The moiré superstructure arises from the different registry between the carbon atoms of graphene and the underlying Ir substrate, which varies across the moiré unit cell. Different regions can be recognized, named *fcc*, *hcp*, and *atop*, according to the position of the carbon hexagon with respect to the Ir substrate. Therefore, the adsorption behavior of adsorbates should be different at different regions of the moiré pattern.

STM measurements show that the deposited Pt atoms at room temperature yield a self-assembled cluster lattice with hexagonal pattern of Pt particles adsorbed on the hcp region of the moiré unit cell [37, 39]. This well ordered arrangement is stable up to 400 K for small sizes and up to 650 K for large sized particles. The adsorbed Pt atoms are found where the hexagons of the carbon are centered on top of the Ir atoms in the second layer or the third layer of the hcp and the fcc regions respectively (a threefold coordinated hcp-site or a threefold coordinated fcc-site). In those two regions of the moiré the adsorption of the cluster yield local buckling in the graphene layer. The graphene layer locally re-hybridizes from sp^2 to sp^3 carbon bonds at specific regions of the graphene moiré and in between the substrate and the deposited metal [40]. This model has been experimentally verified by means of X-ray photoelectron spectroscopy (XPS); in particular, C1s core level shifts (CLS) for Gr/Ir(111) carbon atoms were acquired, both with and without adsorbed Pt clusters; the results were then compared with the CLS calculated in the framework of the re-hybridization model using DFT calculations [40].

Similar behavior was observed also in the case of Ir clusters, whereas no buckling of graphene was observed in the region where the carbon hexagons are centered on the Ir of the first layer (where no carbon atoms atop substrate sites) [41]. This suggests that, the local sp^3 re-hybridization of carbon atoms controls the adsorption metal clusters, leading to the formation of well ordered nanoclusters.

Pt cluster arrays grown on the Gr/Ir(111) template were tested for their stability with respect to CO gas exposure. In particular, Gerber et al. studied the cluster stability and adsorption-induced processes by means of in situ STM and XPS [42], finding a CO-induced Smoluchowski ripening effect on small Pt cluster (less than 10 atoms) superlattices. Sintering takes place when a certain CO threshold coverage is reached, with a substantial reduction of the number of clusters. It was demonstrated that the CO situated on the edge Pt atoms of small clusters largely affects the graphene rehybridization, enhancing the cluster mobility. The CO adsorption could also lead to transformation of the cluster to three-dimensional shape. Moreover in the same work, through spectra of 1 s orbital of the O and C atoms in CO measured after CO saturation, it was demonstrated that for Pt clusters smaller than 40 atoms, CO adsorbs on-top sites.

The Pt clusters grown on the graphene/Ir(111) system is already well known in literature and has been investigated by means of a number of techniques [37–40], [42–44]. Moreover, some structural properties as well as thermal and chemical stability properties are not novelty. What is lacking is a fundamental knowledge of the reactivity of graphene-supported Pt clusters beyond UHV con-

ditions. New experiments were performed by E. Vesselli and coworkers to study the morphology and reactivity of Pt clusters grown on the Gr/Ir(111) template. More attention was given to the CO adsorption at Pt clusters of different sizes, as a function of the gas pressure and sample temperature.

2.2 Experimental results

This investigation was done using Low temperature Scanning Tunneling Microscope (LT-STM), infrared-visible Sum Frequency Generation (SFG), and X-ray Photoelectron Spectroscopy (XPS) from ultrahigh vacuum (UHV) to near-ambient pressure.

2.2.1 Growth mode of Pt/GR/Ir(111)

Pt clusters was grown using Chemical Vapor Deposition (CVD) in UHV at room temperature. STM measurements were used to follow the growth behavior of Pt on GR/Ir(111). The amount of Pt loaded onto full monolayer (ML) of GR/Ir(111) was varied between 0.05 to 1.50 ML. The Pt coverages were expressed in ML with respect to the surface atomic density of Ir(111) surface. The moiré unit cell contains ~ 81 Pt atoms, then a Pt coverage equal to 1 ML means that 81 Pt atoms are present within the moiré unit cell.

Figure 2.1 shows the STM topographs (upper panel) and size-distribution histograms (lower panel) for different Pt coverages on graphene/Ir(111). Several parameters reported in table 2.1 were extracted from the STM images in Figure 2.1 to understand the growth behavior of Pt aggregates at different coverages. The average cluster size (in atoms) for different Pt coverages was obtained using the next formula:

$$s_{av} = \frac{\Theta \cdot A_m}{n} \tag{2.1}$$

where Θ is the deposited amount of Pt expressed in ML with respect to the underlying Ir(111), and A_m is the number of Ir atoms per moiré unit cell (81 atoms), and n is the fraction of moiré cells occupied by a cluster (the filling factor) which varies from 0 (empty moiré) to 1 (totally occupied moiré).

At Pt coverages less than 0.23 ML, the average cluster size was 7.2 atoms for 0.05 ML and 8.7 atoms for 0.09 ML. At these coverages the moiré filling factor (Figure 2.2, left panel) is about 80%, and high percentage of superlattice distribution mainly consists of single layer clusters (Figure 2.2, right panel).

At 0.25 ML, the graphene moiré is almost completely filled with Pt clusters at filling factor of 88%. The cluster size distribution is broad (Figure 2.9, lower panel), with the presence of both 14 and 30 atoms cluster. From the height distributions in Table 2.1, 2-layered clusters are dominant for this Pt coverage, associated to 30 atoms cluster. While the 1- layer clusters coexist with an average size of 14 atoms.

Upon deposition of 0.74 ML Pt, well-ordered hexagonal arrangement of the clusters was observed (Figure 2.1, upper panel). 95% of the graphene moiré was occupied, with an average cluster size of 60 atoms. Additionally, the moiré unit cells are mostly populated by 2-layer clusters.

Table 2.1: Structural parameters extracted from the STM images shown in Figure 2.1 for different Pt coverages: the filling factor (n), average cluster size s_{av} in atoms, and the different layers formation. Figure from [1]

			layer formation (%)			
Coverages (ML)	n	S_{av}(atoms)	1-layer	2-layer	>2-layer	h_{av}(ML)
0.05	0.56	7.2	78	19	3	1.25
0.09	0.79	8.7	76	23	1	1.25
0.23	0.88	21	36.5	57.5	6	1.69
0.74	0.95	63	3	76.5	20.5	2.23
1.50	1.00	140 to 300	3	74	23	2.20

At the highest investigated coverage (1.5 ML), coalescence between clusters growing in adjacent cells is dominant and evident from the images (Figure 2.1, upper panel), yielding large particles with on average 140 and up to 300 atoms (Figure 2.2, right panel). The clusters coalesce without leaving their moiré unit cells, due to their size and significant binding. Concerning the cluster height distributions, there are 74% of 2−layered clusters and 23% of (> 2)−layered clusters.

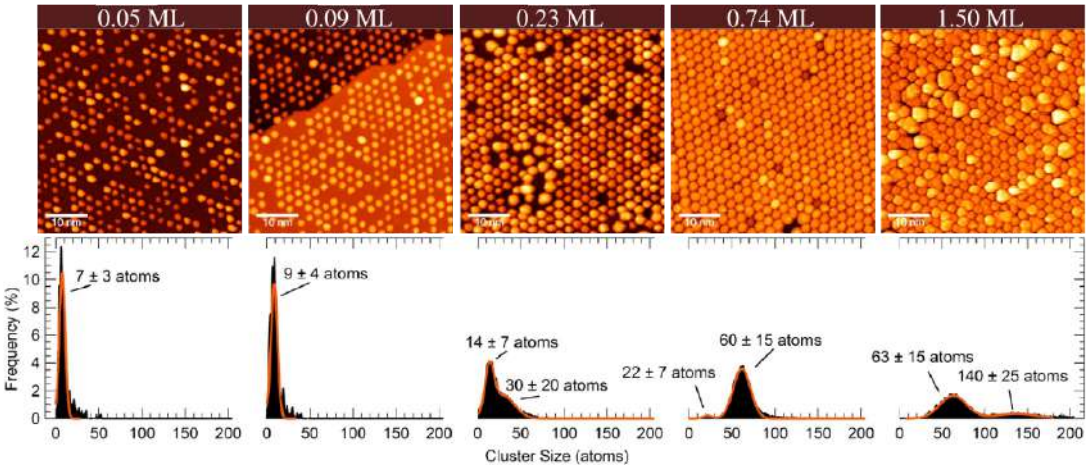

Figure 2.1: STM images of Pt clusters at room temperature on graphene/Ir(111). Pt loadings span from 0.05 to 1.5 ML (from left to right), depending on image). In the bottom panel, corresponding size distributions (cluster size frequencies) are shown as obtained upon averaging the whole STM image data set: continuous lines represent fitting curves with Gaussian profiles. The STM image size is 50×50, V bias = $+1.0$ V. Figure from [1].

2.2.2 CO adsorption on GR/Ir(111)

STM images of Pt nanoclusters exposed to CO molecules are shown in Figure 2.3. for three Pt loading. The Pt clusters were exposed to 1×10^{-7} mbar of CO at room temperature until a dose of 10 L was reached. The adsorption of CO molecules yield a significant decreasing of the filling factor to almost half of the initial value for the smallest clusters. This is due to the so called Smoluchowski ripening [42], in this case the particle mobility and coalescence occur, which

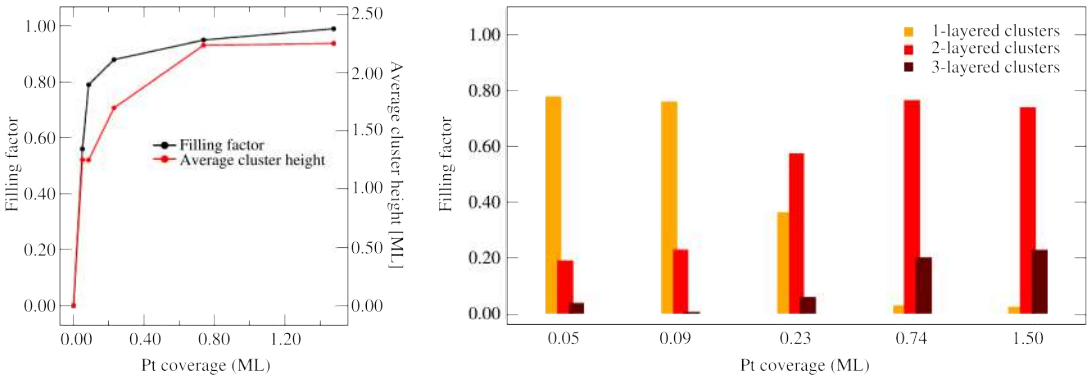

Figure 2.2: On the left: Black curve shows the fraction of occupied moiré (filling factor n) as a function of Pt coverage. Red curve shows the average cluster height (expressed in layers) as a functions of the Pt coverage. Two different scales are used for the y-axis. **On the right**: Cluster height population for each Pt coverage. Figure from [1].

leads to clusters merging into larger clusters. A regular structural pattern can

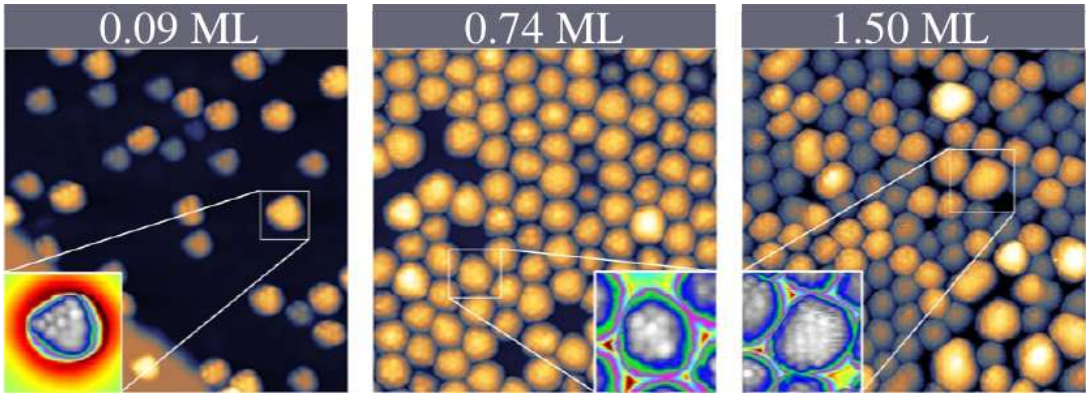

Figure 2.3: STM images of Pt clusters exposed 10^{-7} mbar at room temperature. Insets (zoomed) show selected clusters with enhanced color contrast to highlight the CO-induced corrugation. The STM image size is 25 × 25, V bias = +1.0 V. Figure from [1].

be observed on the surface of the clusters (Figure 2.3, insets), showing hexagonal symmetry with a lattice constant reducing progressively from 5.0 to 4.0 Å with growing cluster size (from 0.05 to 1.5 ML Pt, respectively).
IR-vis SFG measurements were performed for the detection of chemisorbed CO on ordered Pt clusters on GR/Ir(111) at room temperature. The C−O stretching resonance were employed under in situ reaction conditions, in the pressure range 10^{-8} to 1 mbar.

Figure 2.4 displays the SFG data of the C−O stretching region together with the best fit and the deconvolution of the resonance. Four non-equivalent stretching modes (P_i , i =1−4), corresponding to CO molecules adsorbed in non-equivalent sites, are observed, depending on the adsorption conditions. A double vibrational frequencies were observed for the lowest Pt coverage (0.05 ML) in 10^{-8} mbar CO: P_2 at $\omega_2 = 1975\ cm^{-1}$) (green) and P_3 at $\omega_3 = 2039\ cm^{-1}$ (violet) (Figure 2.4, a). The peak positions of CO at high pressure (1 mbar) was shifted to 2000 and 2071 cm^{-1} for P_2 and P_3 respectively. In addition, a third peak,

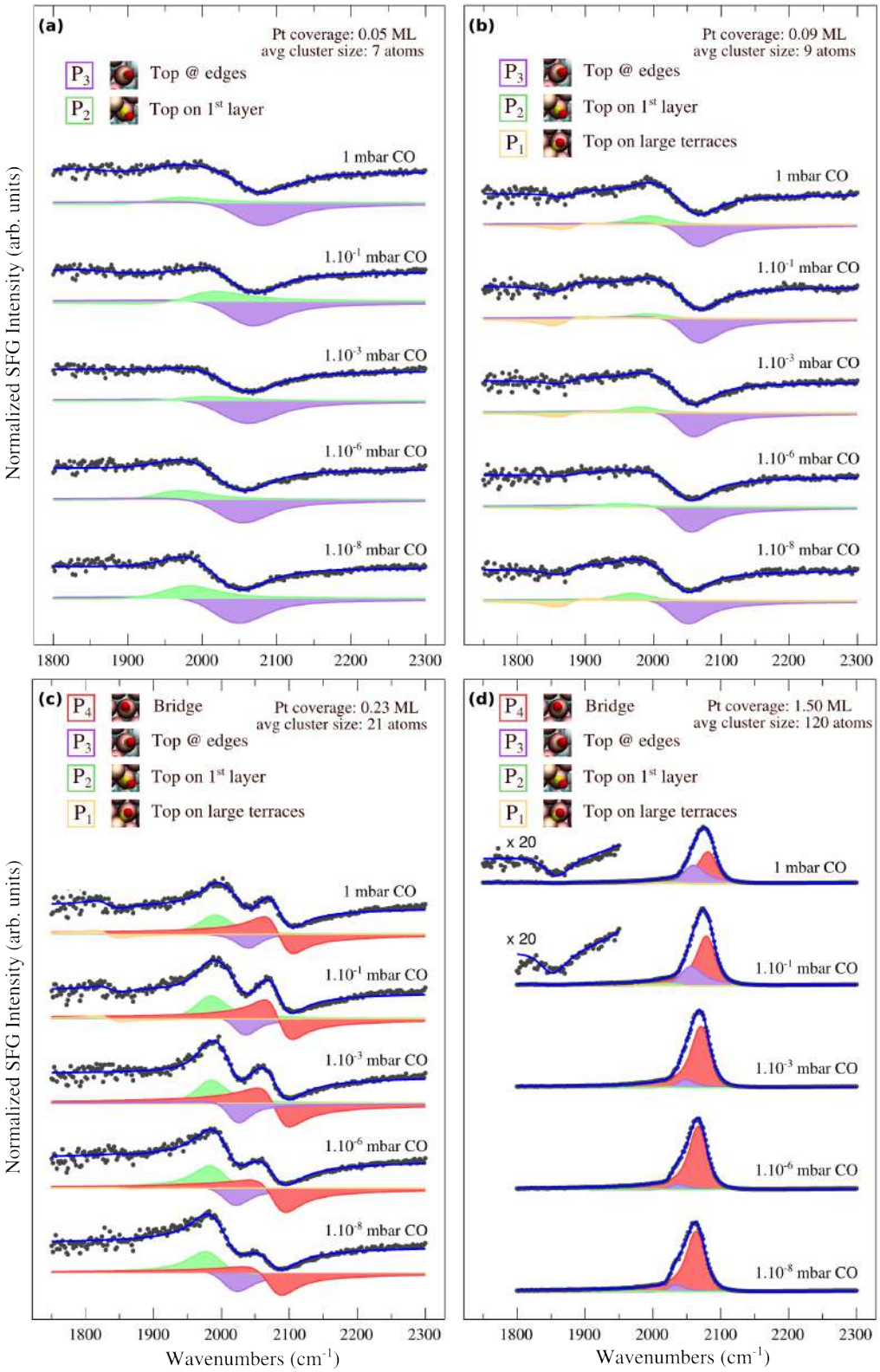

Figure 2.4: IR-Vis SFG vibrational spectra in the C−O stretching region collected at room temperature in situ for increasing Pt cluster size (from a to d) and upon exposure of the CO pressures (from bottom to top in each of the panels). Experimental data (grey dots) and best fit curve (blue line) are plotted together with the deconvolution of the spectral vibrational features. Figure from [1].

P_1 (yellow), with very low intensity and dispersive line shape is observed at $\omega_2 = 1845\ cm^{-1}$. A significant Gaussian broadening of the whole spectrum is also found ($\sigma = 25\ cm^{-1}$). This can be explained by a high structural and chemical inhomogeneity of the system induced by CO, in agreement with the STM measurements. A similar situation was observed also for 0.09 ML Pt, with $\omega_1 = 1871\ cm^{-1}$, $\omega_2 = 1969 - 1993\ cm^{-1}$, and $\omega_3 = 2041 - 2057\ cm^{-1}$ (Figure 2.4,b). The Gaussian broadening reduces to $\sigma = 15\ cm^{-1}$, indicating a less inhomogeneous system with respect to the 0.05 ML case. At 0.25 ML Pt (Figure 2.4,c), a fourth feature P_4 (red) appears in the $\omega_3 = 2076 - 2087\ cm^{-1}$ range, depending on the CO pressure, and the inhomogeneity contribution further decreases to $\sigma = 11\ cm^{-1}$. The intensity of the fourth resonance increases by almost one order of magnitude when further increasing the Pt cluster size up to 1.5 ML (Figure 2.4,d), while no additional features appear.

As a general trend, the line shape analysis of the IR-vis SFG signal reveals a relevant weakening of the observed Gaussian broadening, from 25 down to 7 cm^{-1} , for increasing Pt loading. This is in agreement with the STM images that show an increased degree of order of the superlattice for larger particles. In addition, higher CO pressures yield a typical, progressive blue-shift of the stretching features, consistent with a denser CO phase at the clusters' surface and with the CO-induced coalescence of adjacent particles.

The vibrational spectroscopy of CO adsorbed on Pt nanoclusters provided four non-equivalent CO species as shown in Figure 2.4. The position of the resonances can give an insight into the metal−adsorbate bond strength and thus about the corresponding adsorption site. The C−O stretching frequency of the adsorbed CO is red-shifted with respect to the gas-phase, this is due to the weakening of the C−O molecular bond. This phenomenon is understood on the basis of the bonding mechanism on metallic Pt, described by the Blyholder model [45, 46] sketched in Figure 2.5.

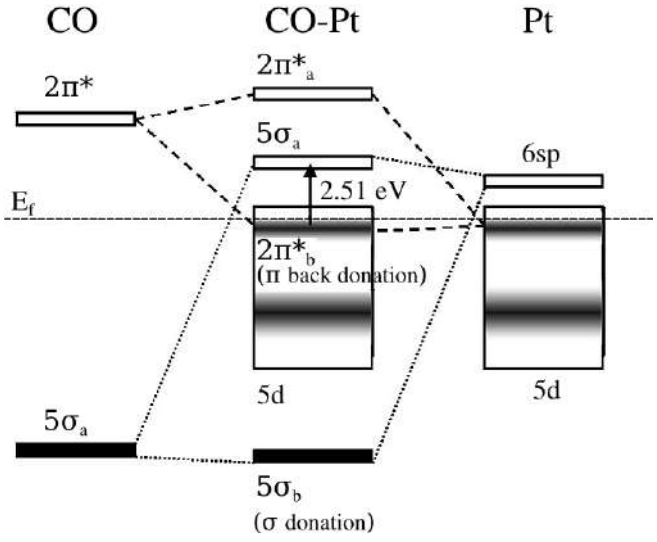

Figure 2.5: A schematic molecular orbital diagram for the interaction between CO and Pt. Black indicates occupied states and white indicates vacant states. Figure from [45].

The hybridized states between CO and Pt originate from the σ electron

donation from the filled 5σ orbital of CO to the vacant 6sp conduction band of Pt and by the π electron back donation from 5d of Pt to the vacant $2\pi^*$ orbital of CO. Since the latter interaction leads to the introduction of electron density into the CO antibonding orbital, there is a consequent reduction in the C−O bond strength, and hence the red-shift with respect to the resonance at 2170 cm^{-1} of free CO [45].

In the case of adsorption on Pt, a simple model can be obtained by considering the coordination number (CN). It suggests that lowering the Pt coordination number is important in determining the C−O bond strength. The lower the Pt coordination number, the stronger the Pt−CO interaction, thus the stronger the electron back-donation and the weaker the C−O bond. High energy spectral features P_4 was attributed to more coordinated species, namely CO molecules adsorbed at on-top sites Pt atoms in the middle of (111) terraces on multilayer clusters, where Pt atoms have the highest possible coordination number ($CN = 9$) [47–51]. The P_4 spectral feature grows for Pt loadings higher than 0.25 ML, when 2-layer clusters start growing. The P_3 feature was observed in the energy range $2015 - 2060$ cm^{-1}, this peak was associated to the C-O stretching mode of CO adsorbed at on-top sites of single-layer clusters ($CN = 6$) at 0.05 and 0.09 ML Pt coverage. For thicker clusters, this peak was attributed to CO adsorbed on top of edge Pt atoms at the borders of the first layer of the cluster ($CN = 6$). The P_2 component was found at lower energy range $1980 - 2010$ cm^{-1}, a negligible contribution to SFG spectra was observed from small clusters, while its intensity grows for higher Pt loadings. In this case the spectral feature are associated to CO molecules adsorbed at on-top sites of edge Pt atoms for 1-layered clusters or corner Pt atoms for multilayer clusters ($CN = 4$ or $CN = 3$) [52]. Lastly, P_1 is the lowest energy feature that was observed in the energy range $1840 - 1870$ cm^{-1}. This vibrational feature was observed for high CO pressures and with higher and with growing intensity for larger cluster sizes. This peak was attributed to CO adsorbed on the bridge sites of the Pt clusters. Under high CO coverage conditions (> 0.5 ML), CO adsorbs on (111) terraces forming a c(4×2) superstructure, so that bridge sites also get populated [48, 53, 54]. The intensity of the P_1 (yellow) peak appears weaker compared to the on-top ones, because of the smaller IR and Raman cross sections [54]. From the SFG spectra, blue-shift of the on-top vibrational features is observed for increasing CO pressure, due to the strong dipole-dipole interaction between the adjacent CO molecules.

2.2.3 Effects of temperature

Temperature investigations (from RT up to 570 K) were performed on Pt clusters at 0.1 mbar pressure of CO. Figure 2.6 shows the IR-vis SFG spectra for the C−O stretching region measured for 0.05 (left) and 0.23 ML (right) of Pt on graphene. When temperature increased to 348 K, the same components are present and no appreciable difference was observed with respect to the RT. At 423 K, all the peaks appear red-shifted with respect to their RT positions. Moreover, for high Pt coverage (0.23 ML), the vibrational frequency associated with the P_4 component appears more intense and sharper, as shown in Figure 2.6, right panel. Increasing the temperature, this peak shows a red shift of about

50 cm^{-1} down to the $2040 - 2057$ cm^{-1} range, this intense peak is referred to as P_5. The high intensity of this peak was ascribed to the change in electronic structure of the adsorption site, compatible with the spillover of the CO from Pt cluster to Ir surface. Temperature dependent red-shift results from the anharmonic coupling with the frustrated translation modes of adsorbed CO molecules [55]. Similar behavior was already observed for CO/Ir(111), where the C−O stretching mode is found in the $2063 - 2079$ cm^{-1} range [56], close to the values reported here. The intensity of this peak may also be associated to the progressive growth of density packed CO island at the Ir(111) surface, as observed in the case of CO intercalation at the GR/Ir(111) interface [57]. A broad and less intense component (P_6, cyan) at 1880 cm^{-1} was also observed in the case of larger clusters, due to a thermal induced loss of registry and inhomogeneity of CO in the bridge sites of the cluster. The interpretation of this vibrational

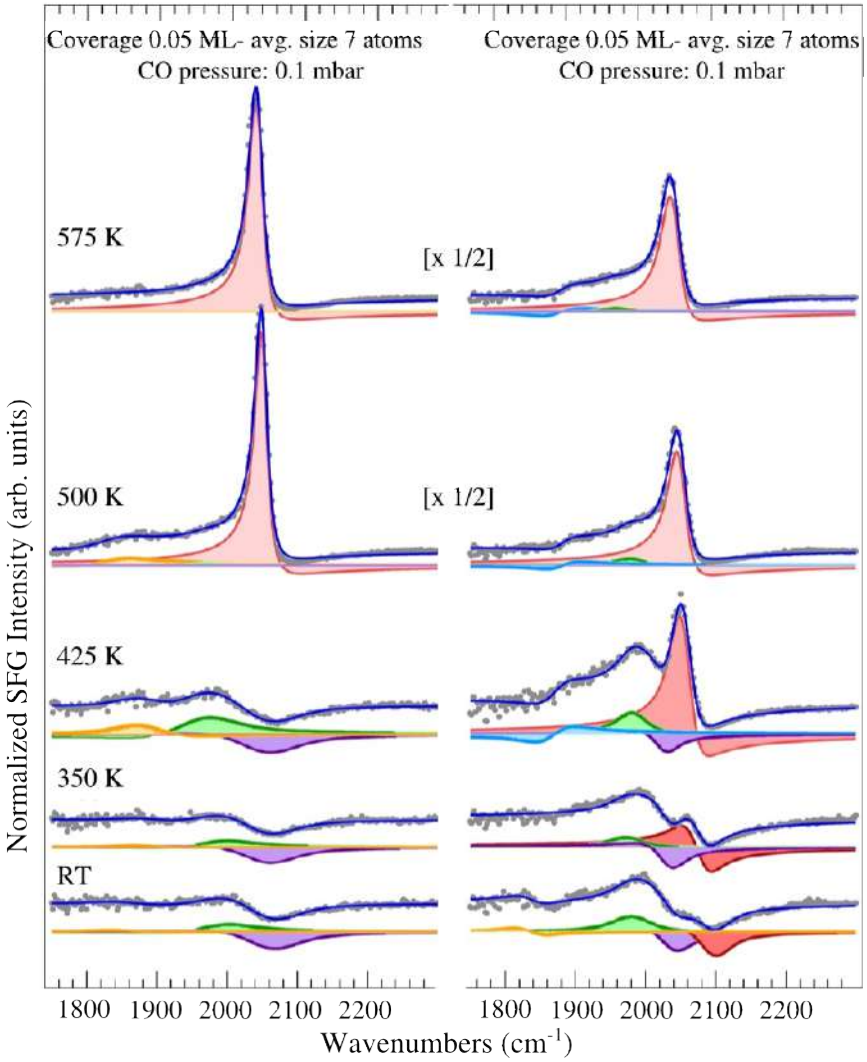

Figure 2.6: IR-Vis SFG vibrational spectra in the C−O stretching region collected in situ at 0.1 mbar CO as a function of the sample temperature for 0.05 ML (left) and 0.25 ML Pt (right). Experimental data (grey dots) and best fit curve (blue line) are plotted together with the deconvolution of the spectral vibrational features. Figure from [1].

peak was also investigated by Near-ambient pressure XPS experiments. What

has been found is that the presence of Pt clusters catalyses the graphene foil degradation already at 423 K (for 0.1 mbar of CO pressure), allowing the CO molecules to intercalate and adsorb on the underlying Ir (111) surface. The P_5 feature can be attributed to CO adsorbed on-top on Ir(111), in agreement with previous SFG measurements [56].

2.3 Theoretical investigation

In the following sections, we investigate the adsorption behavior, electronic structure, and the structural details of Pt nanoclusters on Graphene/Ir(111). Furthermore, we also report the interaction of Carbon mono-oxide (CO) with different Pt clusters sizes (Pt_4, Pt_7, Pt_{19}, and Pt_{31}).

2.3.1 Calculation details and structural model

Spin-polarized DFT calculations without Hubbard-U corrections were performed. Semiempirical corrections accounting for the van der Waals interactions, that have been proved important to properly describe the binding of epitaxial graphene with transition metals, are included with the DFT-D approach [58]. After convergence tests, we set a kinetic energy cutoff of 30 Ry for wave functions and of 300 Ry for the charge density basis sets, and we used the Methfessel-Paxton smearing technique, with an energy broadening of 0.02 Ry [59].

Graphene/Ir(111)

The calculated equilibrium lattice parameters are 2.46 Å and 2.75 Å for graphene and for the Ir(111) surface respectively, in excellent agreement with previous works [60] and with the experimental values of 2.46 Å and 2.715 Å, respectively (the latter derived from the bulk value) [61]. The ratio between the graphene and the iridium lattice constant is equal to 0.91, with the iridium lattice about 10% larger than the graphene one.

The Moiré structure of GR/Ir(111) is modeled using a supercell with 10×10 GR unit cells on 9×9 Ir surface (111) unit cells, with the in-plane lattice parameter fixed at the Ir value. The graphene layer is therefore stretched by only 0.6% with respect to its equilibrium lattice constant. To reduce the computational effort, the Ir substrate is modeled with a 2-layer slab geometry, for a total of 362 atoms included in the simulations. The repeated slabs are separated by about 26 Å, a space large enough to accommodate also the presence of clusters without introducing fictitious interactions with repeated images. Γ-point sampling is used for Brillouin zone integration, the convergence was done for small cells, for example: Γ-point for 10×10 graphene cell correspond to $12 \times 12 \times 1$ mesh for 1×1 graphene unit cell. The interplanar distance between the top-most and second Ir layers is kept fixed at 2.15 Å, derived from a full optimization of a 1×1 Ir(111) slab. The position of the graphene layer is also optimized: in the absence of Pt, the result is an almost flat layer, with an average distance from the substrate of 3.13 Å and a corrugation of about 0.30 Å.

The registry of the graphene layer with the iridium substrate locally changes at different regions of the supercell. It can be characterized by the relative

position of the center of the hexagons of graphene with respect to the Ir atoms of the substrate, as already proposed in several previous works. In this way, fcc, hcp, and atop regions can be identified, which correspond to hcp-top, fcc-top, and fcc-hcp positions of the carbon atoms [61], respectively (shown in red in Figure 2.7, left). Fcc and hcp regions are the closest to the substrate, with a distance of 3.00 Å, whereas the atop region is the most distant 3.25 Å. Since Pt deposition affects the graphene structure, with pinning effects depending on the Pt loading, the graphene geometry is optimized in each run.

Since the simulation of graphene on Ir(111) is very demanding, we describe the three different high symmetry regions with other reduced models (see Figure 2.7, right). In this case, we have used fictitious systems with cell reduces with respect to the full model (10×10 graphene/9×9 Ir(111)), where the graphene stretched with the underlying substrate and has the same registry for each region. In this view, we performed calculations in a supercell with 5×5 GR unit cells stretched to match 5×5 Ir(111) surface cells (see Figure 2.7, right panel); three different models have been used, considering different registries between graphene and the substrate in order to mimic the nonequivalent fcc, hcp, and atop regions. For the reduced models, three atomic-layers of Ir has been always used. We checked that the results do not change significantly if only two atomic-layers are considered, therefore validating that choice for the full model. The Brillouin zone is sampled using a $2 \times 2 \times 1$ Monkhorst-Pack grid [27], centered at the Γ-point. For symmetry reasons, in the reduced models, the epitaxial graphene without adsorbed nanoclusters is perfectly flat, with a distance from the substrate (3.18 Å) which is very close to the one obtained in the more realistic, larger model. Even though the size constrains introduced in the reduced models limit the possibility of deformation of graphene upon nanocluster adsorption, some tests with the larger model confirm the trends obtained.

2.3.2 Pt clusters of different sizes on graphene

According to the experimental observations [1], Pt clusters (up to 20 atoms) on graphene moiré prefer one-layer formation of the clusters. The Pt-Pt bonds become stronger for higher cluster sizes. Moreover, increasing the Pt coverage the Pt atoms aggregate forming well ordered hexagonal structure. This implies that the Pt nanocluster selectively adsorb in only one region of the graphene moiré. To interpret the growth mechanism of these clusters, we therefore studied different sizes of Pt nanoclusters starting from small atomic aggregates up to a 31 atoms cluster. We quantify the stability by calculating the adsorption energy of the Pt cluster on the GR/Ir(111) substrate as follows:

$$E_{ads} = E_{Pt_n+substrate} - E_{Pt_n} - E_{substrate}, \tag{2.2}$$

where $E_{Pt_n+substrate}$ is the total energy of n Pt atoms cluster on GR/Ir(111) substrate, E_{Pt_n} is the total energy of the isolated Pt cluster, and $E_{substrate}$ is the total energy of the GR/Ir(111) substrate. A large absolute values of the adsorption energy with negative sign means strong binding of the Pt atoms on the supported graphene.

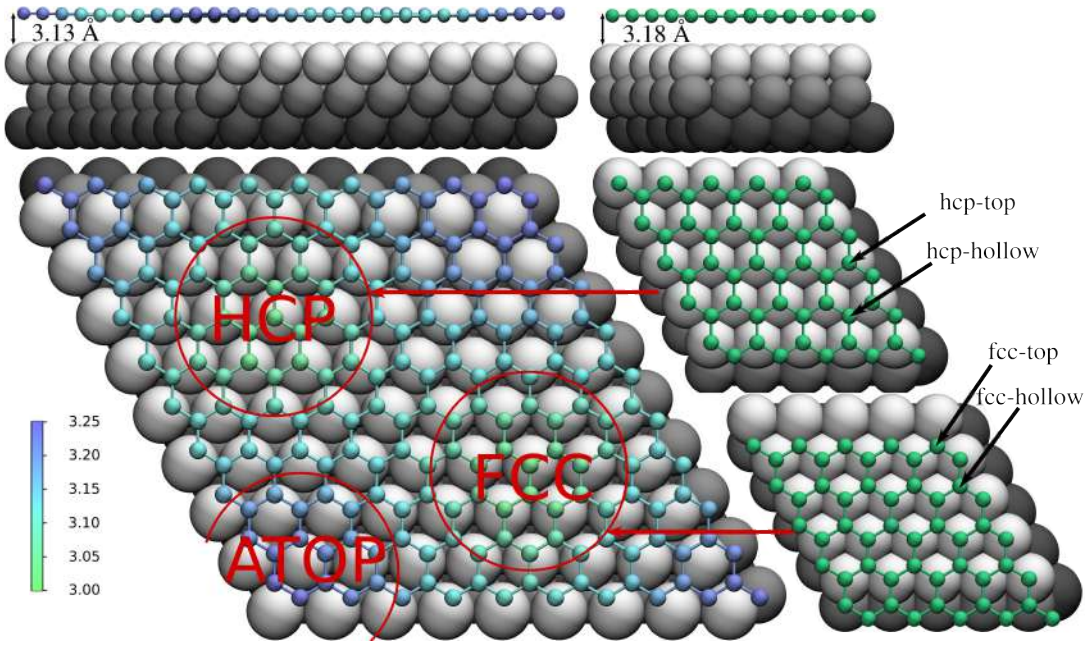

Figure 2.7: Left side: Top and side view of optimized structure for the full model of the graphene Moiré on Ir(111) described by a GR(10×10)/Ir(9×9) supercell. **Right side**: Top and side view of the reduced models for the hcp and fcc regions, described by two different GR(5×5)/Ir(5×5) supercells. The color scale of the C atoms on the left bottom maps the distance with respect to the Ir-substrate: the average graphene distance from the Ir substrate is 3.13 Å in the full model and 3.18 Å (constant value) in the reduced models. The possible adsorption sites for hcp and fcc regions are labeled in black arrow. Figure adapted from [1].

We started by investigating the most stable adsorption sites for single Pt atom at different sites of the moiré regions [62]. Thoes sites are shown in black arrows in Figure 2.7, right. The adsorption energies for the Pt adatoms on the hcp and the fcc regions of the moiré pattern for the full and reduced model are summarized in Figure 2.8. In both hcp and fcc regions of the moiré, the adsorption of Pt atom on the C in the hollow sites was found to be more energetically stable. For the hcp region, the carbon atom is located on top of the Ir atom in the second layer, while in the former region, the C atom is located on top of the Ir atom in the third layer. The overall results obtained using the reduced models are not significantly different from the full model, therefore validating the model to study small aggregates of Pt atoms. In the following, each Pt atom is adsorbed on the hcp-hollow and fcc-hollow of the hcp and fcc regions, respectively.

Hcp vs fcc region

To demonstrate why Pt atoms are observed only in one regions of the moiré, we studied the adsorption of small cluster sizes (up to 9 atoms). Figure 2.9 shows relaxed DFT models for the aggregation of Pt nanocluster (increasing of the Pt atoms from up to down) at the fcc and hcp regions.

The interaction per Pt atom with the support decreases with the increase of the size of the cluster as shown in Table **??**. Moreover, in both the hcp and fcc

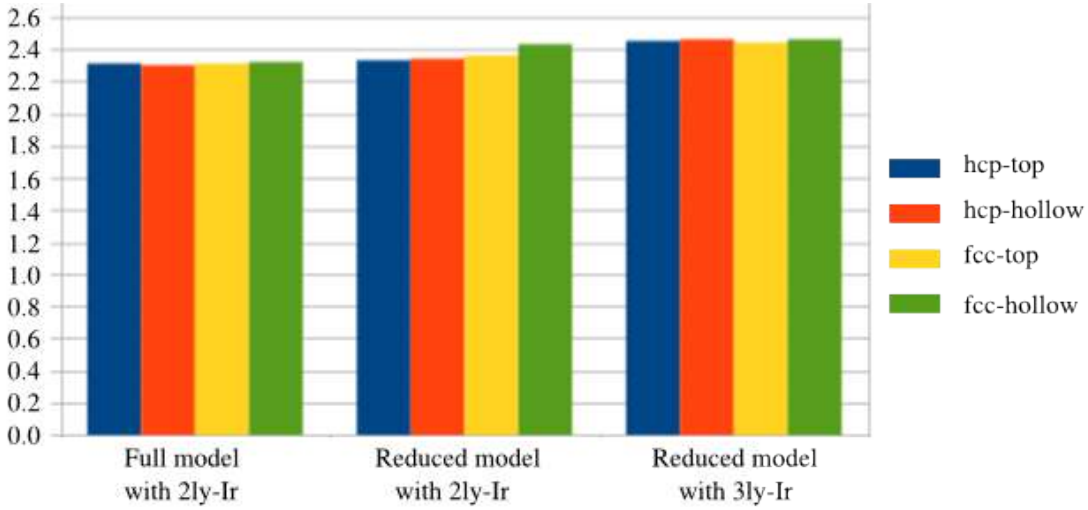

Figure 2.8: Shows the calculated adsorption energy for Pt adatoms on different sites of the hcp and fcc regions using a full and reduced models(thoes sites are shown in Figure 2.7). Blue and yellow are related to the adsorption on top of the sites in the metallic substrate, hcp and fcc regions respectively; red is for fcc site in the metallic substrate and hcp region, while the green is for hcp site in the metal and fcc region.

regions, the adsorption energy of the clusters increase with an increasing number of Pt atoms, which implies that the Pt atom like to bond to each other on those regions of the moiré. The single Pt atom has the same adsorption energy in the fcc and hcp regions. In the case of dimer, the fcc region becomes less stable by about 0.03 eV. For number of atoms $\geqslant 7$, aggregates on the hcp regions show clear energy difference (of about 0.20 eV) with respect to the FCC regions. These findings imply that the Pt atoms prefer to adsorb at the hcp region of the GR/Ir(111). This explains the well dispersed hexagonal arrangement of the Pt clusters at higher coverages, as observed in the experiments [1]. Moreover, high mobility of very small Pt aggregates are consistent with the absence of nanoclusters with number of atoms < 5 in the experimental observation.

Table 2.2: Shows the adsorption energy per atom for various cluster sizes adsorbed in the fcc (E_{ads}^{fcc}(eV)) and hcp (E_{ads}^{hcp}(eV)) regions of the moiré (as shown Figure 2.9).

clusters	E_{ads}^{fcc}(eV)	E_{ads}^{hcp}(eV)	$E_{ads}^{hcp} - E_{ads}^{fcc}$(eV)
Pt_1	2.31	2.31	0.00
Pt_2	1.57	1.58	0.02
Pt_3	1.39	1.38	-0.01
Pt_4	1.27	1.29	0.02
Pt_7	1.23	1.25	0.02
Pt_9	1.14	1.16	0.02

The Pt adsorption ($>$ 2 Pt atoms) in the both fcc and hcp regions of the moiré affects the graphene layer, as observed in Figure 2.9. Some carbon atoms

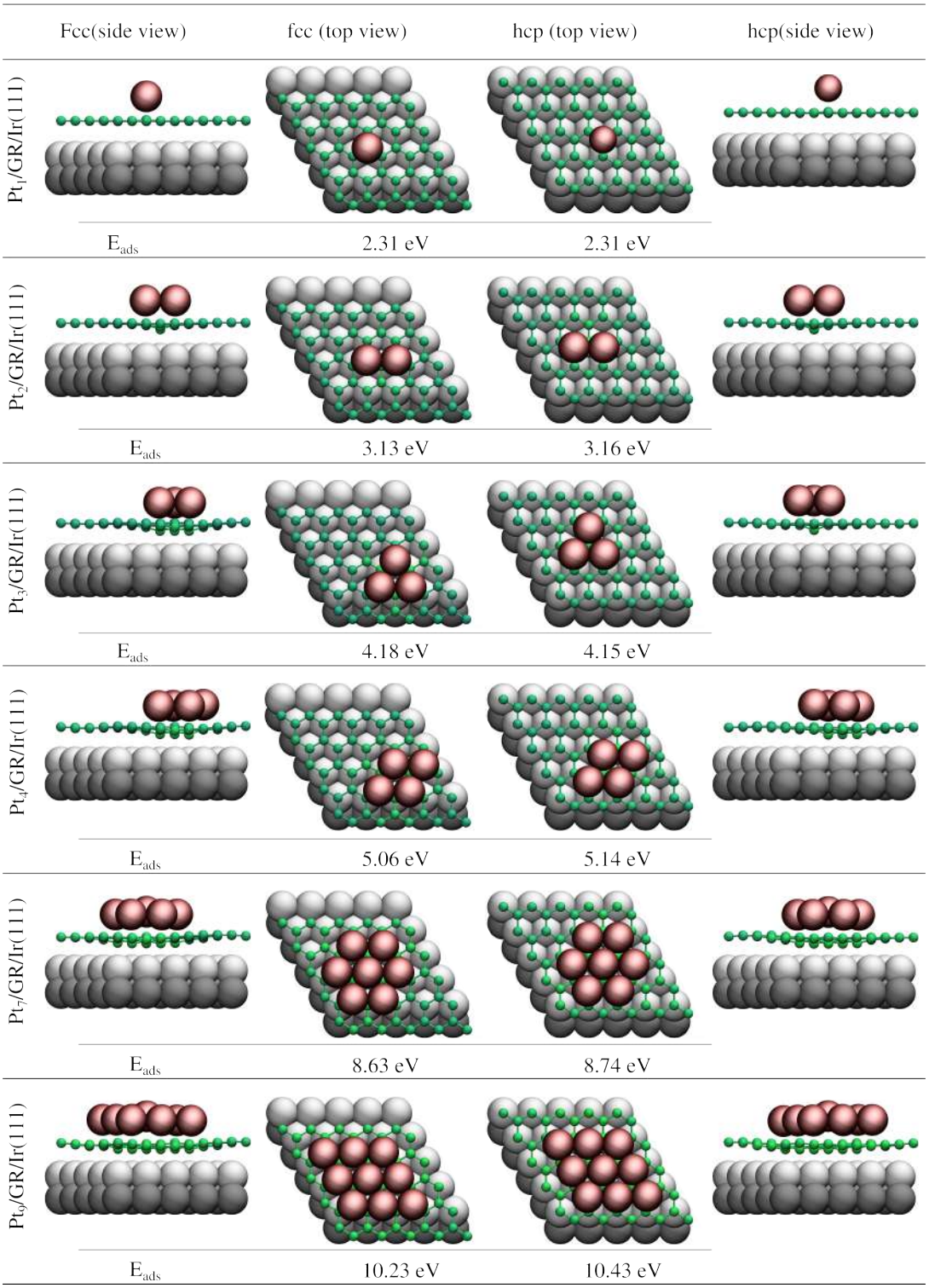

Figure 2.9: Optimized structure for the reduced model of the GR(5×5)/Ir(5×5) hcp unit cell with an adsorbed clusters (from up to down: 1, 2, 4, 7, 9 atoms), adsorption energies are reported at the bottom of each structure (in E_{ads}). A three-layer Ir(111) slabs were used

under the clusters are pinned toward the Ir(111) substrate. The pinned C atoms are those located on top of the Ir atoms in the first layer, where each Ir is located in the middle of three Pt atoms or in the bridge (as labeled in blue and orange

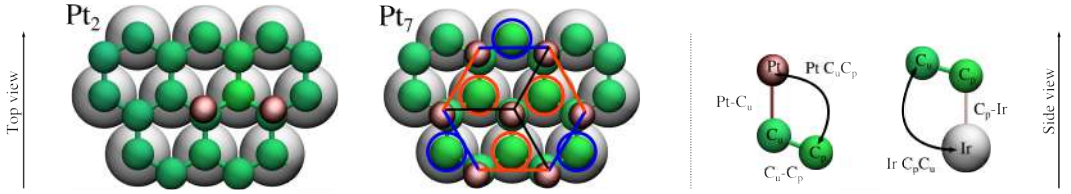

Structure	region	Pt-Pt Å	Pt-C_u Å	C_p-Ir Å	Pt C_uC_p	Ir C_pC_u	C_u-C_pÅ	d_{GR} Å
Pt_2	fcc	2.56	2.07	2.56	106.2°	107.2°	1.47	3.04
	hcp	2.56	2.07	2.52	106.6°	106.7°	1.48	3.03
Pt_7	fcc	2.68 2.64 2.69	2.52 2.10	2.35 2.39	98.8° 104.6° 111.4	98.3° 104.5° 106.8°	1.46 1.47 1.48	2.81
	hcp	2.68 2.64 2.69	2.54 2.10	2.34 2.38	98.4° 104.7° 111.4°	97.9° 104.6° 106.7°	1.45 1.47 1.48	3.80

Figure 2.10: Top panel: optimized structures of Pt_2 and Pt_7 on GR/Ir(111). In the case of Pt_7: Pinned carbons (C_p) with with 2 Pt neighbors are labeled in blue circle and the ones with 3 Pt neighbors are labeled in orange circle; bond lengths between edge Pt atoms are colored according to the C_p in the bridge between them; bonds with central C atom are labeled in black, Bond lengths and bond angles between graphene-adsorbed Pt atoms (PtC_uC_p) and graphene-underlying substrate (PtC_pC_u) are drawn on the right side . Bottom panel: sp^3 re-hybridization of graphene induces by $Pt_2$and Pt_7 at the hcp and fcc regions of the moiré. Referring to the labeles in the top panel, table shows; bond lengths: between Pt atoms (Pt-Pt), Pt atoms with underlying carbon (Pt-C_u), C bonds to Ir substrate (C_p-Ir); bond angles; and average distance of the graphene layer (d_{GR}).

in Figure 2.9, top panel). The number of C atoms squeezed at the $Pt - Ir$ interface increases with the number of Pt adatoms. The average distance of the graphene layer from Ir(111) substrate was decreasing from 3.03 Å for the dimer to 2.69 Å for the 9 atoms cluster.

Furthermore, we also found that the strong pinning of the graphene yield strong interaction between Pt atoms and GR/Ir(111). This was observed for both hcp and fcc regions of the moiré. Moreover, the pinning in the hcp region is slightly higher, which makes it more favorable for the adsorption of the Pt clusters. To clarify, as an example we refer to Pt_3 in Figure 2.9. We can see that the adsorption in the fcc region has a larger effect on graphene, because of the different adsorption configuration for Pt atoms in the two regions. In the fcc region, the Pt atoms are adsorbed such that three C atoms have two Pt atoms as the nearest neighbor are pinned toward the substrate. Whereas, in the hcp region only one C with three Pt nearest neighbor is pinned down. Thus, the arrangement of the Pt atoms within the hcp(fcc) regions is the one of the factors that detect the stability of the clusters.

Figure 2.10 explain how the Pt adatoms bind strongly to the graphene moiré. The strength of the metal−C bond can be form upon the sp^3 rehybridization of the C atoms[63]. Characterization of the bond lengths and bond angles for Pt_2

and Pt_7 in Figure 2.10 provide evidence about the local bonding in C atoms. C_p referred to the pinned carbon atoms on the graphene, and C_u referred to the carbons under Pt atoms. The calculated $C_p - Ir$ (the pinned carbon located on top of Ir atoms, labled in blue and orange circle for Pt_7) distance decreases from 3.17 Å in the absence of Pt atoms to 2.56 Å(2.52 Å) for the Pt dimer in the fcc(hcp) regions. The calculated Pt-C_u indicates the nature of the cluster bonding to the graphene, while the C_p-Ir bond shows the chemisorption of graphene under and in the vicinity of the adsorbed cluster to the Ir substrate. In Pt_2, the pinning of the C atoms produces a weakening of the sp^2-like in-plane bond that elongates from 1.42 Å to 1.47 Å(1.48 Å) for the fcc(hcp) regions respectively. The carbon atoms with 2(3) Pt neighbors (labeled in blue(orange) in Figure 2.9) are involved in a sp^3-like rather than sp^2 hybridization. Calculated bond angles (PtC_uC_p and IrC_pC_u) provide clear evidence that the local bonding is sp^3. All the calculated angles are close to the tetrahedral bond angle (109.5°) of sp^3 hybridization. For Pt_7, the Pt atom in the middle of the cluster is lifted up. The C under the Pt atom was pinned toward the substrate, increasing the Pt−C distance to 2.54 Å, see Figure 2.9.

1- and 2- layer configurations

From the previous section, we demonstrate that the occurrence of deformation of the cluster increases as the size of the cluster increases. In the case of Pt_7 and Pt_9, the Pt atom in the center of the cluster was lifted out (about 0.37 Å) with respect to the edge atoms. This behavior was stronger in the configurations with 19-atoms cluster, as shown in Figure 2.11. In this case, the Pt atoms were absorbed in 2D hexagonal arrangement on the hcp-hollow of the hcp region of the GR moiré. Upon optimization, strong deformation of the cluster was observed, leading to almost a dome shape. The Pt atoms at the edge of the cluster are strongly bound to the graphene layer, with the Pt−C_u distance ranging between 2.13 to 2.25 Å, while the central atom is at 2.15 Å distance. Three Pt atoms among those surrounding the central one are lifted up to an average distance of about 0.7 Å above the edge atoms, at distance of 3.43 Å, 3.30 Å, and 3.15 Å from the carbon under (C_u). Those atoms are labeled in black, blue, and aqua cross in Figure 2.11. However, not all the C atoms under the clusters are at the same hight, some of them are slightly pulled toward the Pt atom, increasing the $C - C$ bond length up to 1.58 Å and decreasing the Pt−C_u bond to 2.02 Å. At higher cluster size, the Pt−C_u bonds become weaker than the Pt−Pt bonds, and the Pt atoms tend to form a second layer.

The investigation of multilayer formation was done focusing on cluster sizes of Pt_{13} and Pt_{31}. It was shown that the interaction between Pt clusters and supported graphene also depends on the cluster facet which in contact with the support [64]. The (111) facets were showing stronger interaction than the (100) facets[65]. For a cluster of 13 atoms (see Figure 2.12), we adsorbed the cluster with three Pt-atoms parrall to the surface. A simple structural optimization procedure results in a flattening of the cluster, confirming therefore the tendency of small Pt particles to wet graphene.

As a selected example of larger clusters: Pt_{31} has been simulated in a 2-layer arrangement (as shown in Figure 2.13), consisting of a first layer of 19 (colored in

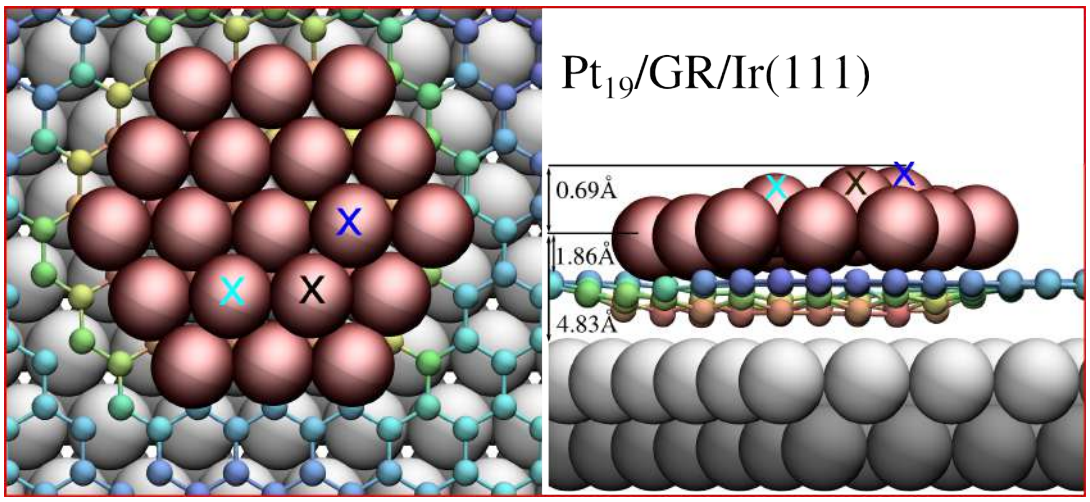

Figure 2.11: Fully optimized structure of the 19 atoms Pt cluster on the HCP region of the moiré. The 19 Pt atoms are in red color, three lifted atoms surrounding the central atom are labeled in black, blue, and aqua cross color. Average hight of the cluster from the graphene and the Ir substrate, together with the three lifted Pt atoms are also shown in the Figure. The graphene layer is colored according to the position of C atoms along the z-axis.

Structure	before the optimization	after the optimization
Pt_{13}/GR/Ir(111)	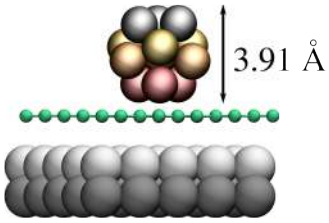	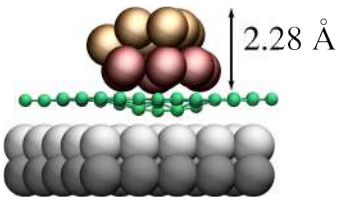

Figure 2.12: In the middle the initial configuration of a spherical Pt_{13} nanocluster on GR/Ir(111), and on the right its optimized structure after relaxation, suggesting the trend of nanoclusters with few Pt atoms to wet the GR layer. The average hight of the cluster is also shown in the figure.

red) and a second layer of 12 atoms (colored in orange), as previously described by Franz et all [43]. At variance with ref [43], we performed a full optimization has been performed, which, interestingly, gives a relaxed structure that well compares with the model used to fit surface X-ray diffraction data [43], with a strong pinning of the graphene toward the substrate.

2.3.3 CO adsorption on Pt nanoclusters

CO adsorption on Pt clusters have been investigated in order to study the effect of coverage and surface structure on CO adsorption. We first studied the adsorption of single CO molecules on various adsorption sites of Pt_4 cluster; on top of the Pt atom (T), in bridge between two Pt atoms (B), in the three-fold fcc-hollow (F-H), and on top of pinned carbon connected to 3 Pt atoms (P), as shown in Figure 2.14.

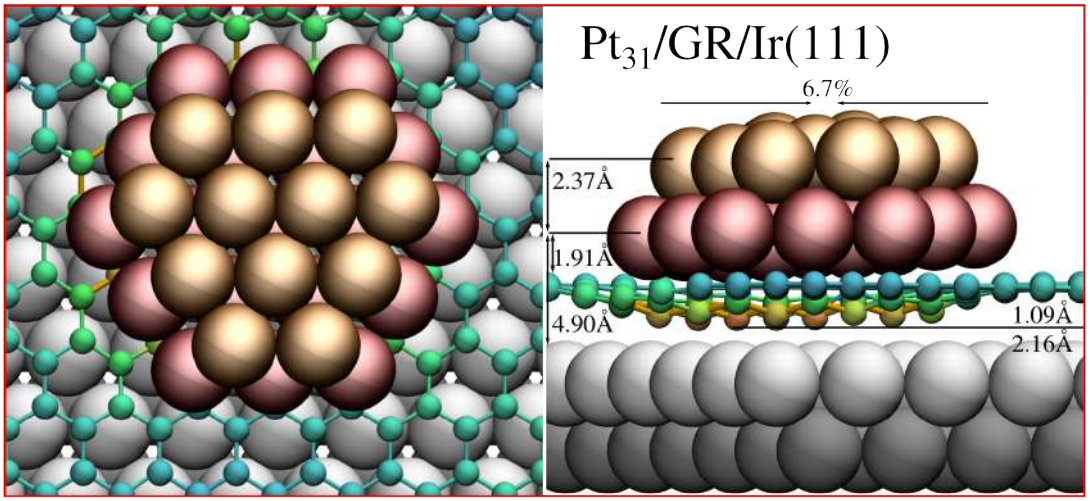

Figure 2.13: Fully optimized structure of the 31 atoms Pt cluster on the hcp region of the moiré. The 19 Pt atoms in the first layer (red) host the 12 atoms in the second layer (orange). Average distance between: first and second layer of the cluster, the first layer cluster from graphene, first layer cluster from the Ir substrate, the most pinned carbon from the atop region and from the Ir substrate. The graphene layer is colored according to the position of C atoms along the z-axis. Figure adapted from [1].

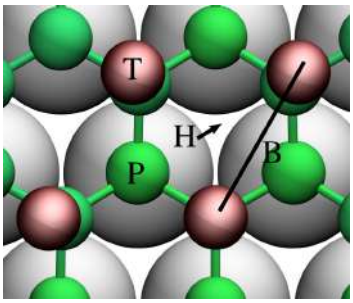

Sites	E_{ads} (eV)	C−O (Å)	Pt−C (Å)
P	1.47	1.20	1.32
F-H	1.63	1.21	1.31
T	2.00	1.16	1.88

Figure 2.14: Left Panel: structural model shows possible adsorption sites of Pt_4 cluster supported on hcp region GR/Ir(111): on-top (T), bridge (B), hcp-hollow (H), and top of pinned carbon (P). **Right Panel**: table shows adsorption energies (E_{ads}), bond length of CO molecule (C−O), and C (of the CO) distance from the Pt atom (Pt−C) for single CO adsorption on different sites of Pt_4.

Our calculated results show that a single CO molecule prefers top (T) adsorption site with $E_{ads} = 2\ eV$ and a different in adsorption energy of 0.53 and 0.37 eV, compared to P and H sites, respectively. For the adsorption of CO molecules on bridge site (B), the CO molecule migrate to the three-fold sites after geometry optimization. As a result of the different adsorption strengths, the Pt−C distance is larger for CO adsorbed on top site rather than on the other two sites. Moreover, the CO molecule at the top site is slightly tilted on the cluster surface with the C−O bond length of 1.16 Å and the average Pt−C bond length of 1.88 Å. These values are in agreement with experiments [66], and calculated results [67] for CO adsorption on Pt(111) at low coverage. The C−O bond at the other two adsorption sites (P and H) is a bit longer (about 1.20 Å) and the average Pt−C distance is shorter by 0.60 Å with respect to the top site. The adsorption of a single CO molecule on free-standing Pt nanoclusters has been

investigated by DFT also in previous works that report E_{ads} values from 2.09 to 2.84 eV, depending on the cluster size, shape, specific adsorption site, and exchange-correlation functionals [68, 69], therefore compatible, although bigger, with our results.

CO adsorption on various Pt cluster sizes

We investigated the effect of CO adsorption at nanoclusters of different size. The CO molecules are placed in a vertical position with the C-atoms pointing downward directly above the Pt atoms. During the optimizations, only the Ir(111) substrate was kept fixed. The adsorption energy of the CO molecule on Pt cluster was expressed as follows:

$$E_{ads} = [E_{nCO+substrate} - nE_{CO} - E_{substrate}]/n, \tag{2.3}$$

where $E_{nCO+substrate}$ is the total energy of n CO molecules adsorbed on the Pt/GR/Ir(111) system, E_{CO} is the total energy of the isolated CO molecule, and $E_{substrate}$ is the total energy of the Pt/GR/Ir(111) substrate.'n' refers to the number of adsorbed CO molecules.
The Pt clusters are adsorbed in the hcp region of GR/Ir(111) moiré.

- **CO adsorption on Pt_4**:

Figure 2.15 shows the optimized structures and adsorption energies of Pt_4 cluster for increasing CO coverage (top to bottom) from 0.25 to 1 ML. The adsorption energies change from 2.00 to 2.13 eV at most, since the CO molecules have enough space to tilt and reduce their mutual repulsion. The axes of the CO molecules are not perpendicular to the surface, and for growing coverage, the CO−CO dipole repulsion increases the deviation from the normal.

For CO adsorption on the Pt(111) single crystal surface (The system was modeled in 4×4 square cell with 4 layers of Pt), we obtain E_{ads} values ranging from 2.06 (zero coverage limit) down to 1.8 and 1.39 eV, in case of 0.5 and 1.0 ML (full coverage), respectively. Therefore, the presence of the GR/Ir(111) support seems to improve the affinity of Pt with respect to CO, yielding an overbinding effect. The calculated C−O bond lengths and the Pt−C distances are close to the CO adsorption on top (T) site of Pt cluster, and in good agreement with [66, 67].

Increasing the CO coverages on Pt_4, the Pt−Pt bond distances increase from 2.66 Å (for 0.25 ML, Figure 2.15, top) to 2.82 Å (for 1 ML, Figure 2.15, bottom) with respect to the 2.63 Å for the pure Pt_4 cluster. Our calculations for the supported Pt_4 nanocluster show that its structure is almost unaffected by CO adsorption at small CO coverage. The calculated C−O bond length is 1.16 Å (compared to the simulated value of 1.40 Å and experimental value of 1.41 Å [70] in the gas phase) and a Pt−C bond length of 1.88 Å. The Pt−C_u distance increases by 0.1 Å with respect to the pure cluster.

- **CO adsorption on Pt_7**:

The CO adsorption on Pt_7 at full coverage has similar behavior than on Pt_4: all the CO molecules on the edge are adsorbed, tilted with the same C−O and

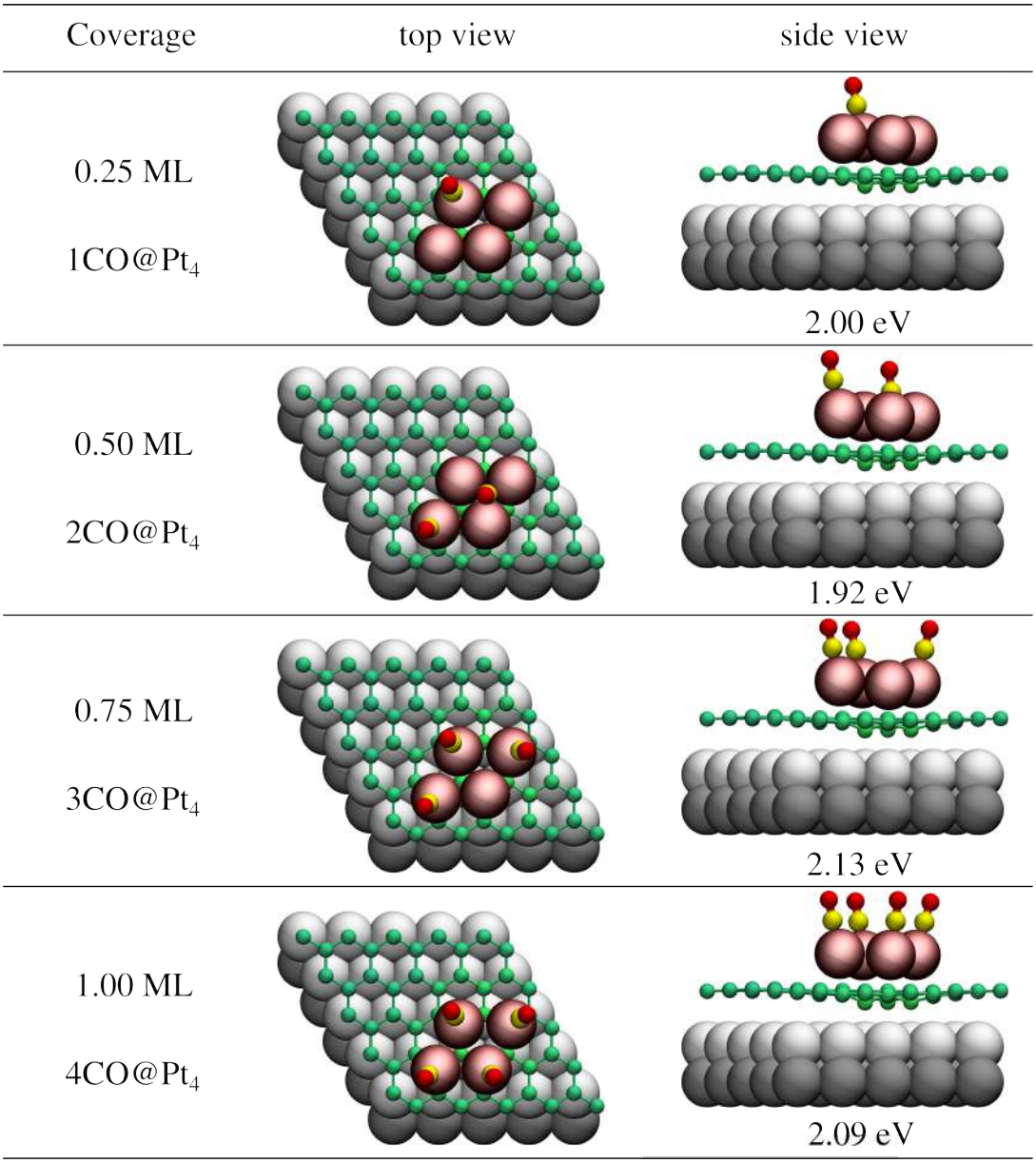

Figure 2.15: Optimized structure for the reduced model of the GR(5×5)/Ir(5×5) hcp unit cell with an adsorbed Pt_4 cluster on the hcp region of the moiré, CO adsorption structure (increasing CO coverage, from top to bottom: $0, 1, 2, 3, 4$ CO). CO adsorption energies (per molecule) are reported at the bottom of each structure (E_{ads} in eV). Figure adapted from [1].

Pt−C distances. The top and side view of 7 CO molecules on Pt_7 is shown in Figure 2.16. The CO adsorption energy per molecule is 2 eV similar to the single CO adsorbed on the most stable site of Pt_4. The CO on the central Pt atom is perpendicular with the C−O distance of 1.15 Å and C−Pt distance of 1.91 Å. The deformation of the cluster was not observed even at full coverages: only small increasing in the Pt−Pt bond length was observed, which is due to the tilting of the molecules on the edges of the cluster for decreasing the interaction between them. Furthermore, in comparison with the Pt_7 cluster, the interaction distance of $Pt - C_u$ increases upon CO adsorption, which makes shorter the distance with the C of CO shorter.

summarizing, for small clusters size, our simulations show that a full coverage of CO can be easily reached, with no effects on the cluster structure; moreover, the adsorption energy per molecule is almost independent from the CO coverage.

Coverage	top view	side view
1.00 ML 7CO@Pt_7	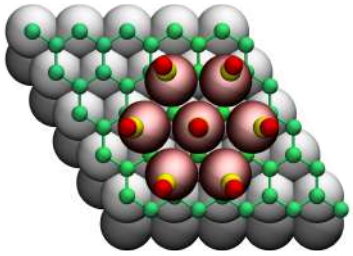	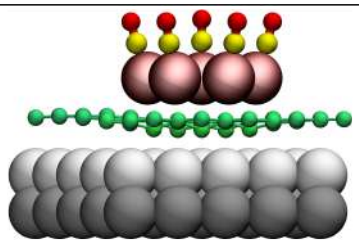 2.00 eV

Figure 2.16: Optimized structure for the reduced model of the GR(5×5)/Ir(5×5) hcp unit cell with 7CO adsorbed on Pt_7 cluster, and CO adsorption energies per molecule (E_{ads}).

- **CO adsorption on Pt_{19}**:

Figure 2.17 shows the optimized structures of Pt_{19} cluster for increasing CO coverage (from top to bottom) up to 0.89 ML. The coverage is calculated by taking the ratio between the CO molecules and the Pt atoms. For high CO coverage on Pt_{19}, a sizable reduction of E_{ads} is found, from 2.28 eV to 1.64 eV, due to intermolecular repulsion. The adsorption of a molecule does not have relevant effects on the cluster shape, apart from a local lifting of the CO bonded to the Pt atoms. This is not general, the adsorbate may induce a change of morphology [71]. Before optimization, the CO molecule was adsorbed perpendicular on the central atom of Pt_{19}. After optimization the molecule was moved on a bridge site, lifting those atoms to 0.56 Å with respect to the pure Pt_{19} cluster (see Figure 2.17, 0.05 ML). However, the scenario changes with the adsorption of more molecules.

When 12 CO molecules are adsorbed, the cluster is more restructured, assuming a dome shape, with the central Pt atoms pulled by about 1 Å more with respect to the bare Pt_{19}. The CO molecules occupying top and bridge sites of the cluster: the bridge molecules are usually adsorbed between those lifted atoms, between lifted and edge Pt atoms or with the other central atoms. Bridges and top sites are occupied also in case of higher CO coverage. The restructuring reduces the number of Pt atoms bonded to graphene , making the nanocluster-graphene interaction weaker. The strong affinity of Pt toward CO may explain the overall energy gain upon CO adsorption and reconstruction of nanoclusters, overcompensating the removal of Pt−GR bonds. As a rule of thumb, while the average strength of the Pt−GR bond is of the order of 1 eV in a flat nanocluster of 5 to 21 atoms, the average adsorption energy of CO is about twice (from 1.6 to 2.3 eV depending on the CO coverage, see Figure 2.15, 2.17, and 2.16). The repulsion between the adsorbed CO molecules may induce the nanocluster restructuring, since a dome-like shape allows larger CO−CO distances and tilting with respect the adsorption on a perfectly flat Pt island.

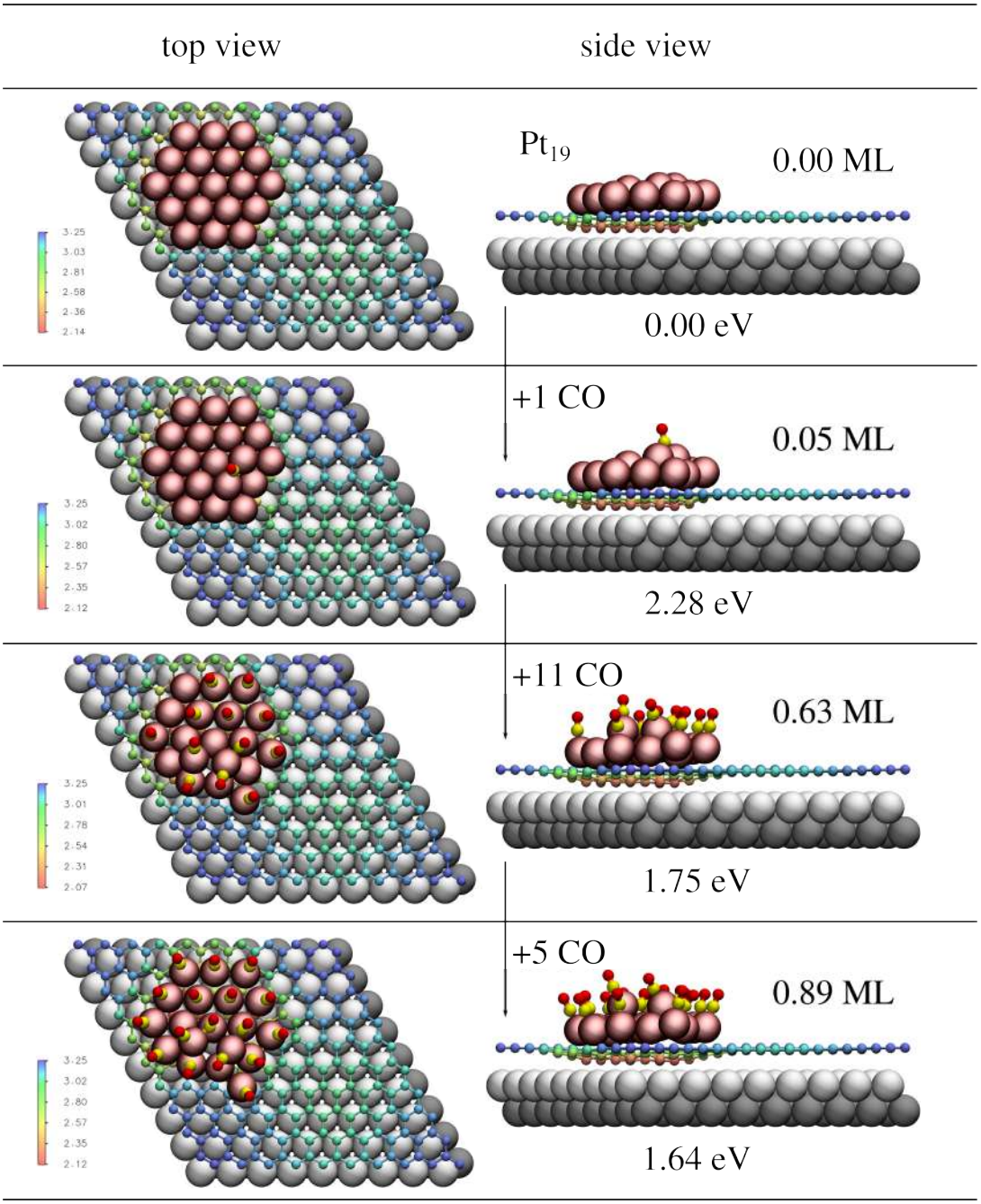

Figure 2.17: Optimized structure for the full model of the GR(10 × 10)/Ir(9 × 10) moiré unit cell with an adsorbed Pt_{19} cluster on the hcp region of the moiré, CO adsorption structure (increasing CO coverage, from up to down: $0, 1, 12, 17$ CO). CO adsorption energies (per molecule) are reported at the bottom of each structure (E_{ads} in eV). The color bar on the left bottom shows the corrugation on the graphene layer. Figure adapted from [1]

The d states of Pt and s and p orbitals of C (both in GR and from CO molecules) are mainly involved in the binding. The most significant change upon CO adsorption occurs for the d states of the Pt atoms pulled up and detached from GR, being shifted toward lower energies (see Figure 2.18).

- **CO adsorption on Pt_{31}**:

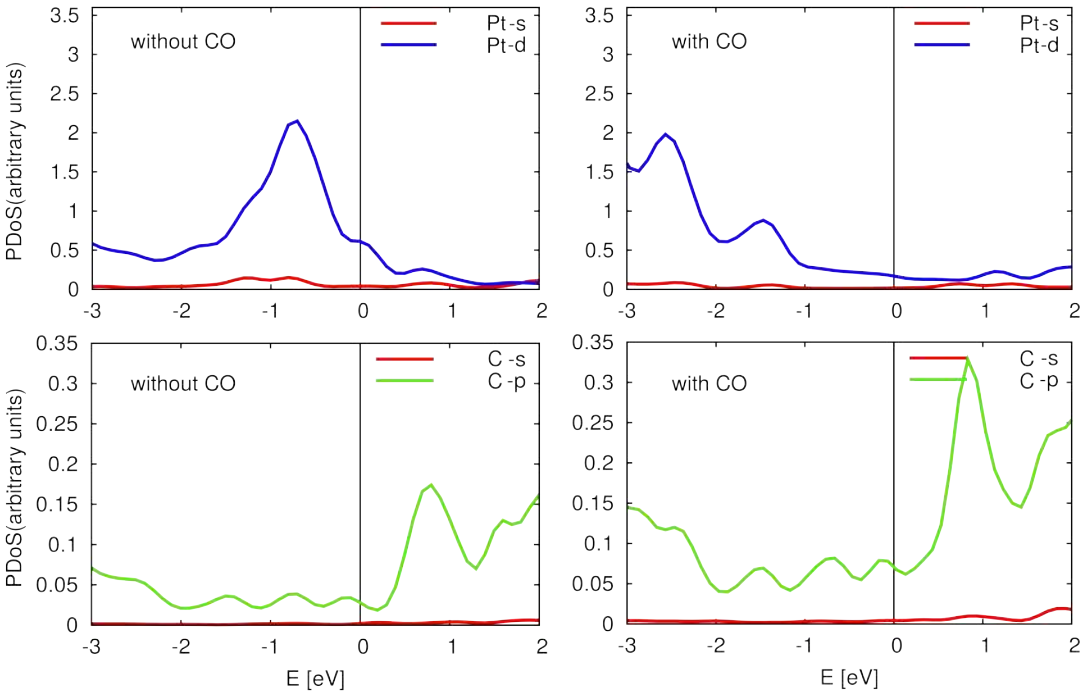

Figure 2.18: Projected Density Of States (PDOS) for selected atoms of the Pt_{19} nanocluster with (right) and without (left) adsorbed CO molecules. Upper panels: Pt atom at the center of the nanocluster, which upon CO adsorption is pulled up and detached from graphene. Lower panels: C atom of graphene beneath that specific Pt atom. The Fermi energy is set at 0 eV.

31 Pt atom cluster, structurally relaxed in the hcp adsorption region on the graphene moiré and covered with 8 CO molecules adsorbed (in a $\sqrt{3} \times \sqrt{3}$ pattern) at Pt in on-top configuration of both the surface layer and edge sites, is reported in Figure 2.19. The adsorption of CO induces a buckling in the cluster structure and repulsive dipole interactions between the ad-molecules yield a tilt of the molecular axes, thus explaining the larger O−O distances measured on small clusters with respect to CO islands on extended (111) facets, and also in line with the observed ripening of the Cu(111) termination upon exposure to high CO pressures [72]. The agreement between the experimental and simulated STM image can be appreciated from the Figure 2.19, where the CO superstructure cell is highlighted in orange. A less bright halo surrounds the clusters in the observed STM image. Interestingly, our simulated images reproduce also this feature: some molecules adsorb in bridge sites across the first and second Pt layers, pointing laterally and therefore appearing lower and darker than those adsorbed in top sites in the uppermost Pt layer and forming the brighter $(\sqrt{3} \times \sqrt{3})R30°$ superstructure.

The peculiar shape of restructured nanoclusters allows the adsorption of CO in different configurations, mainly in nonequivalent top sites (with Pt atoms that are either directly bound to graphene or not) and in bridge sites, as in the case of the Pt_{31} nanoclusters with intermediate CO coverage. These results provide a qualitative rationale for the different peaks in SFG spectra that were discussed in section 2.

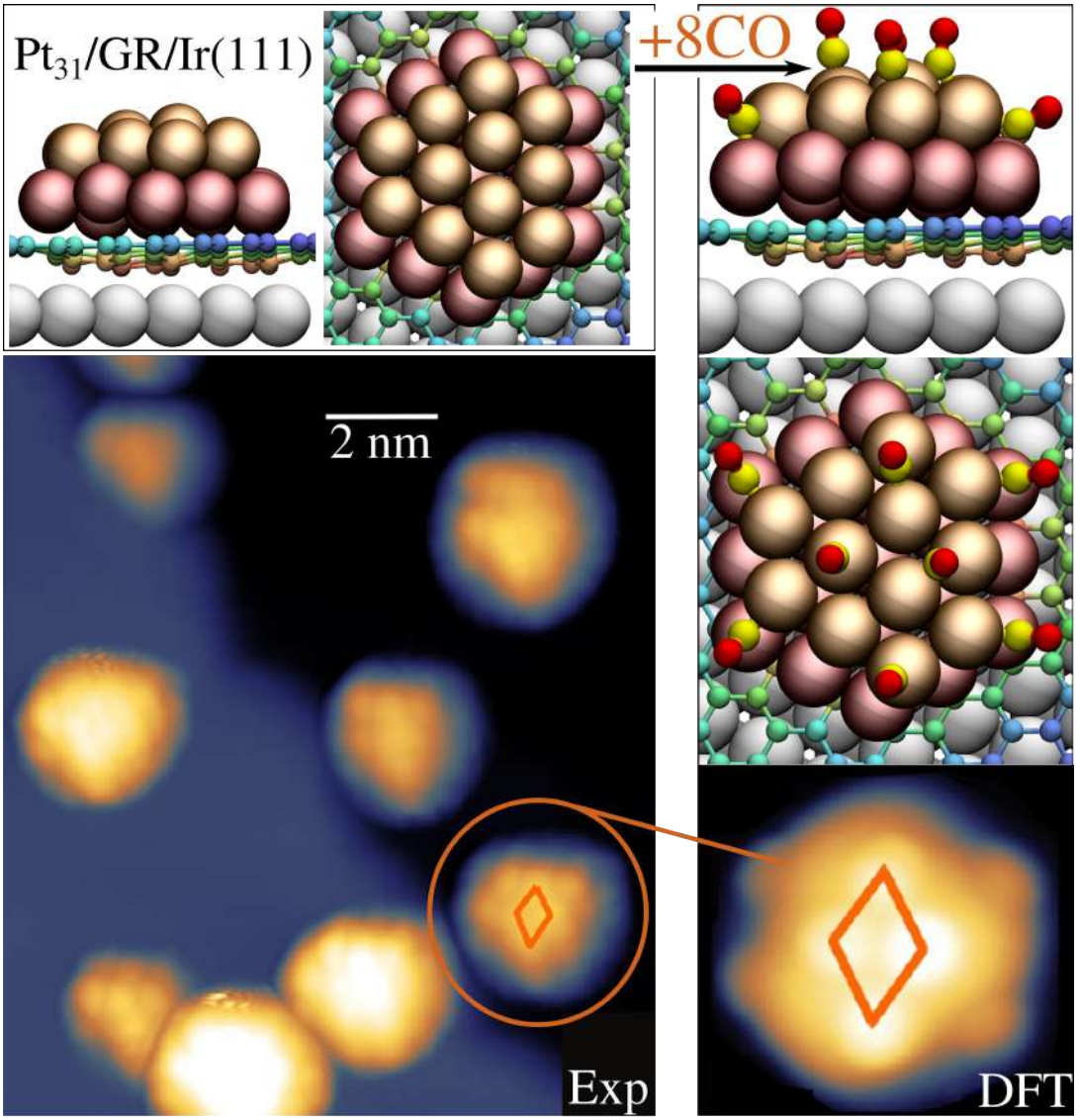

Figure 2.19: Comparison between experimental STM imaging of CO-covered Pt clusters (large image) and DFT simulations (right panel, bottom) of a 31 atoms Pt cluster hosting 8 CO molecules. The left panel on the top shows a model (side and top views) of the fully relaxed cluster structure, including the graphene sheet and the underlying Ir(111) terminal layer; the orange parallelograms indicate the $(\sqrt{3} \times \sqrt{3})R30°$-CO unit cell. adapted from [56]

Chapter 3

Iron phthalocyanines on alumina film

The aim of this chapter is to show, by a combined experimental and theoretical study, the growth behavior of FePc's on $Al_2O_3/Ni_3Al(111)$ at monolayer and multilayer coverage. Until now, the deposition of different metals on this substrate has been investigated [9], [73], [74]. However, for what concerns MPc's, only the self-assembly of Cu(II)Pc molecules on this substrate has been reported to our knowledge so far. While on a low-interacting support as monolayer graphene on Ir(111) MPc's generally form highly ordered almost square lattices, no templating effect has been found for CuPc on $Al_2O_3/Ni_3Al(111)$. Interestingly, the growth of a second layer has been observed before the first is completed [75]. In our work we investigate the self-assembled structure of FePc's on $Al_2O_3/Ni_3Al(111)$, with the aim of clarifying whether it can be used to provide a regular distribution of stabilized single Fe atoms.

3.1 Introduction

Phthalocyanines (Pcs) [76] are square planar organic molecules with chemical formula C32H18N8 that consist of four isoindole units linked by nitrogen atoms. If the two hydrogen atoms in the central cavity of the molecule are replaced by a metal atom, the resulting compound is normally referred to as Metal Phthalocyanine (MPc, MC32H16N8).

MPc's have a structure reproducing the porphyrinic pocket of biological macromolecules and are therefore close to porphyrins. Since their discovery in the early nineties [77], Pc's have become a topic of interest for many experimental as well as theoretical scientists, aiming at understanding the detailed process of the catalytic active part in more complex biological molecules such as chlorophyll and hemoglobin. These molecules incorporate active centers in large organic superstructures and, like in many enzymes [78], the size of the catalytic active part is pushed down to the extreme, basically reducing to single metal atoms. The organic part instead usually handles the interaction with the surrounding molecular backbone and stabilizes the active site. MPc's can mimic at a simplified level both the catalytic active part and the organic structure of biological systems, and can be used in a biomimetic approach to model single atom catalysts

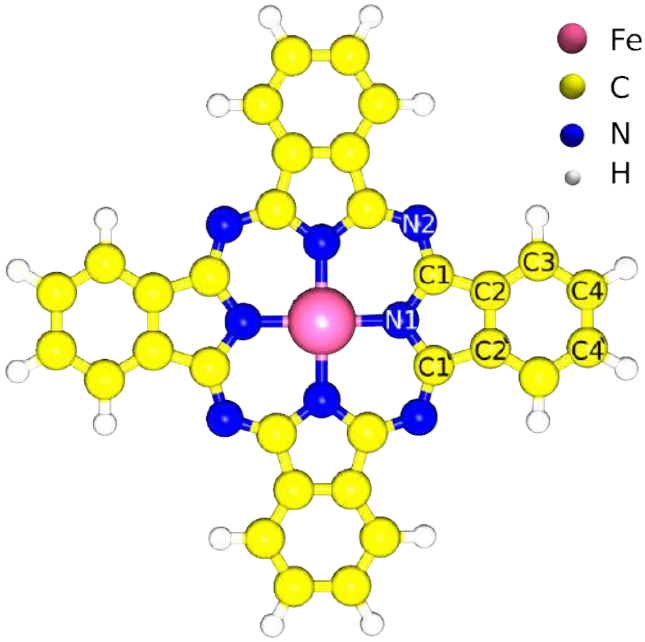

Figure 3.1: Molecular structure of FePc molecule.

(SACs) [79], [80].

Interestingly, Pc's and MPc's have been used as oxidation catalysts [81], organic light-emitting diodes [82], molecular organic photovoltaics [83–85], photosensitizers in dye solar cells [86], organic thin film transistors [87], electroreduction catalysts [88], and many further applications, proving their fascinating technological applicability.

Among many heme-like molecules, the Iron phthalocyanine (FePc) is one of the most interesting species, since it has been proven to act as a good catalyst in oxygen reduction reactions [89]. Great attention has been focused on the adsorption and assembly of FePc's on different metal surfaces [90–101]. However, understanding the behavior and the properties of metallorganic molecules templated by an appropriate support is a critical issue to tune stability, efficiency, and selectivity of the resulting interface. Indeed, charge transfer effects at the metallorganic/inorganic interface of a heterostack may be exploited to govern the properties of the layer, in a competition among lateral interactions, interactions with the support, and trans-effects [102–104]. The symmetry relation of the substrate with respect to the molecules also plays a role in the formation of supramolecular architectures.
The self-assembly of various MPc's has been previously studied combining experimental surface science techniques like Scanning Tunneling Microscopy (STM) and ab-initio Density Functional Theory (DFT) calculations for a thorough understanding of the structural properties of the molecule, adsorption sites, nature of bond, charge distribution between the molecules and the substrate, and interaction between the molecules [90].

3.2 Experimental results

Experiments were performed to investigate the adsorption of FePc molecules on the ultrathin alumina film by means of X-ray Photoelectron Spectroscopy (XPS) and Scanning Tunneling Microscopy (STM). XPS and STM experiments were performed under UHV conditions (low 10^{-10} *mbar*) at room temperature and LN_2 (77 *K*), respectively.
The structure of a thin film of aluminum oxide (Al_2O_3) grown on $Ni_3Al(111)$ was determined using DFT calculations and STM experiments [11], [10]. The unit cell of the oxide film is hexagonal with in-plane lattice parameter of 41.5 Å, and contains some peculiar sites giving rise to two ordered superstructures. One is the "dot" structure corresponding to a hole (oxygen vacancy) reaching the metal substrate (shown as black dots in Figure 3.2), with the same periodicity of the oxide film. The other is the so-called "network" structure (shown as small yellow triangles in Figure 3.2), with two additional sites per unit cell, at a distance of 24 Å one from each other. Top and side view of the DFT model of this structure is shown in Figure 3.2.

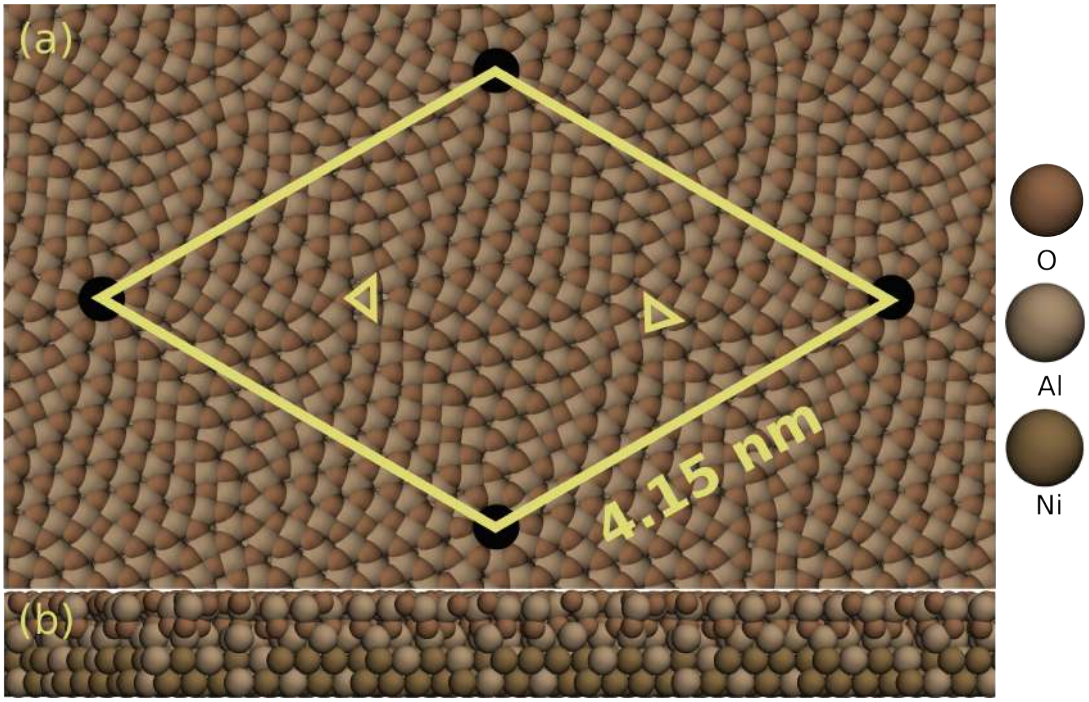

Figure 3.2: Optimized structure of (a) top and (b) side view of the DFT-based model for the $Al_2O_3/Ni_3Al(111)$. Dimension of the unit cell is shown in solid line (lattice parameter = 41.5 Å). The "dot" sites are shown in black circle and the "network" sites are indicated in small triangles.

X-ray Photoemission Spectroscopy (XPS) was used to study the $C1s$ and $N1s$ core level spectra for the FePc molecules deposited on $Al_2O_3/Ni_3Al(111)$ substrate. The $C1s$ and $N1s$ photoemission spectra are shown in the left and right panel of Figure 3.3, respectively. The $C1s$ photoemission spectrum of the FePc monolayer (Figure 3.3, right panel) shows three peak components: two can be clearly resolved and one is quite small, in line with the literature [105–107]. The two clear features are associated to the carbon atoms forming the benzenic (B)

and pyrrolic (P) groups, yielding binding energies of 284.7 eV (B), 286.2 eV (P) respectively, as shown in the (Figure 3.3, right panel). The small spectrum centered at 288.0 eV is associated to inelastic shake-up effects (S). Concerning the nitrogen region, it is known that FePc adsorbed on several substrates exhibit two features that are in most cases energetically unresolved and are centered at about 399 eV with a relative shift of $0.3 - 0.5$ eV. They are associated with the two non-equivalent nitrogen atoms in the tetrapyrrolic ring [105–107]. Accordingly, we fitted the N 1s spectrum of FePc molecules deposited on the pristine alumina surface with two Voigt-shaped features of equal intensity centered at 399.3 eV and 399.0 eV, respectively (blue filled profiles).

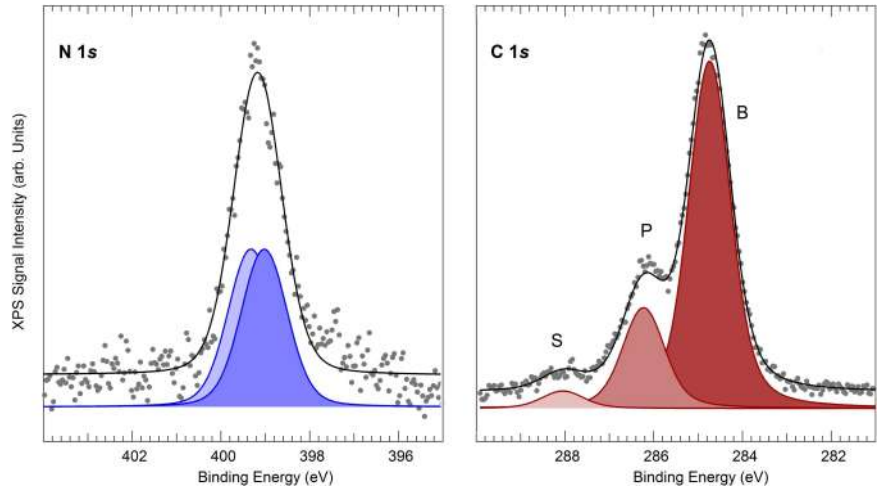

Figure 3.3: N (left panel) and C (right panel) 1s core level spectra collected at room temperature upon deposition of FePcs on the ultrathin alumina film termination; data (grey dots) are shown together with the best fit (black lines) and with the deconvolution (color filled profiles) into the separate spectral components.

The stability of adlayers was also investigated using XPS. Figure 3.4 shows the evolution of the core level intensities and of the core level shifts for both N 1s and C 1s signals as a function of the annealing temperature. Drastic modifications are observed already above 450 K, yielding a shift of the spectral components of more than -300 meV associated with a signal decrease of more than 40 % beyond 600 K. On the basis of the spectroscopic information, we can conclude that desorption of the FePcs and partial decomposition occur already upon mild heating of the layer, thus indicating a relatively poor temperature stability. However, the FePc metallorganic layer is strongly stabilized with respect to the CuPc case, where complete desorption occurs already after annealing to 350 K [75]. On the basis of STM images, a high-density structure was obtained by depositing high coverage of FePc molecules on $Al_2O_3/Ni_3Al(111)$ substrate, showing a commensurate superstructure with a hexagonal unit cell. The new structure is characterized by a hexagonal arrangements of missing FePc sites (”hole” sites), where every ”hole” is surrounded by a hexagon ring of brighter spots. The molecules form a novel ordered structure, characterized by the same unit cell of the underlying alumina template, resulting in regular patterns of FePc vacancies and of Fe ions (see Figure 3.5). The diagonal measures distance between two iron atoms around the ”hole” is 3.1 ± 0.2 nm and is rotated by $21 \pm 1°$ with respect

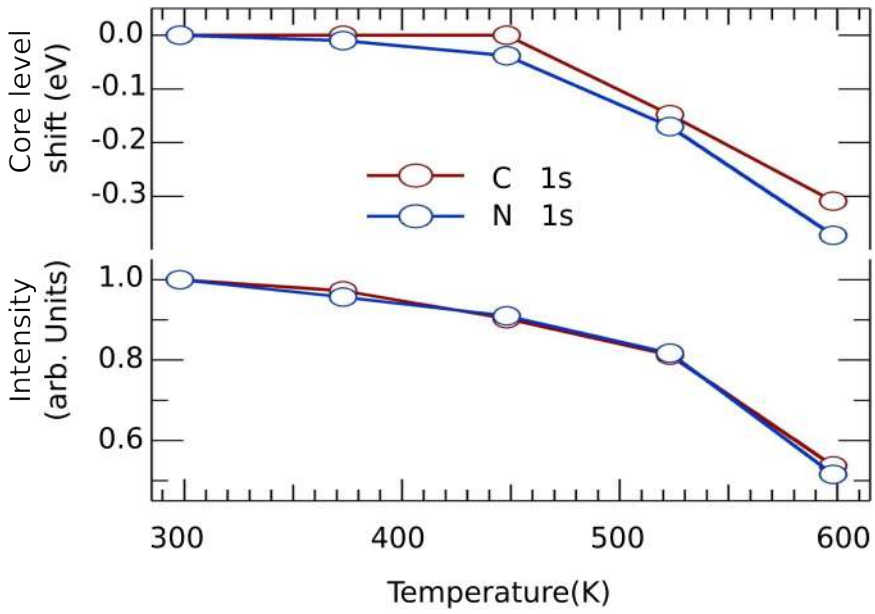

Figure 3.4: Shows the temperature dependence of the normalized core level signal intensities (bottom) and of the relative core level shifts (top).

to the alumina unit vectors. Figure 3.5 b shows the experimental STM images, with regions where bilayers and multilayers are formed. The second molecular overlayer has the same structure and unit cell of the first one. Moreover, the dot-Fe distance around the "hole" was found to be the same with the monolayer case. STM analysis show that FePc molecules adsorbed on an alumina film self-assembled to form hexagonal superstructures in both monolayer and multilayers growth. In the multilayer case, the structural parameters are the same and there is hole-hole correspondence. The relationship between the upper layers and the underlying layers was understood using DFT calculations that will be presented in the last section. These results are in contrast with the CuPc's on the same substrate, where the formation of the second layer was randomly oriented with respect to the first one [75]. The only thing that theoretically should be the same is the fact that Pcs should avoid the adsorption on the holes. For sure the different metal core affects the electronic structure. In the case of CuPc, the alumina template is not strong enough to be greater than or equivalent to the interaction between molecules. In this case the intermolecular forces are much stronger than the molecule-surface bond. While in the FePc case, It may be reasonable that the Fe centers feel more the oxygen atom and so feel better the symmetry of the substrate.

3.3 Theoretical investigation

In the following sections, the adsorption of FePc molecules on $Al_2O_3/Ni_3Al(111)$ were investigated using spin polarized DFT calculations in order to understand the structural properties of the molecule, adsorption sites, nature of bond, charge distribution between the molecules and the substrate, and interaction between the molecules. In addition to the Scanning Tunneling Microscopy (STM) simulation to reproduce the experimental STM images, and also to test the accuracy

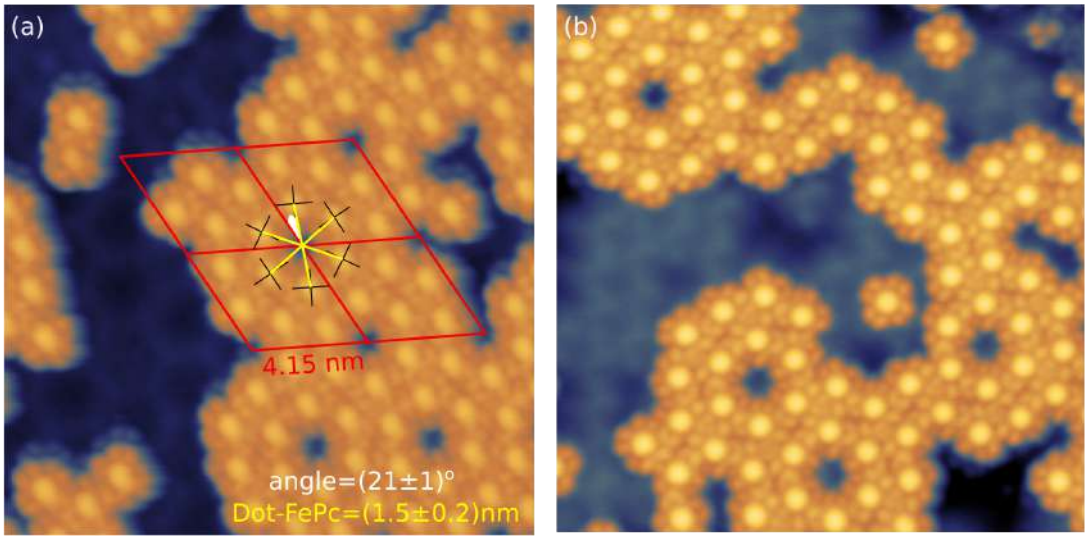

Figure 3.5: STM images of (a) Monolayers, and (b) multilayers FePc molecules self-assembled on $Al_2O_3/Ni_3Al(111)$. The yellow line connect opposite Fe atoms around the "hole", each line makes angle of $21 \pm 1°$ with respect the red line. Yellow lines correspond to the distance of the brigh spots (are shown in black cross) from the center of the hole, and red color correspond to the unit vector of the alumina substrate.

of the models.

3.3.1 Calculation details and structural model

The semi-local Generalized Gradient Approximation (GGA-PBE), including vdW interactions were used throughout. We also examine the effects of a Hubbard corrected energy functional on the electronic d state of Iron. More details will be discuss in the next section.
The DFT model of $Al_2O_3/Ni_3Al(111)$ substrate is shown in Figure 3.2. If the substrate is described by two layers of $Ni_3Al(111)$ under the Al_2O_3 thin film, the minimum size supercell contains 1257 atoms. To reduce the computational effort, the interaction between a single FePc molecule and the $Al_2O_3/Ni_3Al(111)$ substrate was simulated using reduced models cut from the substrate in the most preferable regions (around the "dot" and the "network" sites), without the full periodicity (see Figure 3.6). Taking into account the stoichiometry of the system, we made a cut of almost circular region with a radius of 11.82 Å and 11.55 Å from the center of the "dot" and the "network" regions respectively. A total of 385 atoms (205 atoms for the alloy and 180 atoms for the alumina) and 345 atoms (148 atoms for the alloy and 197 atoms for the alumina) surrounded by vacuum have been considered respectively around the hole (Figure 3.6 a) and the "network" (Figure 3.6 b) sites.
The reduced models of the substrate, with only one molecule adsorbed, were placed in a 31.02 Å × 31.02 Å × 26.07 Å hexagonal supercell, large enough to avoid interaction among the repeated images of the molecule. The full optimization of the molecular structures has been carried on, while the substrate was kept fixed.
The plane wave basis set was truncated at a kinetic energy cutoff of 30 Ry (300

Ry for the charge density). The Methfessel-Paxton smearing technique with an energy broadening of 0.02 Ry was used. Due to the large cell size, only the Γ-point was used for the Brillouin zone integration. Ionic coordinates were optimized to a convergence tolerance of 0.1 $eV/\text{Å}^{-1}$.

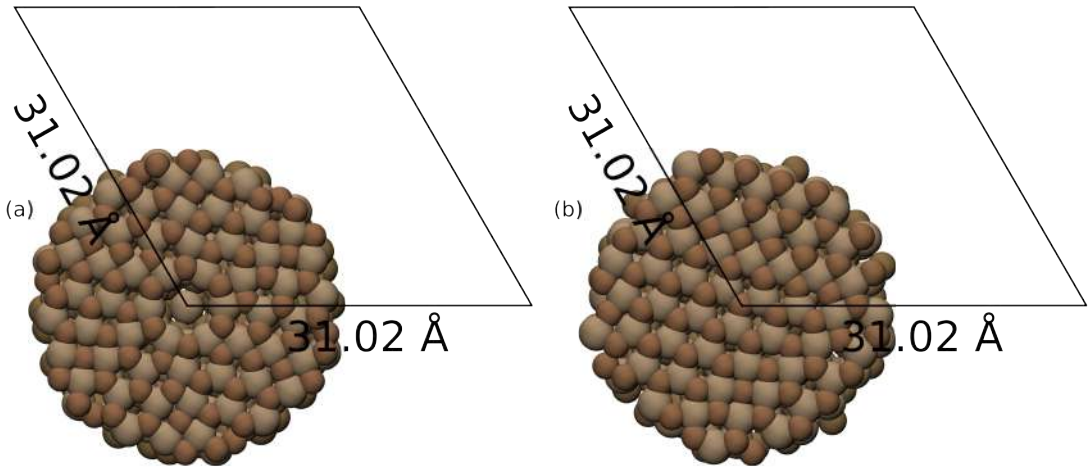

Figure 3.6: Top views of reduced models of the $Al_2O_3/Ni_3Al(111)$. (a) "dot" region, corresponding to an oxygen vacancy, and (b) "network" region. The unit cell is shown in black color.

3.3.2 Adsorption of individual FePc molecule

In this section we are going to report the adsorption of an individual FePc molecule on two different high symmetry regions (shown in Figure 3.6) of the alumina thin film, namely, "dot" and "network" regions. In the "network" region there are different sites (bridge-site, hollow site and O-top site) for the center of the molecule to be placed, as reported in [9], [73] for metallic ad-atoms.
The optimized structure of the isolated FePc molecule was found to be planar with total magnetic moment of 2.01 μ_B/cell, mainly concentrated on the Fe atom. More information about its structural and magnetic properties will be discuss in chapter 5.
The adsorption energy of FePc molecule on $Al_2O_3/Ni_3Al(111)$ substrate was calculated as:

$$E_{ads} = E_{FePc+substrate} - E_{FePc} - E_{substrate}, \tag{3.1}$$

where $E_{FePc+substrate}$ is the total energy of FePc interacting with $Al_2O_3/Ni_3Al(111)$ substrate, E_{FePc} is the total energy of the isolated FePc molecule, and $E_{substrate}$ is the total energy of the $Al_2O_3/Ni_3Al(111)$ substrate.

Figure 3.7 shows the optimized structure of FePc molecule adsorbed on the "dot" and the "network" regions of the alumina substrate. The most stable adsorption configuration for the FePc is on the "network" region (Figure 3.7 b) with Fe atom placed on top of an O atom, similarly to the findings for many metallic atoms [73] and [74]. The adsorption energy on the network site is 2.78 eV. This configuration is also much more stable than the adsorption on the "dot" region (Figure 3.7 a), the adsorption energy for FePc on the O-top site

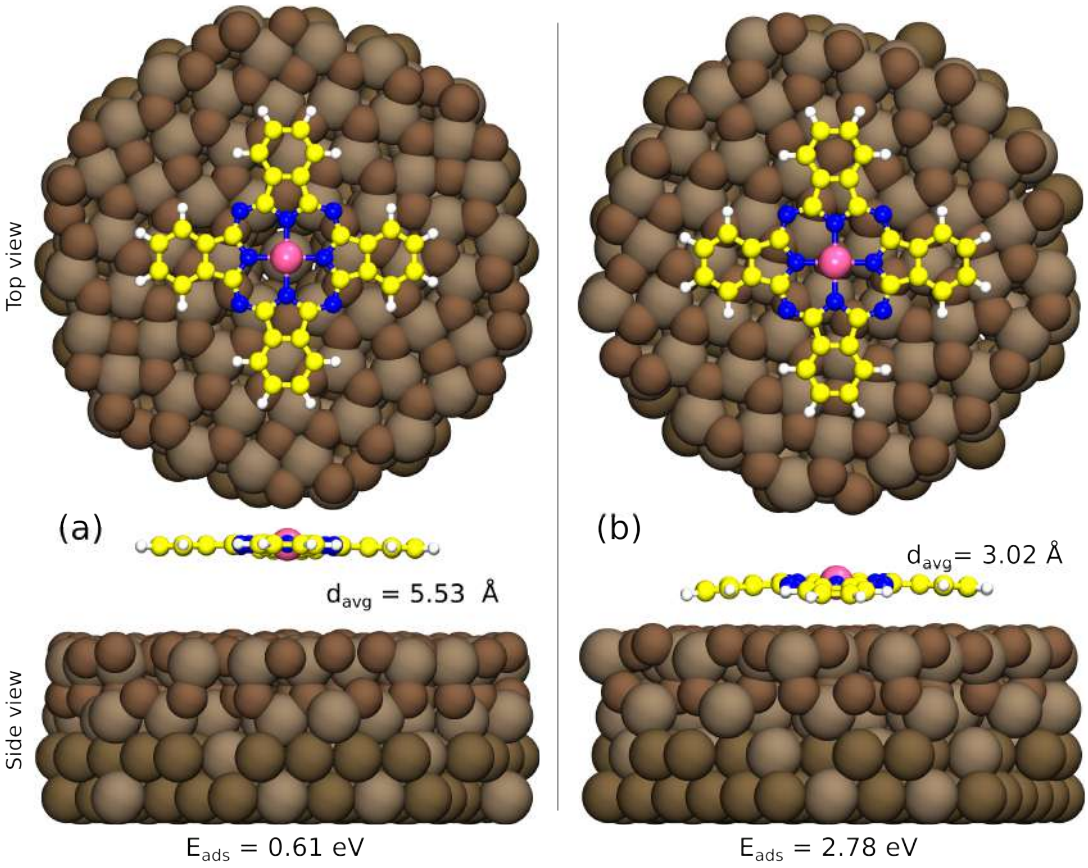

Figure 3.7: Top and side views for the optimized structure of an individual FePc adsorbed on, (a) "dot" region (the Fe atom was placed on the center of hole), and (b) "network" region (the Fe atom was placed on top of O atom) of the $Al_2O_3/Ni_3Al(111)$ substrate.

is 2.17 eV higher than on the "dot" regions. In both regions the molecule is adsorbed parallel to the substrate, but the selective adsorption of the molecule on the "network" region shows slightly distorted configuration, with the pyrroles slightly bent toward the substrate as shown in (Figure 3.7 a). The difference between the z coordinate of the H atoms in the pyrrols and the Fe atom ranges from 0.32 Å to 0.73 Å, indicating a configuration not perfectly symmetric because of the different local registry of parts of the molecule with the underlying substrate. The optimized structure show that the distance of the molecule from the oxide surface is on average 3.02 Å, and 3.27 Å for Fe atom, to be compared with 2.6 ± 0.3 Å for the nucleation of Fe clusters on the same substrate, as reported in ref [74]. Conversely, the average distance of the molecule on the "hole" is 5.53 Å, and 5.63 Å for Fe atom. The magnetic moment of the isolated FePc is 2.01 μ_B, while the FePc adsorbed on oxide surface give 2.25 μ_B for both configurations, with an increase of 0.24 μ_B/cell with respect to the freestanding molecule, indicate a little charge transfer from the molecule to the substrate ($\sim 0.22e^-$). The electronic structure of the adsorbed molecule does not change much with respect to the freestanding molecule, which indicates a physisorption of the molecule on the alumina substrate.

We also studied the adsorption of FePc molecule using GGA+U approximation, to check the effect of Hubbard correction (+U) on the structural and electronic properties of the adsorbed FePc molecule.
In Figure 3.8 we compare the simulated STM images for the individual adsorbed FePc molecule using different values of U (without U(U = 0.0 eV), 1.0 eV, 2.5 eV, 4.0 eV) with the experimental images. The experimental images show large bright spot at the center of the molecule, while the Pc ring appears less bright. Simulated images reproduce well all the features of the experimental images. At U = 1 eV the brightness at the center of molecule dissapear at positive bias near the Fermi energy, this features shift to higher bias as we increase the value of U parameter. It means that, the "+U" correction had influence on the electronic properties of the molecule, in particular, above the Fermi energy. The bright features at the center of molecule can be inferred by studying the PDOS of the Fe d-state, as shown in figure 3.9. As we increase the U parameter, the peaks are shifted toward higher energy, opening a gap near the Fermi energy. This consequently affect the bias at which some specific bright features (for instance, the central spot) appear in the simulated STM images. For U = 3.7 eV and above, the change start appear also for the negative bias.
Concerning the structural properties and adsorption energies: for U= 1 eV, the adsorption energy only decreases by 0.04 eV and 0.01 eV for the FePc adsorbed on the dot and network regions respectively. However, the energy difference between the two adsorption configurations do not change. The structure and the average distances of the molecule from the substrate was exactly the same. Furthermore, the magnetic moment reduced by 0.01 μ_B for both configurations.

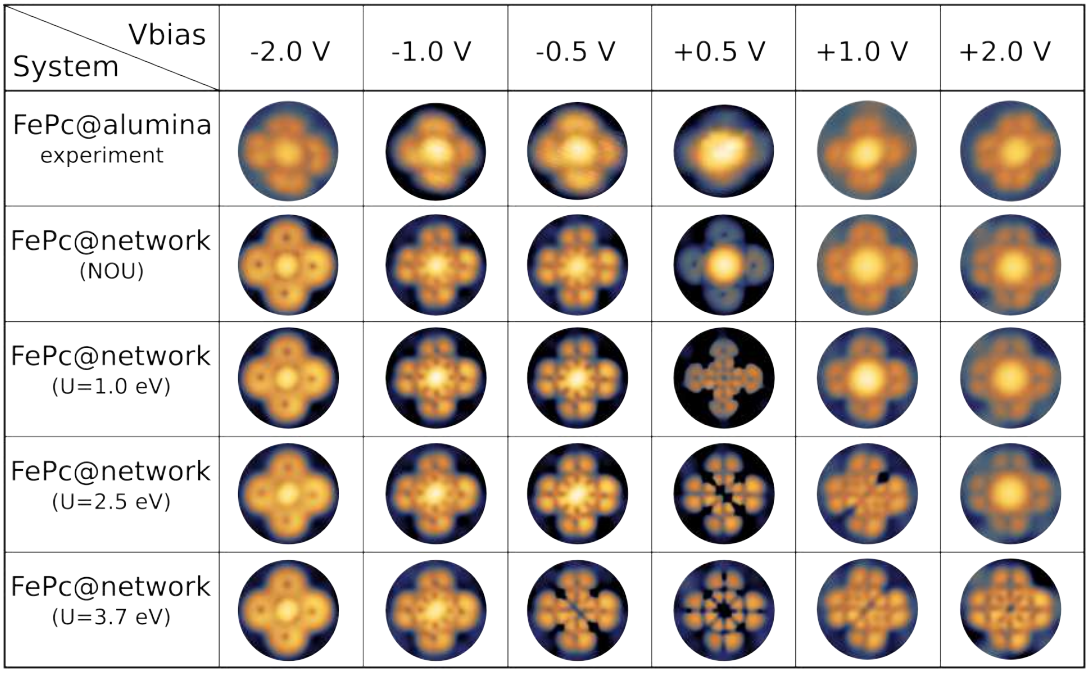

Figure 3.8: Comparison between experimental and simulated STM images of an individual FePc adsorbed on the "network" region of alumina at different bias voltage.

We conclude that the GGA+U (for = 1 to 3.7 eV) does not correctly mimic the experimental STM images close to the Fermi energy. The GGA func-

tional agreed better with the experimental images, as was also reported for the COPc/Ag(111) [108]. Moreover, The "+U" correction had no appreciable effect on the equilibrium structures and adsorption energies. Therefore, only GGA-PBE functional will be use to study the $FePc/Al_2O_3/Ni_3Al(111)$ system.

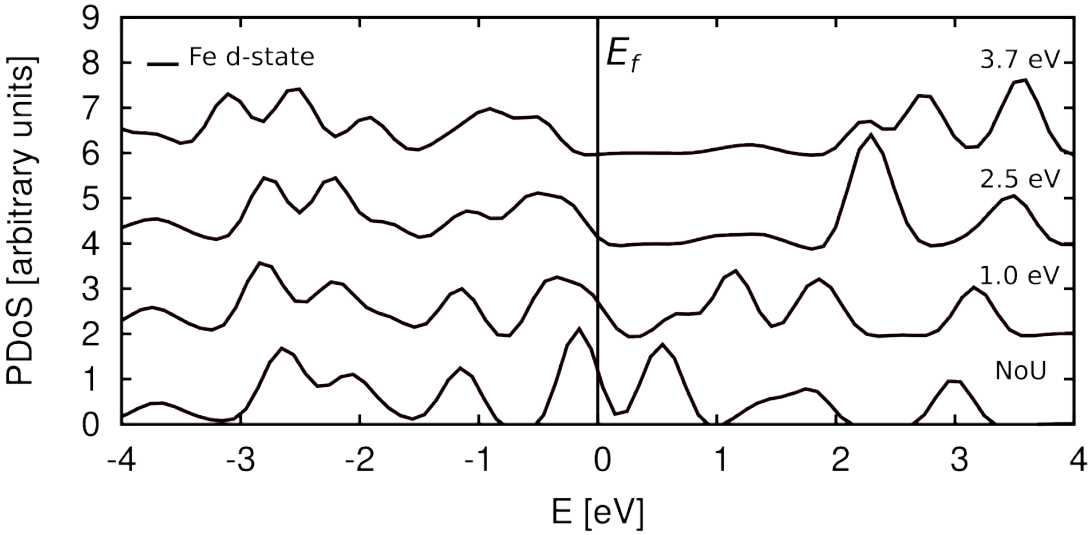

Figure 3.9: Calculated Projected density of states (PDOS) of Fe d-state of an individual FePc adsorbed on the "network" region of alumina at different values of U. The Fermi energy is set at 0 eV.

3.3.3 Monolayer of FePc molecules

Figure 3.10 shows highly ordered FePc monolayer on $Al_2O_3/Ni_3Al(111)$ substrate, showing a commensurate superstructure with a hexagonal unit cell. A structural model for the monolayer is suggested by a close inspection of the experimental STM images, with particular attention to the symmetry of the ordered pattern. After having clarified that the molecular vacancy corresponds to the "hole" in the template, whose structure shows a six-fold symmetry around the "hole", it is possible to identify in the hexagonal unit cell six equivalent adsorption sites around the "hole" where the molecules adsorb, with an ordered pattern and a mutual orientation that is not related to their four-fold symmetry (see Figure 3.10). To precisely identify the molecular structure and the interaction between the molecules, DFT calculations have been carried out to optimize the model shown in Figure 3.10 together with the experimental image. To reduce the computational burdening, only the molecular layer without the substrate is considered.

The interaction between the molecules is shown using the charge difference plot in Figure 3.11 a. The molecules prefer to connect to each other by two hydrogen atoms residing close to the two Hydrogen atoms of neighboring molecules. The molecules are weakly attract to each other with energy of 0.08 eV per molecule, and their mutual minimum distance is 2.13 Å between two closer H atoms in the hexagonal ring around the "hole". In the optimized model, the Fe atoms of the Pc's correspond to the positions of Al-on top sites of the template. The distance from the center of the "hole" to each Fe atom of the hexagon ring

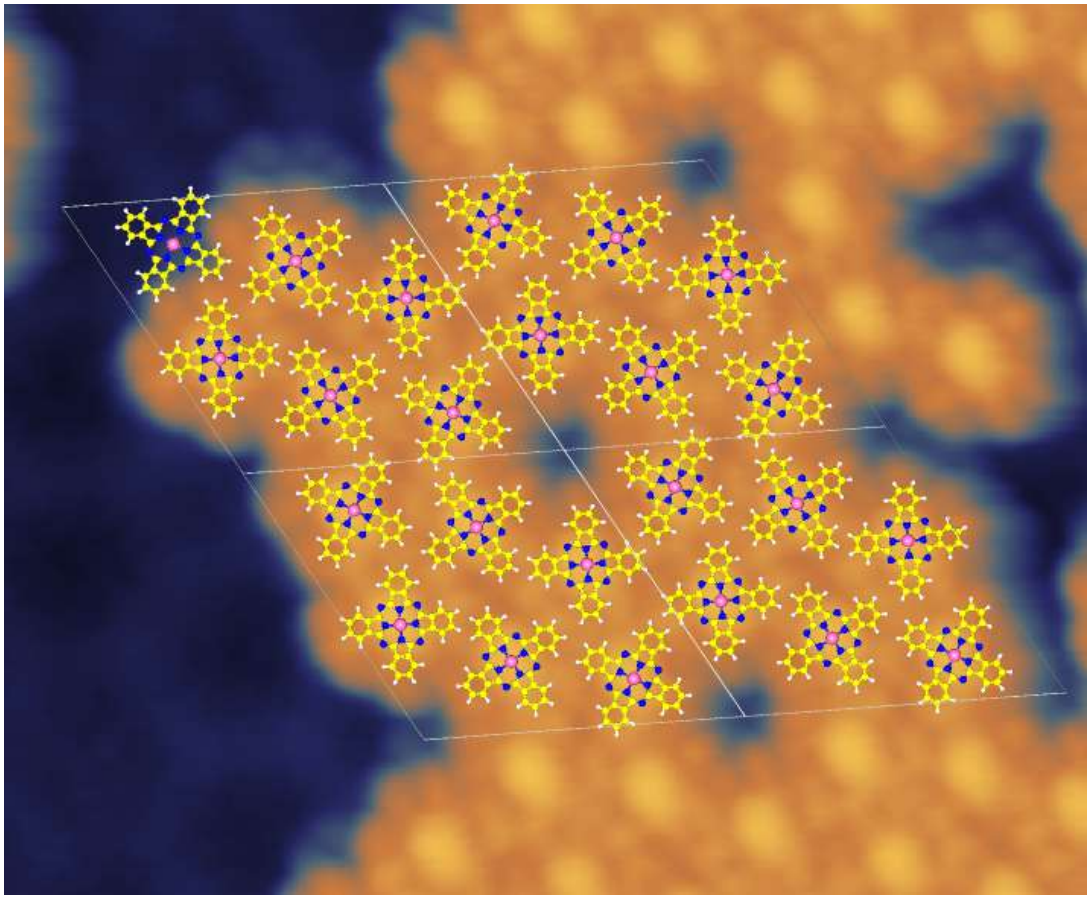

Figure 3.10: Constant current STM images of FePc molecules self-assembled in an ordered hexagonal pattern on alumina thin film at low coverage. The optimized model for 2x2 FePc monolayer obtained by DFT simulations is superimposed to the STM images. STM image at bias = +2 V.

equal to 30.13 Å, which is in agreement with the experimental values. Figure 3.11 b shows the simulated STM images for the hexagonal monolayer, the central dark area is consistent with the "hole" of the experimental STM images.

In conclusion, the FePc's molecules self-assembly on the substrate and form a hexagonal superstructure, due to the molecule-substrate interactions and a very weak attractive molecule-molecule interactions. However, even at supra monolayer coverage, long-range order is not achieved, and the growth of multilayers starts before the first layer is completed. A significant template effect of the substrate introduce different chirality of the molecular layer, that could be function as a new catalyst. In the following we are going to discuss the multilayers formation of the FePc on alumina substrate imaged with STM experiment.

3.3.4 Bilayer of FePc molecules

Experimental STM images revealed the FePc stacking in multilayer films, see Figure 3.5 b. The STM images show a hexagonal superstructure, whose cell parameters similar to the monolayer case. The observed overlayer structure is explained using DFT calculations. In order to determine the stacking of

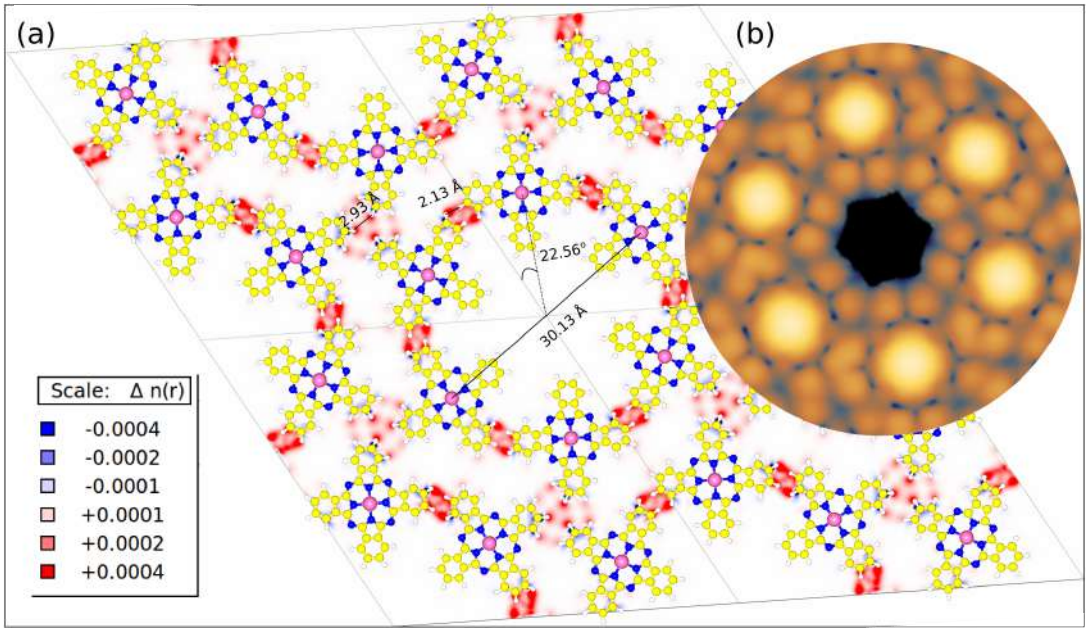

Figure 3.11: optimized structure of FePc monolayer. (a) Charge density difference plot between the 6 molecules within the unit cell charged and neutral. The blue color indicate to a charge lost, whereas the red color indicate a charge gain. The isovalue is set to $\pm$ 0.0004 $|/a_o^3$. (b) Simulated STM image at bias = +2 eV.

FePc molecules in the multilayer film, two bilayers of FePc hexagonal structure were modeled, see Figure 3.12. One with a "face-to-back" (same chirality, one layer exactly on top of the other, Figure 3.12 a) and the other with a "face-to-face" stacking (opposite chirality, one layer flipped with respect to the other, Figure 3.12 b). Among these two different configurations in Figure 3.12, the

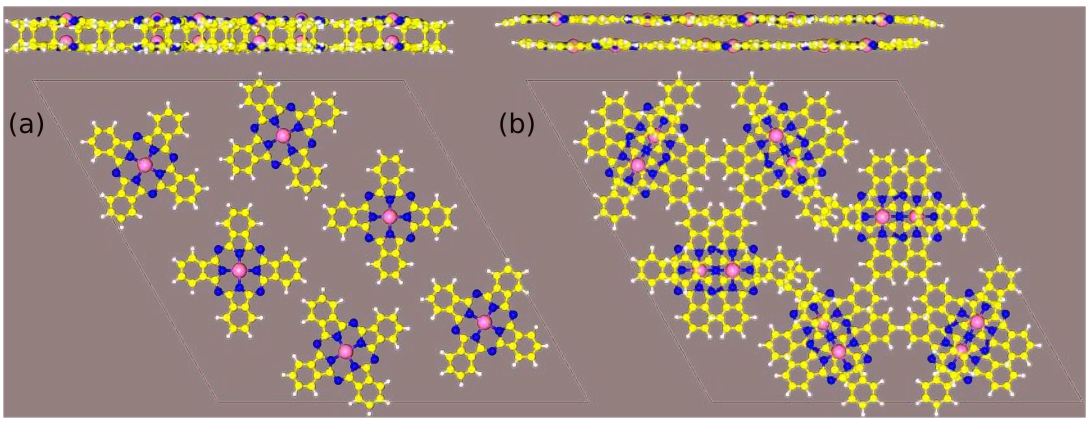

Figure 3.12: Structural models of a FePc's bilayer. (a) A back-to-face superposition (vertical stacking without change of chirality, with one layer exactly on top of the other), and (b) a face-to-face stacking, with a change of chirality. Side/top views in the upper/lower panels.

configuration with "face-to-face" stacking (Figure 3.12 a) is energetically most favored with an attractive interlayer energy of 0.13 eV per molecule. The other configuration where the two layers have the same chirality (Figure 3.12 b) shows a repulsive interlayer energy of -0.69 eV per molecule, significantly unfavorable

with respect to the other configuration. Furthermore, our calculation shows an average interlayer distance of 2.98 Å and 2.67 Å for the stacking with opposite and the same chirality respectively, to be compared with 2.30 Å from the height profile obtained by the STM measurements. For comparison, the interlayer distance was 3.5 Å for the case of CuPc's on the same template [75].

Our calculations show that the FePc molecules lying in two successive layers are not exactly superimposed. DFT model for the topmost layer is shown in Figure 3.13 a. The unit cell is preserved in the case of multiple FePc layers. Moreover, the FePc layer possesses a definite chirality and domains of both enantiomers were observed on the surface. The hexagon ring around the hole sites belonging to the topmost and to the underlying layer are shown in Figure 3.13 a and 3.13 b respectively. In the multilayer formation, FePc switch it's equilibrium orientation 22.56° counterclockwise of the cell axis.

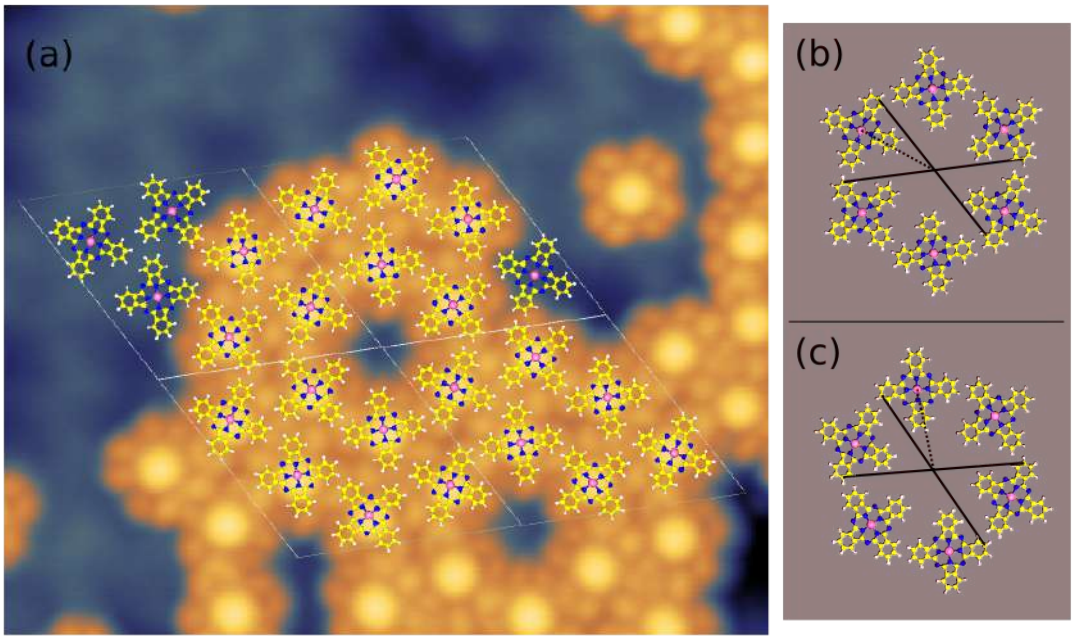

Figure 3.13: (a) Constant current STM images of FePc molecules self-assembled in an ordered hexagonal pattern on alumina thin film at high coverage, the optimized model for 2x2 FePc monolayer obtained by DFT simulations is superimposed to the STM images. The optimized model of FePc molecules around the "dot" site (b) for the same structure at a, (c) the same model with opposite chirality. The dotted line (in b and c) joining two Fe atoms is a guide to the eye to recognize the opposite chirality. STM image at bias = +2 V.

Figure 3.14 shows the simulated STM images for the most stable bilayer structure. The dark area in the STM appearance kept the same, this means that the molecules preserved the same orientations of the First layer. the simulated STM images show good agreement with the experiment.

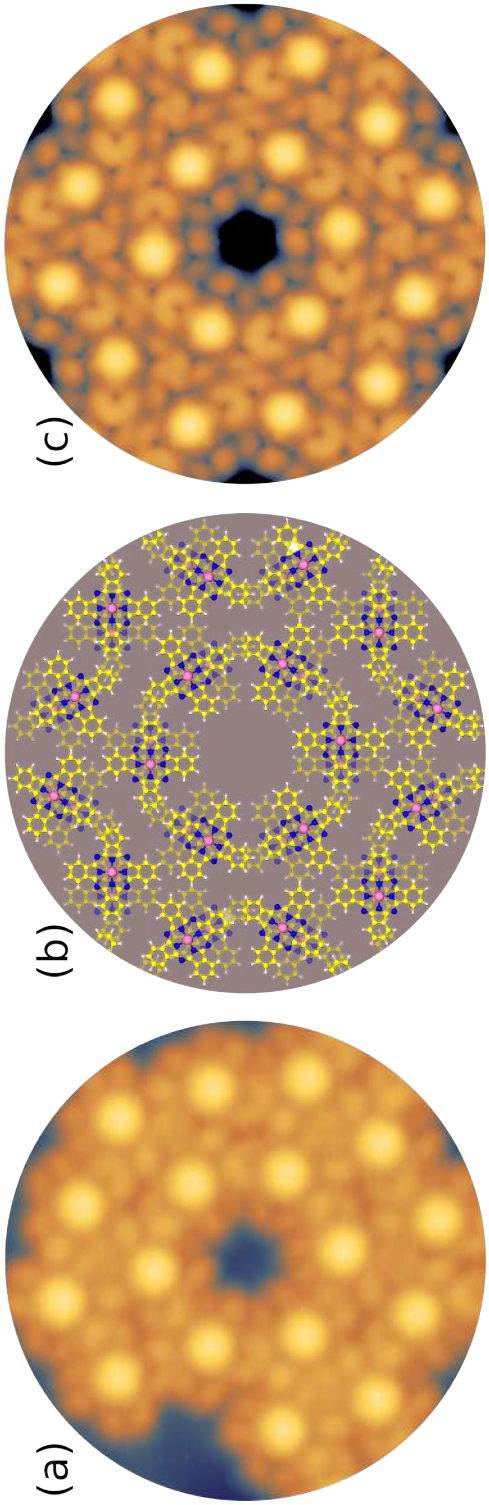

Figure 3.14: STM images of a multilayer region of FePc molecules self-assembled in the ordered hexagonal pattern. The images represent molecules around the "hole" (oxygen vacancy). (a) experimental STM image at bias = +2 V, (b) structural model, with a face-to-face stacking and optimized positions obtained by DFT, (c) simulated STM image at the same bias.

Chapter 4

Tuning Iron phthalocyanines self-assembly

4.1 Introduction

Tailoring the surface chemistry of material can control and tune the binding properties of molecules to the surfaces [109]. As we saw in the previous chapter, FePc molecules present different adsorption energy profile on the alumina template, modulate from stable chemisorption state on oxygen terminated regions to physisorption state on the oxygen and aluminum vacancies [2]. The relative stability of these states can be tuned by modifying the surface potential of the alumina template.

Smoothing the potential energy surface of the substrate can generate different self-assembled molecular layers. Inequivalent self-assemblies of iron phthalocyanines on metal surfaces result in different catalytic properties toward the oxygen reduction reaction, as already shown for FePc's on the Ag(110) surface [110].

It was reported that Cu deposition on the $Al_2O_3/Ni_3Al(111)$ substrate lead to ordered cluster arrays. DFT calculations show that the energetic stability of the Cu on the defective sites (holes) is much stronger than on the oxygen terminated regions (network). In this case the Cu atom is attracted deeply inside the hole and a covalent bond with the supporting alloy is created [9]. Therefore, the presence of Cu adatoms on the holes could smooth the alumina surface and yield different self-assembling of the FePc molecules [3].

Since several important biological centers are made of both (Fe, Mg, Cu, etc.), in this work Cu nanoclusters will be employed to functionalize the alumina surface. In the chapter, we have used the alumina oxide template to investigate the self-assembly of FePcs in the presence of Cu clusters. The dot sites present in the alumina film act as preferential nucleation sites for the growth of Cu nanoclusters. The short range supramolecular formation of the FePc molecules in the monolayer and multilayer coverages on pristine alumina can be controlled by tuning the surface potential of the substrate.

4.2 Experimental results

Experiments were performed to investigate the adsorption of FePc molecules on the $Al_2O_3/Ni_3Al(111)$ substrate in the presence of Cu clusters. The STM image of the pristine alumina film shows the regular honeycomb pattern of the network structure, described as a hexagonal arrangement of dark holes surrounded by smaller hexagonal rings of bright dots as shown in Figure 4.1 a. It was demonstrated that Cu atoms has preferential adsorption inside the "holes" of the alumina template, the adsorption on the "network" side was found to be less stable [9]. A fraction of monolayer of Cu was deposited on the pristine alumina film (Figure 4.1 b) at room temperature. At bias voltage of 3.2 V, STM images suggest that small Cu clusters are homogeneously distributed but are not visible due to low contrast at this bias, while a few intense protrusions, attributed to large size Cu clusters, appear in Figure 4.1 b.
The adsorption of FePc molecules in the presence of Cu clusters was studied using STM and XPS experiments. At low FePc coverage, the large size Cu clusters act as preferential sites for the FePc adsorption, while the small Cu clusters anchored inside the holes of the alumina film do not influence the appearance of the FePc molecules, see Figure 4.2 a. With the Cu coverage of 0.106 ML, instead, a highly ordered FePc monolayer was formed, as shown in the right hand of Figure 4.2. The FePc molecules are form a cross shape pattern with a protrusion at the center, consistent with FePc adsorption on other substrates [111]. This is slightly different with what observed for the hexagonal arrangement of FePc on pristine alumina, in which the molecule exhibit four separated lobes. Almost square unit cell of the FePc monolayer was found in the STM image with unit vectors of 1.40 ± 0.05 nm and 1.50 ± 0.05 nm, with an angle of 98° between the two vectors.

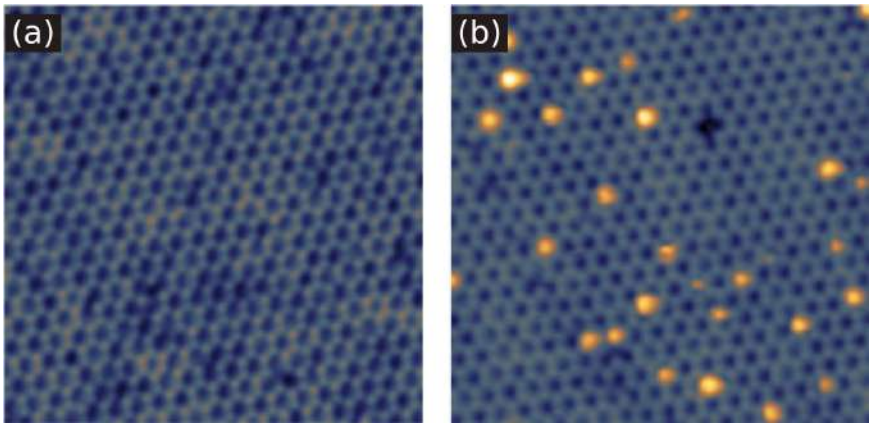

Figure 4.1: STM images collected at [T = 77 K; Vbias = +3.2 V; dimensions of 45 nm × 45 nm]. (a) the pristine alumina film, show the regular honeycomb pattern (bright hexagon) of the network structure. (b) the Cu-decorated alumina film. Bright spots in (b) correspond to larger Cu clusters.

X-ray Photoemission Spectroscopy (XPS) measurements of the $C1s$ and $N1s$ core level spectra were done in order to study the interaction between the FePc molecules and the Cu clusters. The N and C 1s core levels for low FePc coverage (3FePc/alumina unit cell) grown on Cu clusters of selected sizes (6, 10, and 15

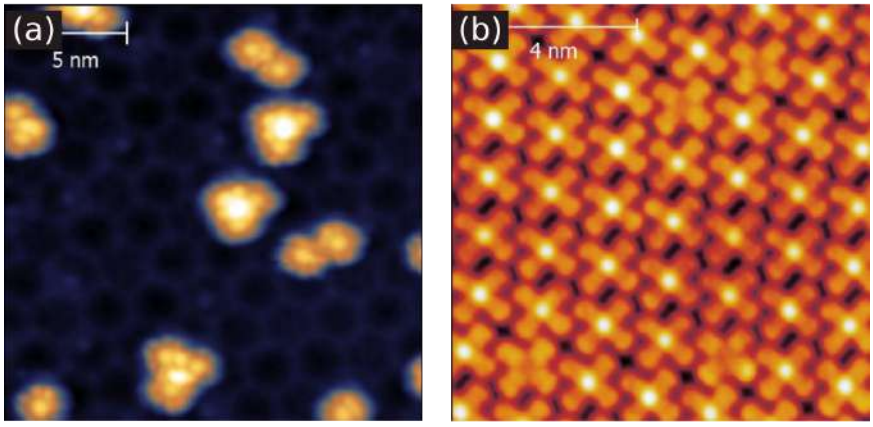

Figure 4.2: Experimental STM images of FePc formed on the Cu clusters on alumina surface at (a) low local coverage [$<$ 0.010 ML; Vbias = +2.0V and dimensions of 20 nm $\times$ 20 nm], and (b) high local coverage [$>$ 0.089 ML; Vbias = $-$0.2V and dimensions of 10 nm $\times$ 10 nm]. Figure from [3].

atoms clusters) are shown in Figure 4.3.
The C 1s spectrum (Figure 4.3-right-panel) for FePc deposited on pristine alumina film consists of three major features as we already reported in chapter 3. When the alumina substrate is pre-covered with Cu clusters, the spectra are successfully fitted by means of two sets of triplets, associated with the FePc molecules interacting with the oxide surface (B_1 and P_1) and with the Cu clusters (B_2 and P_2). The former C 1s triplet is rigidly shifted to lower binding energy by 0.2 eV with respect to the pristine alumina case, while the latter appears at higher binding energy (+0.7 eV). Concerning the N 1s spectra, their lineshape is associated to the two non-equivalent nitrogen atoms in the phthalocyanine molecule. The N 1s spectrum of FePc molecules deposited on the pristine alumina surface is well fitted with two Voigt-shaped features of equal intensity, linked to isoindole nitrogen bonded to the Fe atom, and the azomethine nitrogen bridging two carbon atoms in the pyrrole rings. When Cu is pre-deposited, an apparent broadening of the spectral feature was observed, accompanied by a shift towards lower binding energies, results from the former peaks plus a new peak. The new peaks at 0.6 eV lower binding energy indicate the presence of bonds between FePc molecules and Cu underneath. The signal intensity of these new peaks progressively decreases for increasing Cu cluster size. Therefore, from the core level spectra and in agreement with STM images, it was concluded that the FePc-Cu interaction gradually decreases upon increasing cluster sizes, as indicated in Figure 4.3.

Concerning the temperature effect, XPS spectra demonstrate that an increased thermal stability is achieved when FePc molecules are deposited on the Cu-decorated alumina template. During successive annealing by steps up to 600 K, the overall intensity related to the molecular features decreases faster when Cu nanoclusters are not present on the template.

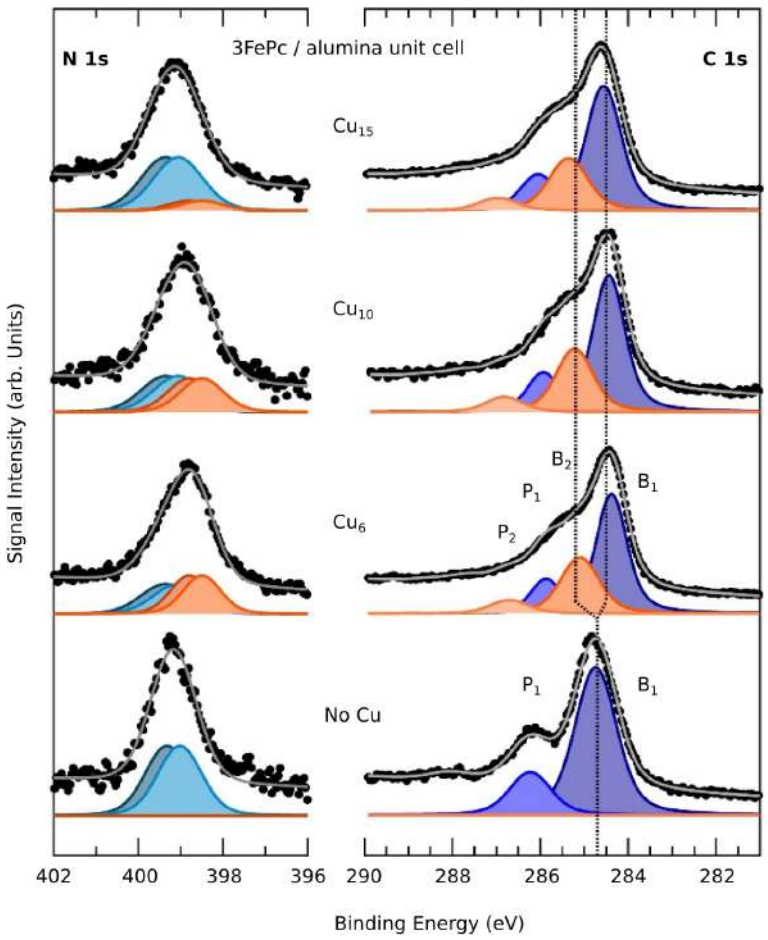

Figure 4.3: Left panel: N 1s spectra collected at 300 K at fixed FePc coverage for increasing Cu loading, from bottom to top [hν = 500 eV]. Right panel: C 1s core level region [hν = 400 eV]. data (black dots) are shown together with the best fit (grey lines) and with the deconvolution (color filled profiles) into the separate spectral components. Blue and orange colors refer to FePc/Al2O3 and FePc/Cu/Al2O3 molecules, respectively. Figure from [3].

4.3 Theoretical investigation

In the following sections, we reported the calculations performed in order to investigate the symmetry and geometry of the assembled monolayer of FePc molecules in presence of Cu clusters.

4.3.1 Calculation details and structural model

Geometry optimizations of all systems were performed using spin polarized DFT calculations with Hubbard-U corrections (GGA+U). In the previous chapter we reported our calculation using only GGA approximation that gave a better agreement with the experimental STM images. In this chapter, since there is a stronger interaction between the molecule and the substrate (mediated by Cu cluster), we have included the Hubbard corrections with U = 1 eV, see the next section for more details. The adsorption system was modeled by a FePc molecule on the reduced model of the dot region proposed in the previous chapter (Figure

3.6, a). The "hole" of the dot region is filled with cluster of two different sizes, a 6-atom Cu cluster (Cu_6) and a 9-atom (Cu_9) Cu cluster as shown in Figure 4.4. A 31.02 Å × 31.02 Å × 26.07 Å hexagonal supercell was used to assure no interaction among the repeated image. The Brillouin zone integration was sampled with a single Γ point due the large lateral periodicity of the supercell. The FePc molecule and the Cu cluster were fully relaxed during the geometry optimizations to a convergence tolerance of 0.1 $eV/Å^{-1}$.

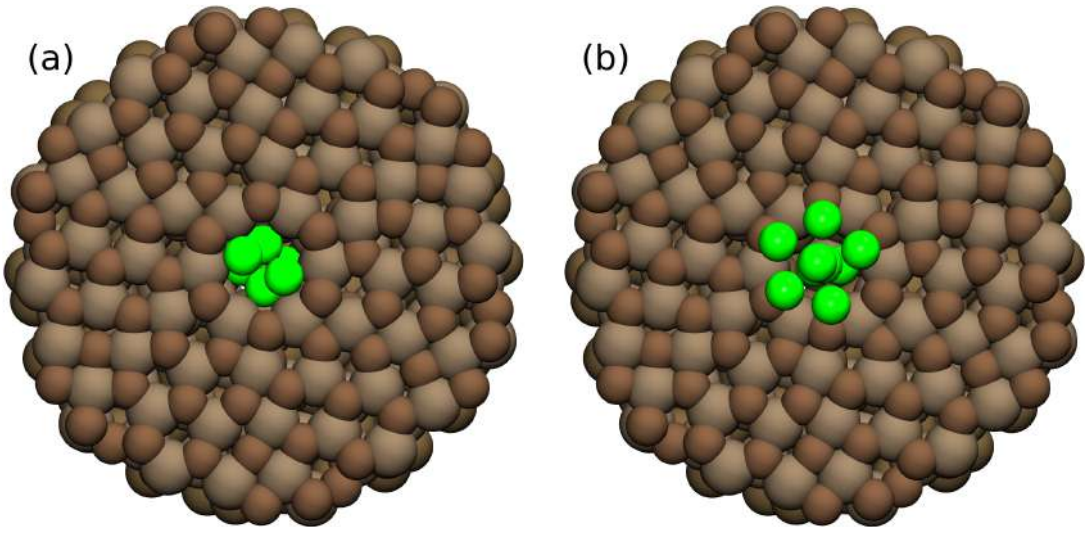

Figure 4.4: Reduced models of the "dot" region of $Al_2O_3/Ni_3Al(111)$ with (a) Cu clusters of 6 atoms inside the "hole", and (b) Cu clusters of 9 atoms inside the "hole".

4.3.2 Adsorption of individual FePc molecule

The side views for the optimized structure of FePc molecule adsorbed on the Cu_6 and Cu_9 on the "hole" site of the $Al_2O_3/Ni_3Al(111)$ substrate are shown in Figure 4.5 (a) and (b) respectively. For small cluster size (Figure 4.5 (a)), the average height of the adsorbed molecule is 3.14 Å away from the alumina substrate and 2.01 Å from the Cu atoms located in the topmost. The adsorbed molecule undergoes a downward bending of the four pyrroles (comparable to the adsorption on the "network" region) due to the increase of interaction between the molecule and the alumina substrate after filling the "hole" with Cu atoms. Concerning the FePc adsorption on 9 atoms cluster, the molecule was found to be planar with average height of 5.53 Å above the alumina substrate (comparable to the adsorption on the "dot" region). The latter is due to the shape and large size of the cluster that we have used. In this case, the apparent height of the cluster above the oxide is 3.19 Å, while it is only 1.08 Å for the case of Cu_6 cluster.

The adsorption energy was calculated using Equation 3.1, where $E_{FePc+substrate}$ is the total energy of FePc adsorbed on $Cu/Al_2O_3/Ni_3Al(111)$ substrate, E_{FePc} is the total energy of the isolated FePc molecule, and $E_{substrate}$ is the total energy of the $Cu/Al_2O_3/Ni_3Al(111)$ substrate.

DFT simulations explore the site dependent adsorption energy of the FePcs molecules. The calculations confirm that the role of the Cu seeds is to allow

adsorption of the ad-molecules at the hole sites. The small Cu nanoclusters act as the preferential adsorption sites. Indeed, an adsorption energy of 3.76 eV is obtained for the binding of the FePc to a Cu_6 cluster at the hole site, as shown in Figure 4.5. This adsorption energy is 1.59 eV higher than that of FePc on "network" region of the substrate. Moreover, a dependence on the cluster dimension is also highlighted, since the adsorption on Cu_9 is 0.50 eV lower with respect to the "network" site and much stable with respect the "hole" site. Therefore, the presence of small Cu clusters on the template make also the dot site favorable for adsorption of FePc molecules. However, the bigger the Cu cluster, the weaker is the interaction with the substrate, as can be seen from Figure 4.5.

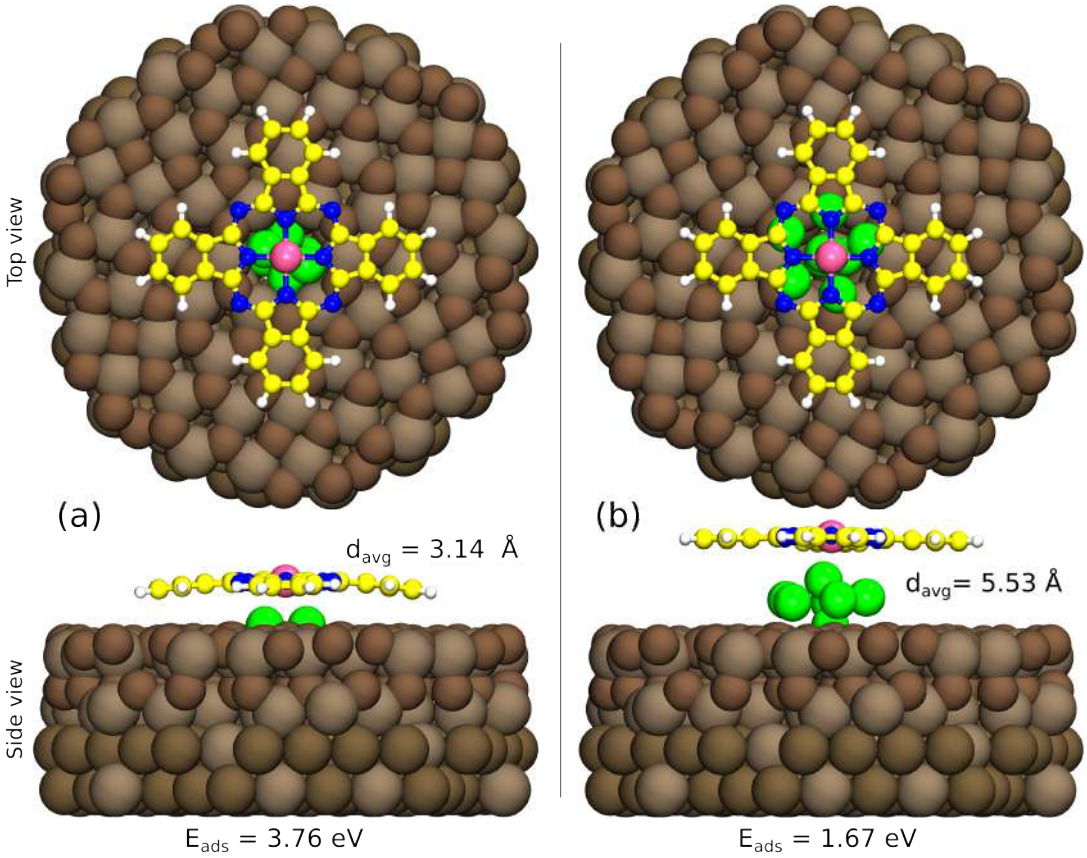

Figure 4.5: shows side view of optimized structure for individual FePc molecules adsorbed on $Al_2O_3/Ni_3Al(111)$. The FePc molecule is centered on (a)Cu clusters of 9 atoms and (b) Cu clusters of 6 atoms. The adsorption energy for FePc molecule together with the average distances from the substrate is also shown; color legend: Fe, pink; C, yellow; N, blue; H, white; O, red; Al, gray; N, orange; and Cu, ice blue. Figure adapted from [3].

Table 4.1 compare the charge transfers analysis for the FePc adsorbed on the pristine alumina and on the Cu cluster with and without U corrections. The charge analysis indicates charge transfers of 0.13 e^- and 0.04 e^- from the substrate to the molecule for FePc adsorption on Cu_6 and Cu_9 respectively. For the former case, the total magnetic magnetic of the FePc changes from 2.05 μ_B in a free molecule to 1.59 μ_B after adsorption. While for the latter case, the magnetic moment changes to 1.90 μ_B. For the FePc adsorbed on the pristine

alumina, no charge transfer was observed, and the magnetic moments are similar to the one of the gas phase FePc molecule.

Table 4.1 also explain the effect of $+U$ correction to the FePc molecule adsorption: we can see that in the presence of Cu cluster, the adsorption energy difference with and without U is 0.15 eV and 0.12 eV for FePc adsorbed on Cu_6 and Cu_9 respectively. Moreover, there is also difference of 0.15 μ_B for the magnetic moment of FePc on small cluster (Cu_6). These differences were not observed for the FePc on pristine alumina. For these reasons we have included the value of U. By choosing small value of $U = 1$ eV (instead of 3.7 eV that was used in reference [29]) to produce well the bias dependence STM experiment.

Table 4.1: Calculated adsorption energy (E_{ads}) in eV, magnetic moment on Fe ($\mu_{Fe}(\mu_B)$), and the total charge on Fe, for FePc adsorbed on Cu clusters (Cu cluster of 6 atoms (Cu_6) and of 9 atoms Cu_9), FePc adsorbed on pristine alumina (at the dot and network sites), and the gas phase FePc (FePc).

system	E_{ads}(eV)		$\mu_{Fe}(\mu_B)$		charges on Fe (e^-)	
	without U	$U = 1$ eV	without U	$U = 1$ eV	without U	$U = 1$ eV
FePc@Cu6	3.91	3.76	1.75	1.60	7.33	7.30
FePc@Cu9	1.79	1.67	1.93	1.88	7.23	7.23
FePc@network	2.78	2.74	2.23	2.22	7.00	7.03
FePc@dot	0.61	0.60	2.25	2.24	7.00	7.01
FePc			2.15	2.11	7.04	7.04

Figure 4.6 shows the spin-polarized PDOS of FePc molecule adsorbed on the network and on the dot region (filled with Cu_6 and Cu_9) of the alumina substrate. The computed PDoS on the benzenic carbon atoms and on the nitrogen atoms are nearly the same, with a little shift with respect to each other. A layer difference is observed in the case of Fe 3d states: the molecule is more perturbed upon adsorption at small clusters. This reflects in a trend in the adsorption energies: the strength of the FePc−Cu bond reduces from 3.83 eV to only 1.79 eV by increasing the Cu nanoparticle size from 6 to 9 atoms (Figure 4.5).

XPS experiments support these findings: different core level spectra were observed and related to FePc interacting with the oxide or the nanoclusters. The features associated to the FePc interacting with the nanoclusters and in particular N 1s, exhibit decreasing intensity for increasing Cu cluster size [3].

Furthermore, the bias-dependent appearance of the single FePc molecule adsorbed on the network region of the pristine alumina and on the Cu_6 clusters was also simulated, and the results are compared with the corresponding experiments in Figure 4.7. The small difference in the electronic states that appear in the PDoS (in Figure 4.6) is not recognizable in the STM appearance of the single FePc molecule with and without Cu clusters. Which means that, the bias-dependent appearance of the FePcs is not affected by the presence of Cu clusters. The overall features of the simulated images are in good agreement with the experiment as shown in Figure 4.7.

4.3.3 Self assembled squared monolayer of FePc molecules

Our calculations confirm that Cu clusters allow adsorption of the molecules also in the dot sites of the alumina template. This functionalization of the template

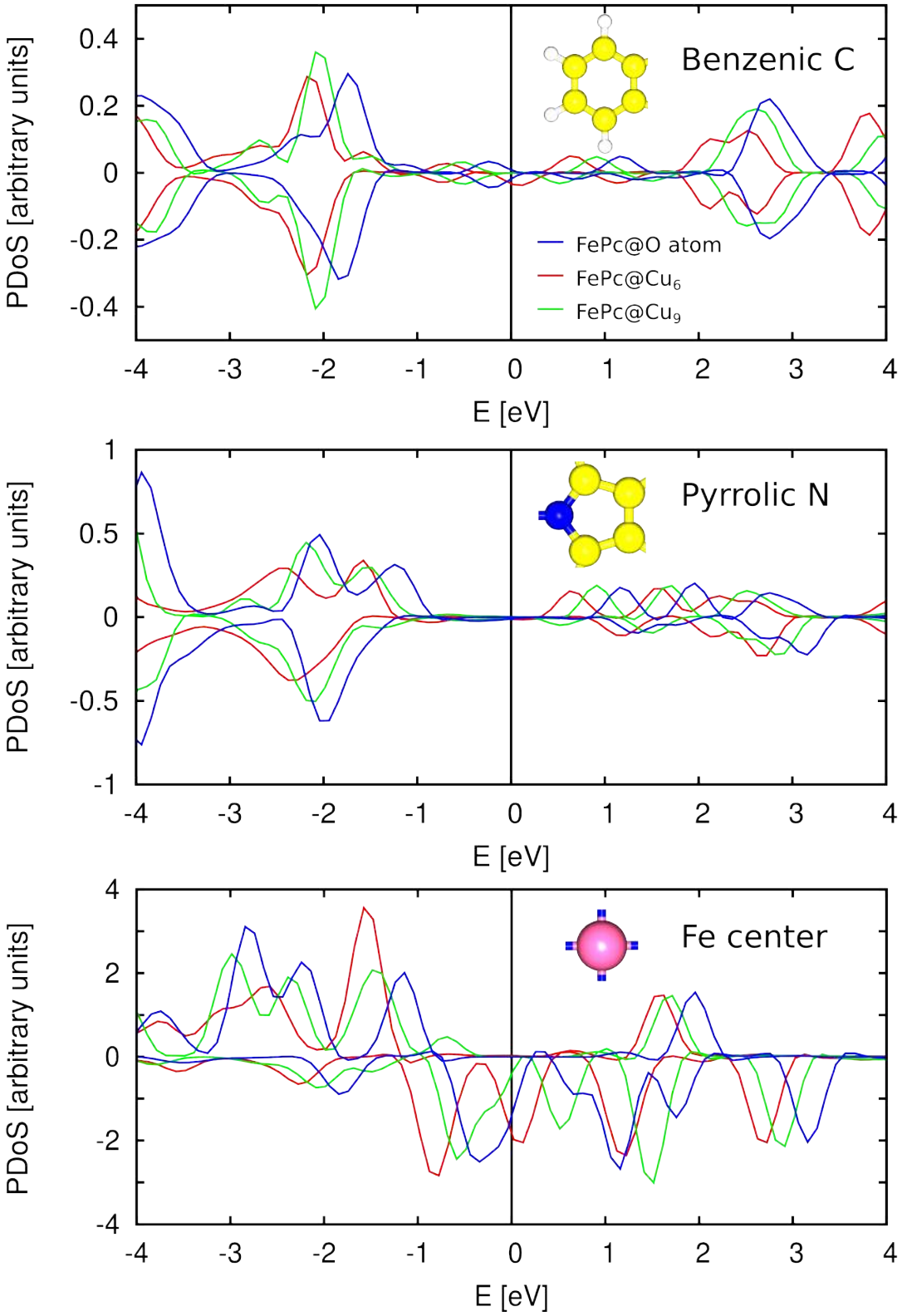

Figure 4.6: Calculated PDoS of (from top to bottom) the p-states of all C atoms of the benzenic rings, the p-states of all N atoms of the pyrrolic rings, and the d-states of the central Fe atom; different colors refer to FePc molecules at different adsorption sites. Figure adapted from [3].

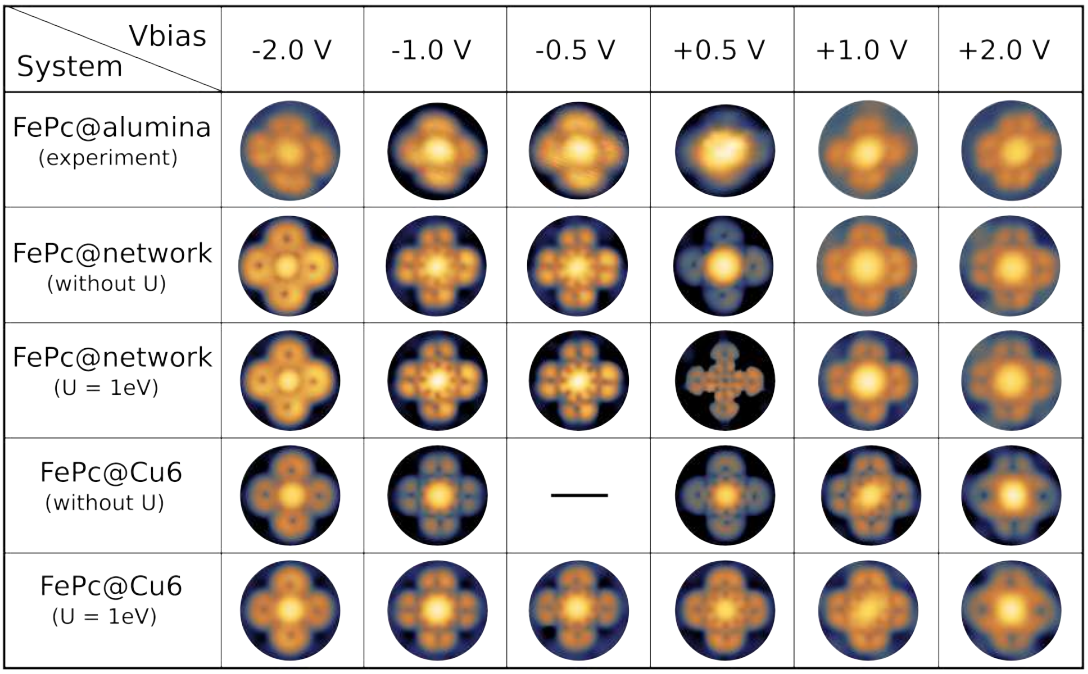

Figure 4.7: Comparison between experimental and simulated STM images of an individual FePc adsorbed on the "network" region, and the "dot" region with Cu clusters of 6 atoms at different bias voltage. Both with ($U = 1\ eV$) and without U calculations are compared. Figure adapted from [3].

tunes the structure of the pattern of the observed molecule from hexagonal in pristine alumina to almost square, as shown in Figure 4.2,b.
Combining our calculations with experimental STM results, we obtain a model for the square structure (shown in Figure 4.8, a) that was formed with a Cu coverage of 0.106 ML. A sketch of the monolayer of FePc is shown in Figure 4.8, (a). The monolayer is placed in a $15 \times 14 \times 15$ Å^3 unit cell with 98° between the x-y axes. The $Al_2O_3/Ni_3Al(111)$ substrate was not included in these calculations. The molecular layer was fully relaxed.
Figure (4.8, b) shows the PDOS of the FePc monolayer that has been used in order to simulate the monolayer STM images. Simulated STM images at different bias voltage (Figure 4.9, bottom panel) reproduced well all the features of the experimental image (Figure 4.9, top panel).
For the majority of the molecules the Fe atom appears brighter than the Pc pyrrole, while few molecules exhibit four separated lobes with hole at their center. These few molecules appear much brighter in their pyrrole, with hole at there center. We refer to them as 'dim' molecules. In order to better clarify the nature of these molecules, additional DFT simulations were performed, and presented in the next section.

Dim molecules

In this section we discuss about the different appearance of some molecules ('dim' molecules) as a function of bias dependence observed in Figure 4.9, only when Cu nanoclusters were pre-deposited on the surface. This population exhibits a completely different bias-dependence appearance with respect to the majority of

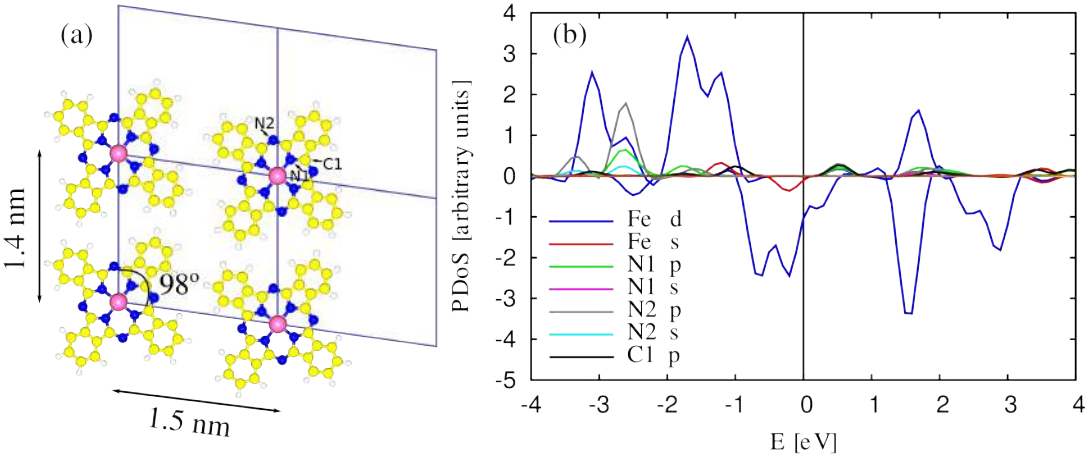

Figure 4.8: (a)Optimized structure of the model formed by (1.5nm×1.4nm×1.5nm) square cell with 98° of angle between the in-plane (x,y) axis. (b) Is the Projected Density of State on the $d(s)$ of the Fe atom, $p(s)$ of the N bonded (N1) and unbonded (N2) to the Fe atom, and the p state of the C1 atom for the structure at (a).

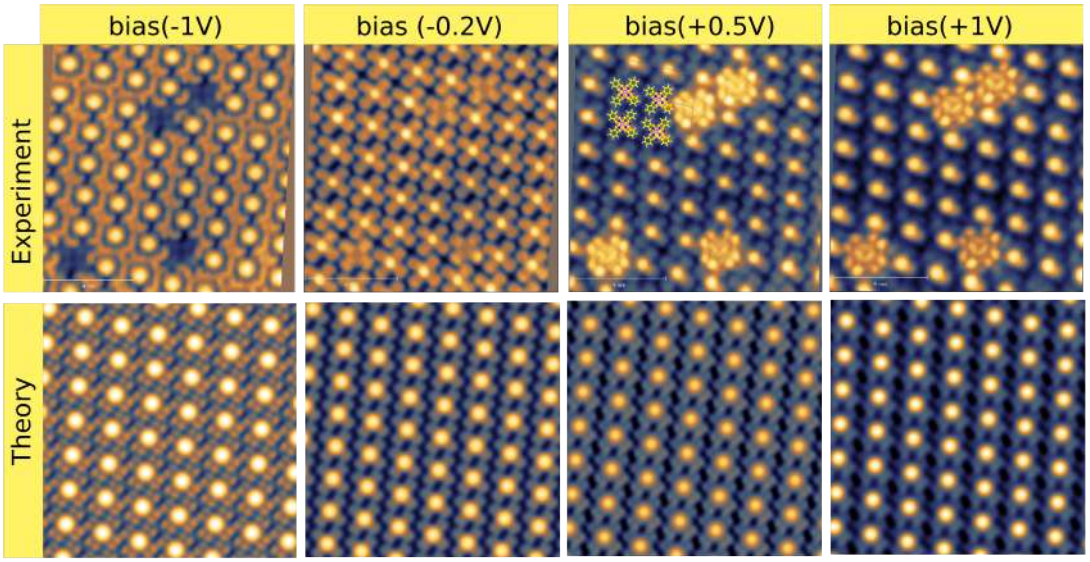

Figure 4.9: Comparison between experimental STM images of FePc square cell observed in the presence of Cu clusters and optimized structure of the model formed by (1.5nm×1.4nm×1.5nm) square cell with 98° of angle between the x,y axis. Figure adapted from [3].

the FePc molecules. The central bright protrusion associated with the Fe atom (shown in Figure 4.7) is absent in the dim molecules (as shown in Figure 4.11). The comparison of the measured dim−dim distances with the periodicity of dot sites (distance of 41.5 Å) excludes the presence of the dim molecules only on the dot sites of the substrate. this implies that those molecules could also exist far from the dot sites.

Moreover, our simulated STM images of single FePC molecule at any bias voltage show a central protrusion associated with the Fe atom (apart from the FePc at O atom at 0.5 V, which has to do with the U correction added to our simulation). Furthermore, large protrusion were observed by STM experiment also in presence of larger clusters. This suggests that larger clusters may not

contribute to the appearance of the dim molecules. On the other side, the dim molecules appears only when the Cu clusters are present in the alumina template.

In order to explain this observation, we simulated different structures of metalated and de-metalated phthalocyanines, and we observed the following:

- The appearance of the dim molecules could be associated to phthalocyanine (Pc) molecules that have undergone de-metalation at the Cu clusters. We simulated STM images of single Pc molecules adsorbed on the network sites of pristine alumina (Figure 4.10,a) and on the Cu_6 cluster (Figure 4.10,b). In both cases, the structural geometry is similar to that of FePc molecules. Considering the energetic stability, we found similar values for FePc and Pc adsorbed on the network site, while at Cu_6 cluster, the Pc was found to be much more stable than the FePc. A similar behavior of Pc molecules upon STM imaging has been observed on the graphene/Ir(111) surface [112].

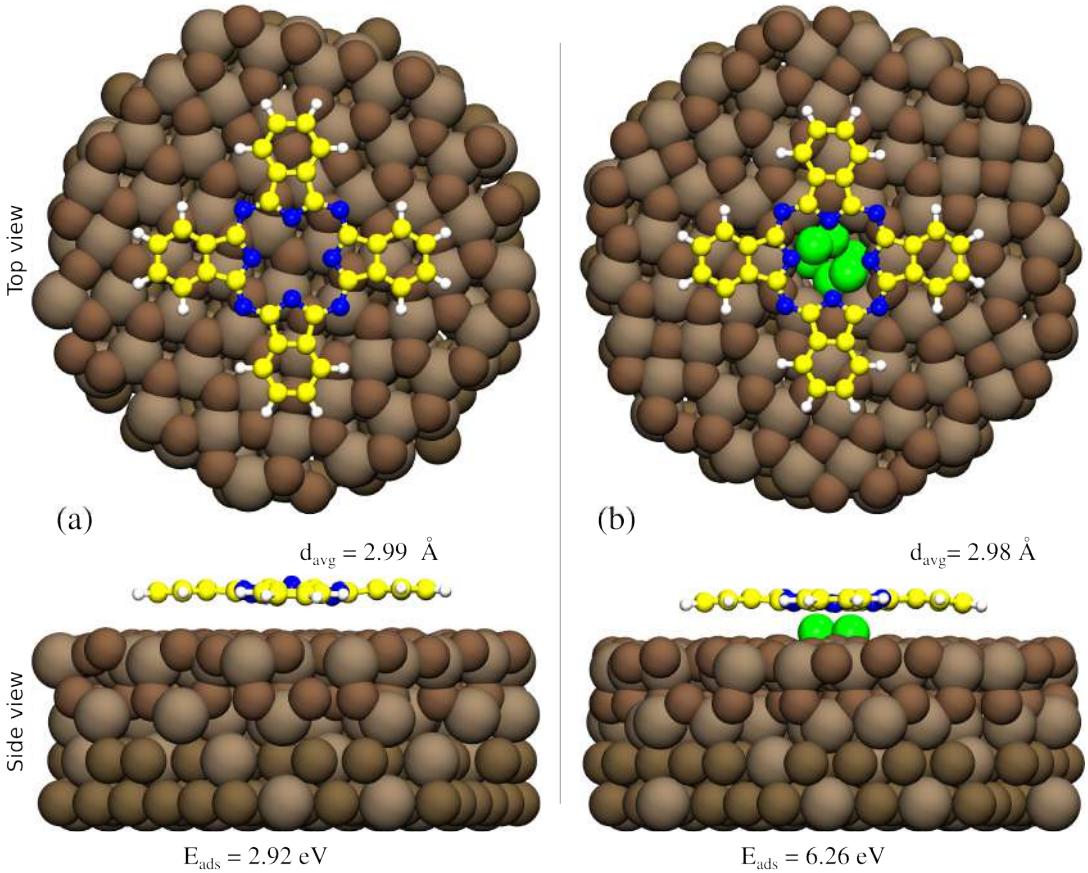

Figure 4.10: shows top and side views of optimized structure for individual Pc molecules adsorbed on $Al_2O_3/Ni_3Al(111)$. The Pc molecule is adsorbed on (a) network side and (b) Cu_6 cluster that fills the dot side. The adsorption energy for Pc molecule (at the bottom of the structure) together with the average distances (at top) from the substrate are also shown.

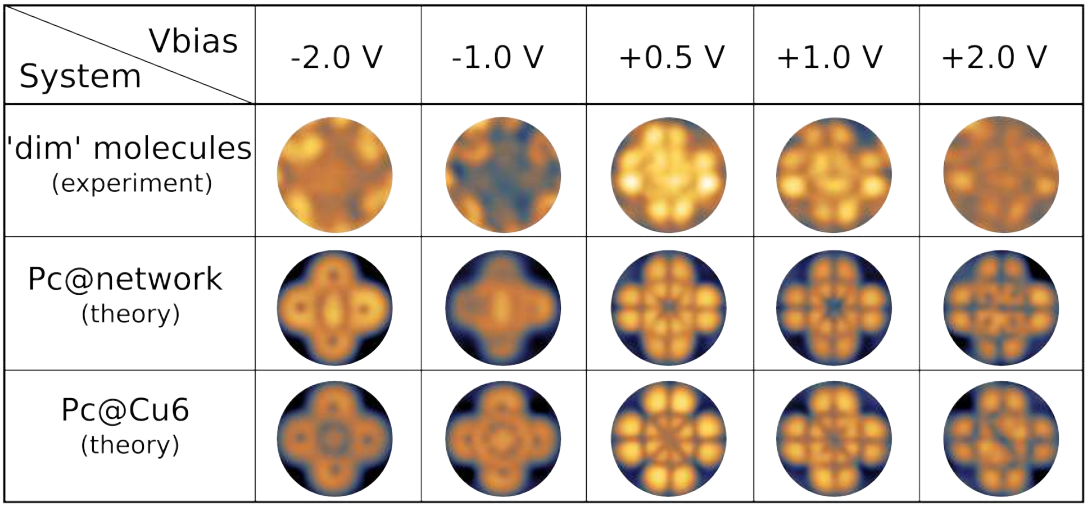

Figure 4.11: 'dim' molecules appearing in the square structure; the disappearance of the central bright protrusion is reproduced by simulating a de-metalated Pc molecule adsorbed either on the oxide surface (Pc@network) or on a small Cu cluster ($Pc@Cu_6$). Figure adapted from [3].

- Furthermore, the simulation of Pc molecule on mixed cluster (Cu_5Fe) has been carried out, as shown in Figure 4.12. Upon relaxation we observed a Fe atom trapping from the cluster to the cavity of Pc molecules. The energy of the new state ($FePc@Cu_5$) is 4.55 eV lower than the initial state ($Pc@FeCu_5$). Because of that, we exclude a metal exchange from FePc to CuPc formation. Moreover, the CuPc would be imaged by STM with a central protrusion [75]. We therefore exclude to attribute the 'dim' molecules to CuPc.

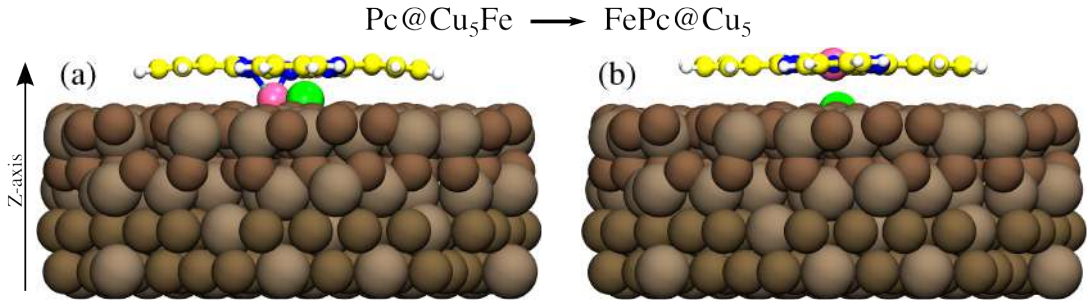

Figure 4.12: Migration of the Fe atom from (a) Cu_5Fe cluster to, (b) the central of the FePc molecule.

- An alternative explanation may be instead ascribed to the interaction between the Fe centers and the underlying O atoms. As the molecular C_{4v} symmetry and the underlying ultrathin alumina C_{3v} symmetry are different, several different, non-equivalent adsorption configurations of the Fe centers with respect to the oxygen-terminated surface are forced by the lateral constraints. While considering the catalytic effect of the FePc/Ag(110) system on the oxygen reduction reaction, Sedona et al.[110] observed that the FePc molecules show a dim, but still metalated center when the Fe

atom interacts with two oxygen atoms in specific adsorption geometries [110]. Therefore, also in the present case, the dim molecules may bind to two oxygen atoms of the underlying oxygen-terminated alumina. Then further simulation could be performed for the FePc on the oxygen terminated regions, in order to better investigate the appearance of the dim molecules.

Chapter 5

Binding of CO_2 onto Iron phthalocyanines

5.1 Introduction

Small carbon-based molecules such as carbon dioxide (CO_2) have a significant impact on climate change and greenhouse effect. This problem can be solved by recycling and transforming CO_2 [113]. Among the possible solutions, heterogeneous catalysis is important to activate CO_2 for its chemical transformations. The development of new catalysts that can reduce the amount of CO_2 emission to the atmosphere, and convert those molecules to produce useful chemicals (like polymers and fuels) is the goal of many scientists [114], [115].
The CO_2 is a linear molecule, all atoms are surrounded by 8 electrons, fulfilling the octet rule. The closed shell nature of this molecule yields relatively small binding energies (of few tens of meV) to reactive surfaces or centers [116]. The adsorption of CO_2 on a catalyst should be strong enough in order to activate the inert CO_2. Different substrates have been studied in order to identify potential catalysts for CO_2 activations [117]-[121]. The activation mechanism of CO_2 is rationalized as follow: when the linear CO_2 adsorb on catalysts surfaces, electrons would transfer to CO_2, elongating the C−O bond and forming a bent CO_2 geometry. The bent configuration may increase by the number of transferred electrons, increasing the reactivity of CO_2, which could lead to further chemical transformations.
Our approach to this problem is based on the biomimetic principles, taking inspiration from the architecture of reactive sites present in biomolecules widespread in nature [119]. For example, a single transition metal supported on porphyrin-like structures acts as a catalyst for enhanced performance and selectivity of CO_2 reduction [122].
The aim of this chapter is to show, by a combined experimental and theoretical study, the mechanism of the CO_2 adsorption and activation on FePc promoted by the electron transfer. Such electron transfer across the graphene-FePc monolayer interface upon oxidation of graphene and close to ambient conditions.

5.2 Experimental Results

Experiment was performed to study the interaction mechanism of CO_2 with FePc molecules deposited on graphene/Ir(111) in presence of O_2. The growth of FePc molecules on graphene gives rise to a regular array of Fe atoms, forming a 2D square lattice. The distance between the two closest Fe-Fe metal atoms was found to be 15 Å [29]. As we have seen in chapter 2, the epitaxial growth of highly ordered graphene monolayers on Ir(111) is characterized by a weak interaction. The presence of the graphene moire$^{'}$ introduces a minigap close to the Fermi level [123]. The Dirac point of the graphene was found to be slightly above the Fermi level at a binding energy of $-0.067\ eV$ [124]. This shift corresponds to a weak p-doping.
Significant changes can occur in the electronic properties of graphene upon oxygen adsorption. The Dirac point can be found above or below the Fermi energy, either by intercalating oxygen between the graphene and metal substrate (p-doping) [124], or by oxidizing the graphene sheet (n-doping) [125], [126]. In the former case, the graphene monolayer is fully decoupled from the metal substrate, with a linear π-band dispersion. While in the latter case, oxidation process causes sp^2 to sp^3 transformation, graphene buckling, a pronounced energy band gap at the Fermi level ($> 0.35eV$), and deformation of the energy wave-vector dispersion from linear to parabolic [126].

X-ray Photoemission Spectroscopy (XPS) was used to study the $C1s$ and $O1s$ core level spectra for the FePc/GR/Ir(111) system during oxygen exposure. The $C1s$ spectrum measured on the clean graphene shows a single peak at 284.01 ± 0.05 (Figure 5.1, lower panel). By exposing the system to 100 $mbar$ O_2, new $O1s$ components appear at $532.5 \pm 0.1\ eV$ (Figure 5.1, upper panel). The $C1s$ component binding energy is shifted to $284.09 \pm 0.05\ eV$, while new components appear at $284.67 \pm 0.05\ eV$, $285.50 \pm 0.05\ eV$, and $286.19 \pm 0.05\ eV$ (Figure 5.1, upper panel). The measured $C1s$ upshift in graphene together with the presence of new components are associated to the graphene oxidation (GRO). This leads to n-doping corrugated graphene, with parabolic energy dispersion and downshift of the valence band below the Fermi level. Opposite behaviour was observed in the case of oxygen interaction between graphene and Ir(111), where the $C1s$ spectrum shows a downshift in the binding energy, attributed to the charge transfer from graphene to the intercalated oxygen, leading to p-doped graphene [124].

IR-Vis Sum Frequency Generation (SFG) spectra including the range of the FePc intramolecular modes, the optical G mode of graphene, and the internal CO_2 stretches are shown in Figure 5.2.

In Figure 5.2 a, the peak located at 1615 cm^{-1} is associated to the graphene optical G mode, while the other two peaks at low energy are due to the normal modes of the FePc molecule. The measured peaks of FePc located at 1335 cm^{-1} associated with the scissoring of the benzene rings, while the peak at 1398 cm^{-1} is related to the tetrapyrrole ring and the isoindoles. Upon CO_2 exposure of the system starting from 10^{-10} $mbar$ and increasing the pressure up to 5 $mbar$ at room temperature, no additional vibrational peaks were observed (see Figure 5.2 b'). Therefore, for given conditions, no adsorption feature of CO_2 on FePc monolayer was observed. When the FePc/graphene system was exposed to

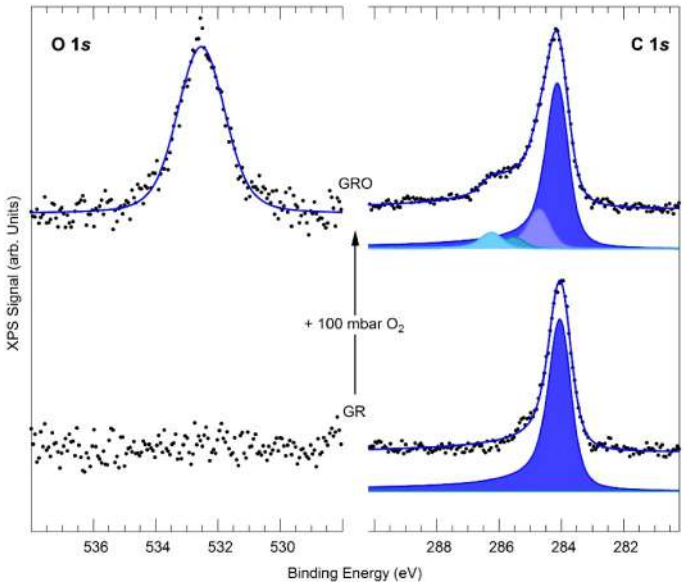

Figure 5.1: XPS data of bare graphene on Ir(111) (lower panel) and of GRO, after oxidation at room temperature in 100 *mbar* O_2 (upper panel). The $O1s$ and $C1s$ core level signals are shown (left and right, respectively) together with the best fit (continuous line) and the deconvolution in the single core level shifted $C1s$ components (filled curves). The spectra were collected ex situ at room temperature in UHV ($h\nu = 1253.6\ eV$).

100 *mbar* O_2, notable increasing in the amplitude related to graphene phonon was observed (see Figure 5.2 b). Exposing the FePc/GRO to 0.05 *mbar* CO_2, two additional peaks grow at 1535 cm^{-1} and 1729 cm^{-1}. These two peaks are associated to the internal mode of FePc and antisymmetric internal stretching mode of adsorbed CO_2 species respectively. When pumping out the CO_2 and recovering UHV conditions, the CO_2 desorbed from the FePc and all spectral features are restored.
Furthermore, the measured phase shift with respect to the non-resonant background of the pyrrolic rings equal to 260 ± 5^0 (see Figure 5.3). After graphene oxidation the relative phase shift lowers to 200 ± 5^0. Morever, the increasing of the CO_2 on the FePc/GRO/Ir(111) system up to 0.05 *mbar* CO_2, leads to further decreasing in the phase shift as shown in Figure 5.3.
Given the above information, we can conclude that CO_2 does not adsorb on the FePc/GR/Ir(111) system, which means that the interaction between CO_2 and FePc is too weak to be suitable for CO_2 activation. Whereas the oxidized graphene (GRO) enhances the adsorption of CO_2. In this case, the CO_2 is expected to bind in bent configuration at the Fe metal center, associated with charge transfer to the molecule.

5.3 Theoretical investigation

In order to understand the experimental evidence (discussed in the previous chapter), two systems have been studied:

1. CO_2 physisorption FePc/GR/Ir(111): we have simulated only a period-

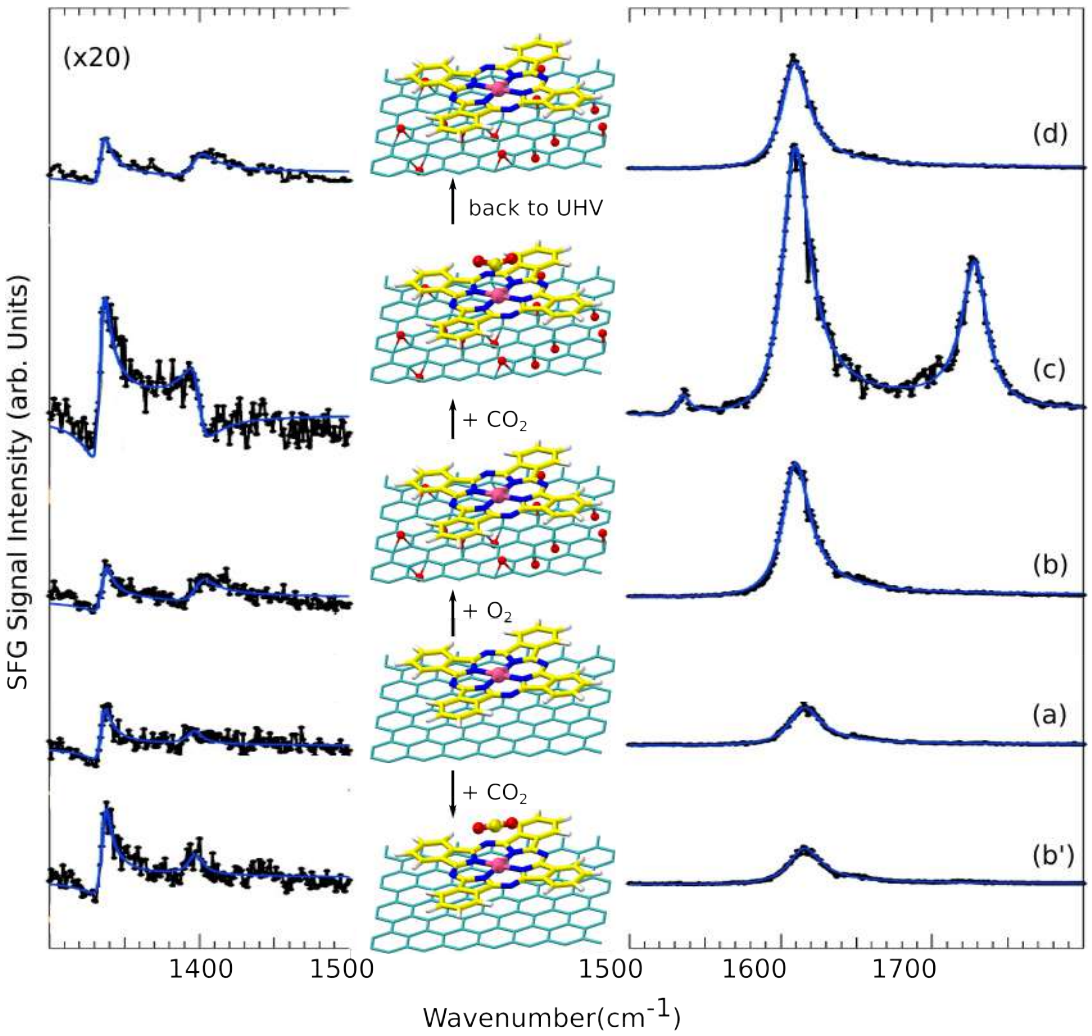

Figure 5.2: IR-Vis SFG spectra of FePc/GR/Ir(111) at room temperature upon increasing CO_2 pressure. (a) FePc 2D crystal on GR/Ir(111) under UHV conditions; (b') in 5 mbar CO_2; (b) after oxidation in 100 mbar O_2 at room temperature; (c) FePc 2D crystal on GRO/Ir(111) in 0.05 *mbar* CO_2; (d) FePc 2D crystal on GRO/Ir(111) after evacuation, back to UHV. The low wavenumber part of the spectra (left) has been magnified for clarity.

ically repeated cell containing a FePc molecule (neutral FePc) without GR/Ir(111) substrate. This is due to the weak interaction between FePc and GR, and to reduce the computational effort.

2. CO_2 adsorption FePc/GRO/Ir(111): as in the previous case, we have simulated this system considering only CO_2 molecule on a FePc monolayer. We reproduced the role played by oxygen exposure, by changing the electronic charges of the FePc molecules (charged FePc), which allows for CO_2 adsorption.

Spin polarized DFT calculations using GGA approximations without and with U ($= 1\ eV$) corrections were carried out (see Chapter 4 for more details about U). In order to investigate the equilibrium atomic geometry, energetic stability as well as electronic structures (in term of charge distribution and PDOS) of the adsorbed CO_2 molecules were calculated. In addition, the vibrational

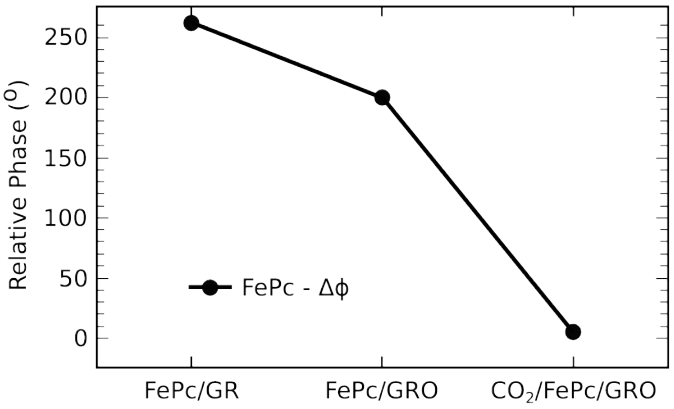

Figure 5.3: Measured relative phase with respect to the non-resonant background of the IR-Vis SFG resonance at 1398 cm^{-1}, for FePc/GR/Ir(111), FePc/GRO/Ir(111), CO_2/FePc/GRO/Ir(111).

modes of CO_2 were calculated, to obtain further information on the strength of and the shape of the local potential at the adsorption site.

5.3.1 Calculation details and structural model

In order to characterize the two systems we mentioned before, we have studied: isolated CO_2, neutral and charged FePc molecules, and CO_2 adsorbed onto both neutral and charged FePc molecules. Two different simulation cells were used to study CO_2 adsorption, one is larger with only one FePc molecule per cell (we refer to it as isolated FePc). The other is a smaller unit cell, also with one molecule per cell with all dimension similarity (we refer to it as FePc-monolayer). For the former case, the molecule was placed in a (31.02 Å × 31.02 Å × 26.07 Å) hexagonal unit cell to avoid the interaction between FePc molecules in the neighboring cell. In the latter case, the FePc molecule was placed in a (14.85 Å × 14.71 Å × 14.97 Å) orthorhombic unit cell. For the latter case, the x-y based on the experimental imaging the monolayer of FePc on Graphene/Ir(111) [29]. For ionic relaxation, we used 30 Ry as the kinetic energy cut-off for wave functions and 300 Ry for charge density, smearing technique with an energy broadening of 0.02 Ry. Γ-point was used in the case of large cell, and grids of (2 x 2 x 2) k-points (shifted by 111) for the square cell. For the latter case convergence has been tested for different k-points with even meshes, up to (8 x 8 x 8) points, including also the Γ-point. However, the differences in the total energy for different K-points with respect to Γ-point sampling is just a few meV. Relaxations were performed until the total forces acting on all atoms were 0.1 $eV/\text{Å}^{-1}$.

It is known that the magnetic properties of metal phthalocyanines depends mainly on the electronic ground state of the central metal (in our case is Fe atom) and are dominated by the *d*-state of this metal [127]. For the relaxation of the FePc system we have started with a certain initiate magnetization on the Fe atom, we end up with a magnetic moment on Fe equal to $0.597\mu_B$ (which is different from the reasonable value of 2.00 μ_B). We repeated the calculations using different initial magnetizations, each time we end up in a different

ground states. We can see that this system exhibit several solutions and it is not guaranteed to fall in the desired global minimum automatically. However, there is no unique or rigorous way to define occupation of localized atomic levels in a multi-atom system [17]. For this reason, we have done several calculations for the system using the same computational parameters and only changing the starting magnetization (between 0.1 and 1) for the system to obtain the lowest energy state. In this case, the total energy of the FePc molecule was calculated for various occupations of the Fe *d*-state as shown in Table 5.1.

Table 5.1: Different occupation of the Fe *d*-state for spin up and down, the magnetic moment on Fe atoms, the total energy value for each occupation (taking the difference with respect to the lowest energy has been reported). the a, b, c, and d referred to the different occupation of Fe *d*-state.

Electronic configuration	dz^2	dzx	dzy	$d(x^2-y^2)$	dxy	$\mu_{Fe}(\mu_B)$	energy (eV)
a-up	0.892	0.591	0.927	0.779	0.703	0.597	-0.684
a-down	0.312	0.763	0.672	0.835	0.714		
b-up	0.984	0.982	0.979	0.861	0.762	2.019	-0.299
b-down	0.500	0.185	0.351	0.820	0.693		
c-up	0.990	0.973	0.973	0.873	0.784	2.102	-0.226
c-down	0.093	0.856	0.859	0.282	0.400		
d-up	0.985	0.972	0.981	0.858	0.758	2.003	0.000
d-down	0.217	0.737	0.192	0.753	0.654		

Table 5.1 shows the different occupations of the Fe *d*-state, the magnetic moment on Fe atoms, and the total energy value for each occupation (the difference with respect to the lowest energy is reported). We can see from the table that the ground state of this system depends on the occupation of the Fe *d*-state, since different occupations leads to different local minimum of the system. Figure 5.4 compares spin up and down PDOS for the four different occupation (a, b, c, and d) reported in Table 5.1. In Figure (5.4 c, d), the PDOS contains partially occupied states at the Fermi level (E_f) which mostly comes from spin-up of dzx state and spin-down of dz^2 state at a and b respectively. Those states are shifted toward the occupied states in Figure (5.4 c, d). In this case the Hubbard correction ($U = 1\ eV$) establishes an insulating ground state with small gap close to the Fermi level. Th occupation with the lowest total energy has been chose as representative of the ground state.

The optimized structures of isolated FePc and of the FePc monolayer (square) correspond to the D_{4h} point group. Simulation analysis of bond lengths and angles are shown in Table 5.2 along with their experimental results [128].

As evident in Table 5.2, the optimized bond lengths for isolated and monolayer-assembled FePc molecules are similar. The agreement with the experiment is within 0.01 Å for the Fe-N1 bond and 0.02 Å for the benzine ring. Regarding the angles, the difference with the experimental data is in 0.01°-0.23° range. The structural properties reported in table 5.2 are consistent with the experimental results in reference [128] and other theoretical results [121],[129].

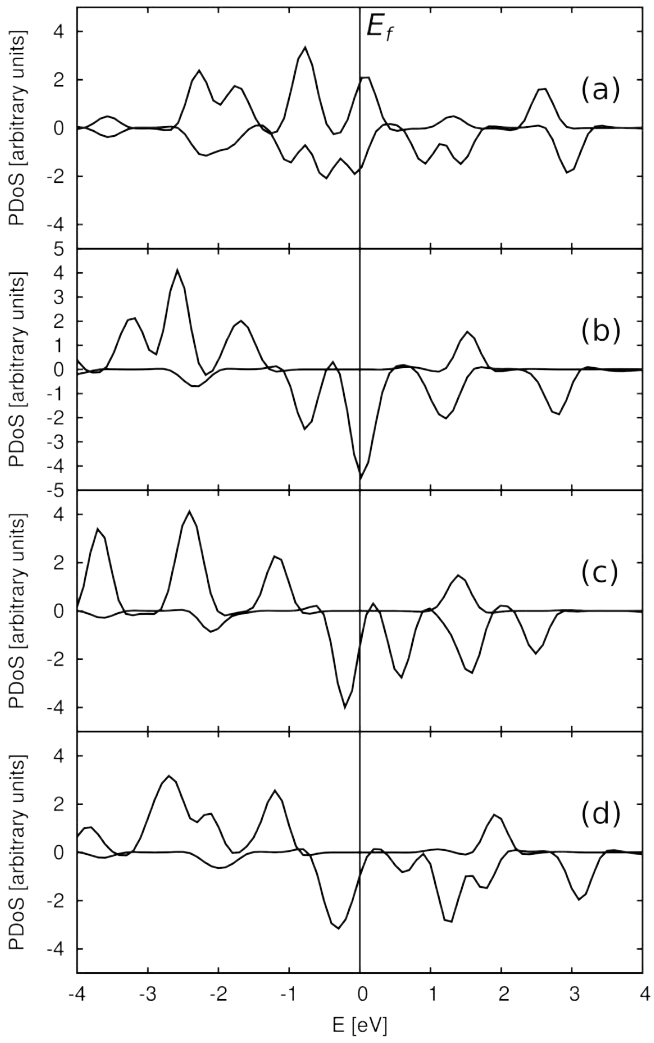

Figure 5.4: Spin up and down Projected density of states (PDOS) on the Fe atom for the monolayer FePc molecules. The a, b, c, and d are the different occupations of the Fe d-state reported in table 5.1. The Fermi energy is set at 0 eV.

5.3.2 CO_2 adsorption on neutral FePc

In this section, we investigated the adsorption of CO_2 onto the isolated FePc molecule. The isolated and adsorbed CO_2 molecule were simulated using the same unit cell of the isolated FePc (31.02 Å x 31.02 Å x 26.07 Å). Geometry optimization of isolated CO_2 resulted in an C-Ô-C angle of 180° and a C−O bond length of 1.17 Å, which is in good agreement with the experimental values of 180° and 1.16 Å [131] and previous theoretical results [120]. The adsorption energy of CO_2 onto different sites of the isolated FePc molecules was calculated as:

$$E_{ads} = E_{CO_2+FePc} - E_{FePc} - E_{CO_2}, \tag{5.1}$$

where E_{CO_2+FePc} is the total energy of CO_2 interacting with FePc, E_{FePc} is the total energy of the FePc, and E_{CO_2} is the total energy of the isolated CO_2 molecule. More negative energies indicates more favourable adsorption configurations.

As the first step, different possible configurations of CO_2 onto isolated FePc

Table 5.2: Calculated structural parameters (bond lengths in Å and angles in degree) for the isolated FePc and a monolayer of FePc molecules; atom labels from Figure 3.1. Experimental data are reported for comparison.

Bonds	Isolated FePc (Å)	FePc monolayer (Å)	Experiment (Å)
Fe-N1	1.94	1.94	1.93
N1-C1	1.39	1.39	1.38
C1-N2	1.32	1.32	1.32
C1-C2	1.45	1.45	1.45
C2-C3	1.39	1.39	1.39
C3-C4	1.39	1.39	1.39
C4-C5	1.41	1.41	1.39
Angles	Isolated FePc (*degree*)	FePc monolayer (*degree*)	Experiment (*degree*)
N1-F$\hat{e}$-N3	89.98	90.01	89.10
C1-N$\hat{1}$-C1`	107.35	107.61	107.20
N1-C$\hat{1}$-N2	127.30	127.41	127.50
C2-C$\hat{1}$-N2	122.97	122.97	122.90
C2-C$\hat{3}$-C4	117.62	117.62	117.00
C3-C$\hat{4}$-C4`	121.17	121.08	121.20
N1-C$\hat{1}$-C2	109.73	109.62	110.00

molecule were studied, in order to identify the favourable adsorption sites and geometries of the CO_2.

Figure 5.5 shows the optimized structures of CO_2 adsorbed onto neutral FePc molecule. Before the relaxation, the molecule was placed around 2 Å far from the FePc molecule. For all the configurations in Figure 5.5, the C−O bond length is 1.17 Å, and the C-Ô-C angle varies from (179.7° to 179.9°) which is very close to the isolated CO_2. Furthermore, the calculated adsorption energies range between $-0.14\ eV$ and $-0.22\ eV$, and the average distances of CO_2 from the FePc molecule range between 2.86 Å and 3.12 Å. The calculated results are reported in Table 5.3. These results indicate that CO_2 interacts very weakly with the neutral FePc molecule, the neutral FePc molecule do not promote the CO_2 adsorption. In agreement with the experimental results (SFG spectra in Figure 5.2) and their interpretation.

5.3.3 CO_2 adsorption onto charged FePc monolayer

In this section we are going to investigate the experimental observation of CO_2 adsorption in the presence of O_2. The effect of GRO on CO_2 activation has been simulated by adding negative charges to the system. We tested the addition of different numbers of charge (starting from $+1e^-$) to the CO_2 on FePc monolayer. We mainly focused on the adsorption of CO_2 on the Fe atom of the FePc center. The CO_2 was introduced to the surface horizontally with C atom pointed on top of Fe atom of FePc monolayer. The optimized CO_2 adsorption geometries on

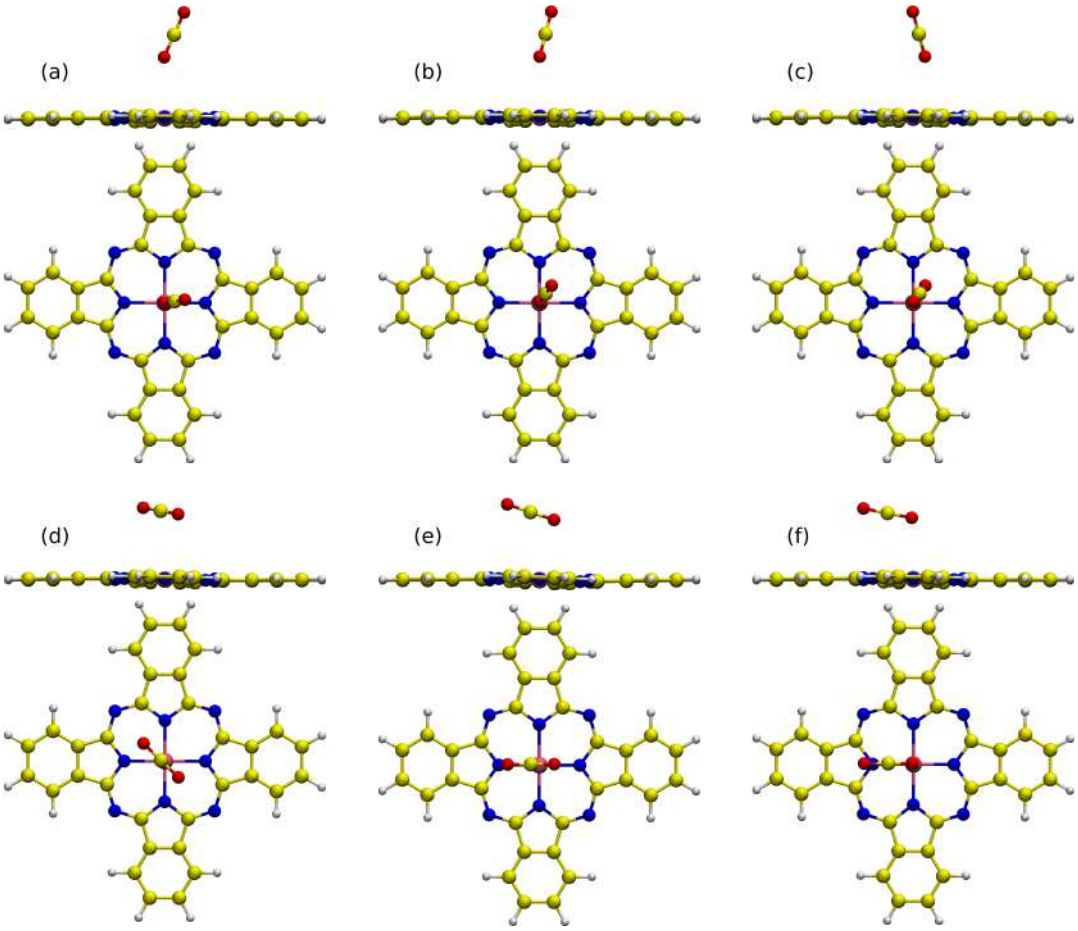

Figure 5.5: The different adsorption (vertical (a,b,c) and horizontal (d,e,f)) configurations of CO_2 on the neutral FePc molecules.

Table 5.3: Calculated structural and electronic parameters of CO_2 adsorbed on neutral FePc (Figure 5.5): adsorption energy (E_{ads}) in eV, distance ($d_{\mathrm{Fe-O}}$) between the Fe and the nearest O of CO_2 , total magnetization(μ_{tot}), absolute magnetization (μ_{abs}), magnetic moment on Fe (μ_{Fe}), C-Ô-C angle of CO_2, and C−O bond length.

System	E_{ads}(eV)	$d_{\mathrm{Fe-O}}$(Å)	$\mu_{tot}(\mu_B)$	$\mu_{abs}(\mu_B)$	$\mu_{\mathrm{Fe}}(\mu_B)$	C-Ô-C	C−O(Å)
a	−0.17	2.91	2.04	2.76	1.99	179.8	1.17
b	−0.17	2.91	2.05	2.75	1.99	179.8	1.17
c	−0.16	2.91	2.05	2.73	1.99	179.9	1.17
d	−0.16	3.12	2.07	2.71	1.99	179.9	1.17
e	−0.14	2.86	2.06	2.46	1.99	179.7	1.17
f	−0.22	2.92	2.04	2.74	1.98	179.8	1.17

charged FePc monolayer are shown in Figure 5.6, with the structural parameters in Table 5.4.

- $+1e^-$ charged system

Adding $+1e^-$ charge to the (CO_2@FePc) system, we have found very weak interaction between the FePc monolayer surface and the adsorbate. During energy

minimization the CO_2 moved away slightly perpendicular to the surface, having a nearly linear configuration (179.3°), as shown in Figure 5.6, a. In this case, no charge transfers were observed between the FePc monolayer, and the C−O bond distance (= 1.17 Å) remained unaffected, as shown in Table 5.4.

- $+2e^-$ charged system

Adding $+2e^-$ charge, we have found that the molecular geometry of the adsorbed CO_2 was significantly different with respect to the isolated CO_2. The C-Ô-C angle decreases to 143.3°, while the C−O bond length increases to 1.22 Å, compared to the gas phase and $+1e^-$ charged system bond lengths of 1.17 Å, indicating that the C−O bond is kind of activated . Furthermore, the bond length between the C atom of CO_2 and the Fe atom (Fe−C) form 2.24 Å. The adsorption energy was calculated using Equation 5.1, where E_{CO_2+FePc} is the total energy of CO_2 onto FePc in the addition of $+2e^-$, E_{FePc} is the total energy of the charged ($+2e^-$) FePc. The isolated CO_2 was always considered neutral. The adsorption energy was found to be 0.28 eV. The stretched C−O bond lengths indicate weaker C−O bonds due to the π-antibonding occupation and activation of the molecule. These results suggest that, as the C atom of CO_2 approaches the Fe atom, the linear structure of isolated CO_2 is deformed to have 'V shape'.

Different number of electrons were added to the system in order to test the activation of CO_2. For $+1e^-$, the CO_2 molecule remains in planar configuration and adsorbed far from the FePc molecule, as in the case of the neutral CO_2. From $+2e^-$ (as we saw) upwards, the CO_2 was activated to have the V-shape. The Fe−C distances decreased and consequently the C-Ô-C angles also decreased. For the addition of $+6e^-$, the Fe−C distance and the C-Ô-C angle were 2.17 Å and 138° respectively. This test was made up to the maximum of $+6e^-$, but the values of $+2e^-$ can be considered a maximum realistic value.

Electronic structure of CO_2 onto FePc monolayer

To get a deeper understanding on the mechanism of CO_2 activation on charged ($+2e^-$) FePc monolayer, we have performed charge density difference analysis calculation. This will give insight about the reorganization of the charge distribution between the CO_2 and FePc monolayer, and was calculated as:

$$\Delta q(\mathbf{r}) = q^{charged}_{CO_2+FePc}(\mathbf{r}) - q^{charged}_{FePc}(\mathbf{r}) - q^{neutral}_{CO_2}(\mathbf{r}), \tag{5.2}$$

where $q^{charged}_{CO_2+FePc}$ is the total charge for the charged system of $CO_2 + FePc$, $q^{charged}_{FePc}$ is the total charge for charged FePc monolayer, and $q^{neutral}_{CO_2}$ is the total charge for the neutral CO_2.
Figure 5.7 shows the charge density difference plot and the planar average of charge density difference plotted between the CO_2 and FePc molecule. Compared to the charge analysis on charged ($+2e^-$) FePc monolayer. Table 5.4 shows the variation of the charges on CO_2 molecule for neutral, charged ($+1e^-$), and charged ($+2e^-$) systems. In the case of $+2e^-$ charged system, We observed clear charge transfer from FePc monolayer to the adsorbed CO_2 molecule. Where a net

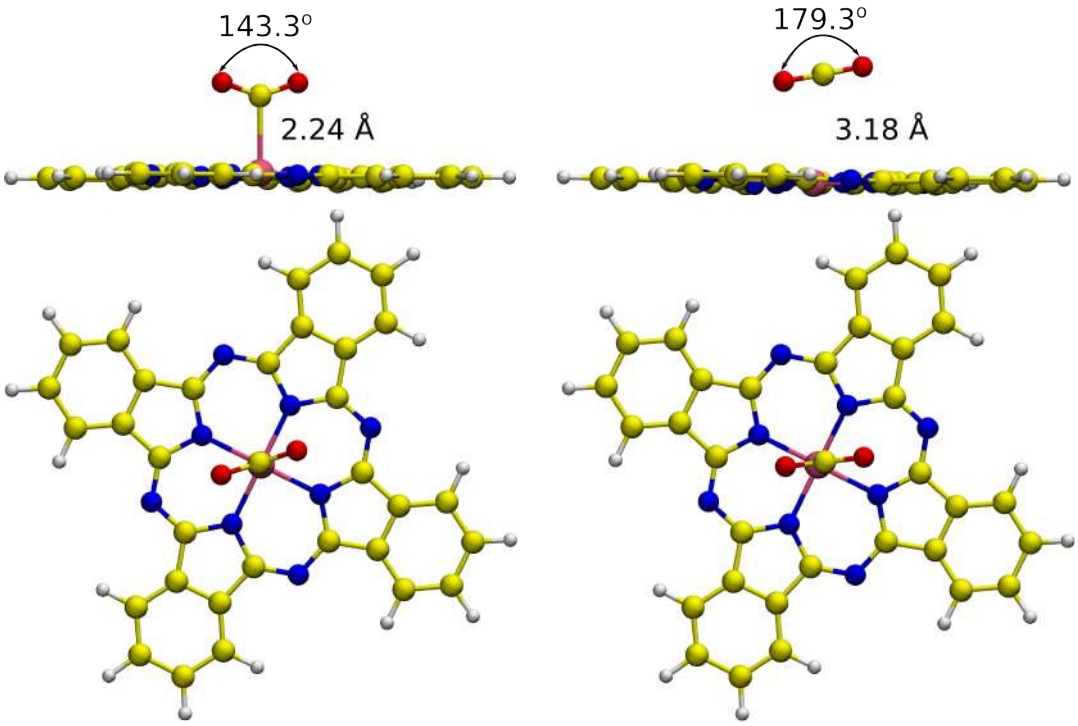

Figure 5.6: Side and top views for the optimized structure of CO_2 adsorbed onto charged FePc monolayer (a)$+1e^-$, and (b)$+2e^-$. Calculated Fe−C distance and C-Ô-C angle for the both structures are shown in (a) and (b).

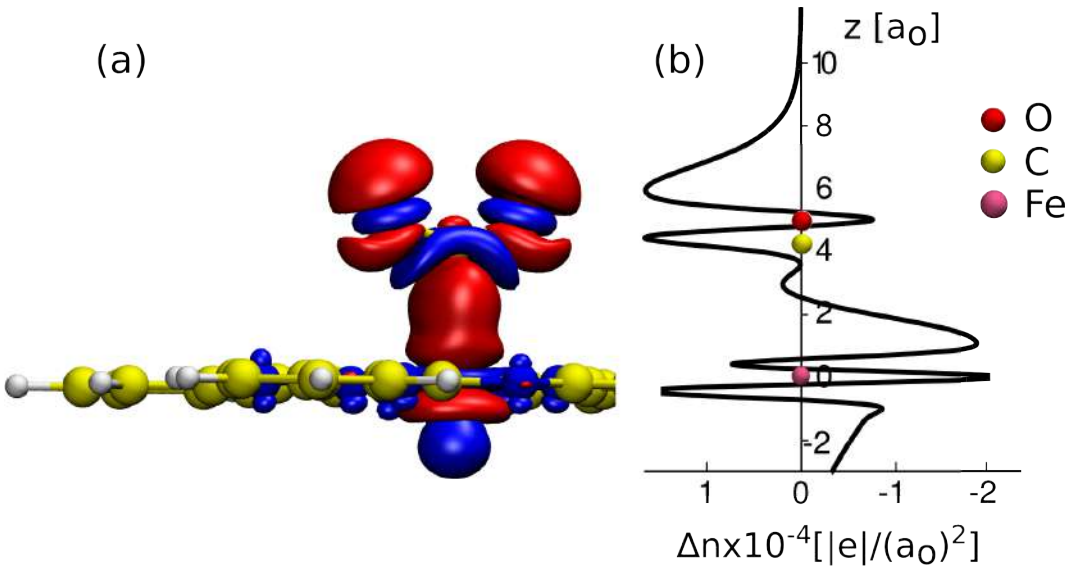

Figure 5.7: (a) The side view of charge density difference plot of CO_2 adsorbed onto FePc monolayer. (b) Planar averaged charge density difference plot along the z-axis. The blue lobes indicates to charge lose, whereas the red lobes indicates a charge gain. The isovalue is set to ± 0.002 $|e|/a_o^3$.

charge of $0.50e^-$ is transfered to CO_2 molecule. The CO_2 adsorption on charged ($\geq +2e^-$) FePc is driven through non negligible charge transfer. Whereas, in the case of neutral, and $+1e^-$ system, almost no charges were added to the CO_2 molecule.

To clarify the source of the negative charge from the FePc monolayer to the CO_2 molecule, we have calculated the electronic DOS, projected on the Fe-d and S-p states of the Fe a, as displayed in Figure 5.8. Figure 5.8 shows comparison of

Table 5.4: Calculated structural and electronic parameters of CO_2 adsorbed on neutral and charged FePc: charge transfered to the C atom (q_C) and to the two O atom (q_{O1} and q_{O2}) of CO_2, angle (C-Ô-C) and bond length (C−O) of the CO_2. The values are reported with respect to the gas phase CO_2.

CO_2@FePc	q_C	q_{O1}	q_{O2}	C-Ô-C (degree)	C−O(Å)
neutral	0.02	0.00	0.00	179.8	1.17
$+1e^-$	0.03	0.00	0.00	179.3	1.17
$+2e^-$	0.23	0.15	0.15	143.3	1.22

PDOS of CO_2 adsorbed on charged ($+2e^-$) and neutral FePc monolayer. There is a hybridization between the Fe d state and the O atoms, indicating strong interaction between CO_2 and charged FePc monolayer. On the contrary, the PDOS of Fe d state of the CO_2 onto neutral FePc monolayer was not modified, similar to the one of Figure (5.4, d) of the isolated neutral FePc. Overall, the above results indicate that the electronic charge transferred to CO_2 from the charged FePc monolayer leads to the activation of CO_2.

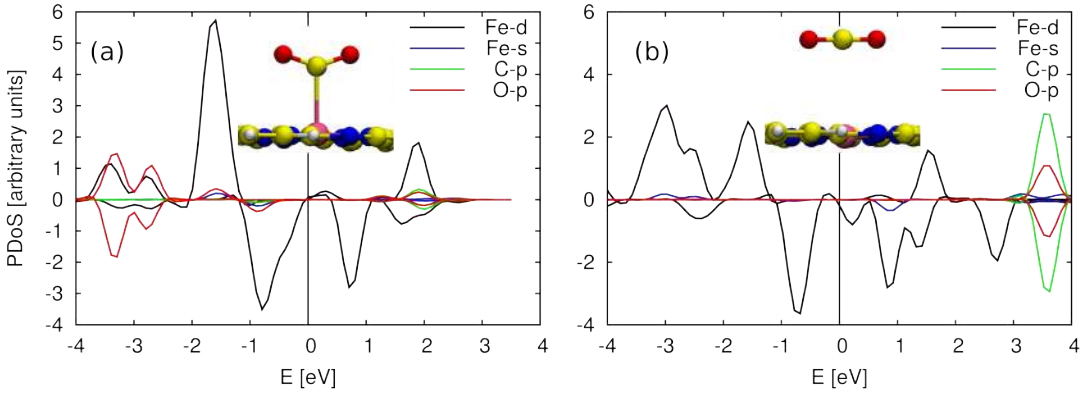

Figure 5.8: Projected Density of State (PDOS) of CO_2 adsorbed on (a) charged, and (b) neutral FePc monolayer. Side view of the adsorbed CO_2 molecule on charged and neutral FePc monolayer is shown in a and b respectively. The Fe s(d) states are shown in blue(black), the (C)O p states of CO_2 are shown in green(red).

5.3.4 Vibrational modes

The vibrational frequencies were calculated for adsorbed CO_2 on neutral and charged ($+1e^-$ and $+2e^-$) FePc monolayers. The calculations were performed allowing to move only the CO_2 molecule and the Fe atom, and without the Hubbard correction. However, since the equilibrium geometry was not affected, we

do not expect important variations of the vibrational frequencies with/without the Hubbard correction.

Table 5.5: Experimental and Simulated frequencies related to the CO_2 symmetric and antisymmetric modes for the negatively charged ($+1e^-$ and $+2e^-$) and neutral CO_2 in the gas phase and + FePc complex.

System	antisymmetric stretching (cm^{-1})	symmetric stretching (cm^{-1})
CO_2/FePc/GRO/Ir(111) (exp)	1729	
literature (gas phase) [131]	2349	1333
CO_2 isolated (neutral)	2336	1297
CO_2/FePc (neutral)	2333	1296
CO_2/FePc ($+1e^-$)	2325	1301
CO_2/FePc ($+2e^-$)	1836	1191

Table 5.5 shows the wavenumbers of the fundamental vibrational modes of the isolated and adsorbed CO_2 molecule on the neutral and charged FePc monolayer, in comparison with experimental results. The calculated symmetric and antisymmetric stretching modes for the Isolated, CO_2 adsorbed onto neutral and ($+1e^-$) charged system lie between $2325cm^{-1} - 2336cm^{-1}$ and $1296cm^{-1} - 1301cm^{-1}$ respectively. The calculated values have similar frequencies to the one of gas phase CO_2 [131], which is in line with the lack of negative electronic transfer from the surface to the adsorbate. The antisymmetric stretching modes of CO_2 on the Fe atom of the charged ($+2e^-$) FePc monolayer shows notable shift with respect to the gas phase CO_2 molecule, which in turn is due to the weakening and stretching of the intra-molecular CO bond. This value ($1729cm^{-1}$) is compared to the experimental value of ($1729cm^{-1}$) of the CO_2^- anion radical [4]. The smaller frequencies of the stretching modes for the chemisorbed CO_2, together with the elongation of the intramolecular C−O bond and localization of negative electronic charge at the O atom give support to the activation of the adsorbate.

5.3.5 Neutral vs charged FePc

In this section we are going to report the effect of negatively (adding electrons) charged FePc molecules on the CO_2 binding. The optimized structure of the FePc monolayer is shown in Figure 5.9. Both neutral and charged FePc monolayer have planar structure. The $Fe-N$ distance for the neutral FePc monolayer is similar to the one of isolated FePc molecule (1.94 Å), and for the charged FePc monolayer this distance is only slightly smaller by 0.01 Å, in agreement with previous theoretical results [130].

Table 5.6 explains the distribution of the additional charge on FePc monolayer. The total magnetization dropped from 2.06 μ_B (2.00 μ_B on Fe atom) to 0.13 μ_B (1.51 μ_B on Fe atom) for neutral to charged ($+2e^-$) FePc monolayer respectively. In the case of neutral FePc the magnetic moment is mainly localized on Fe atom, which is not the case for the charged FePc. When the CO_2 is adsorbed on the $+2e^-$ charged system, the charge on Fe atom was reduced

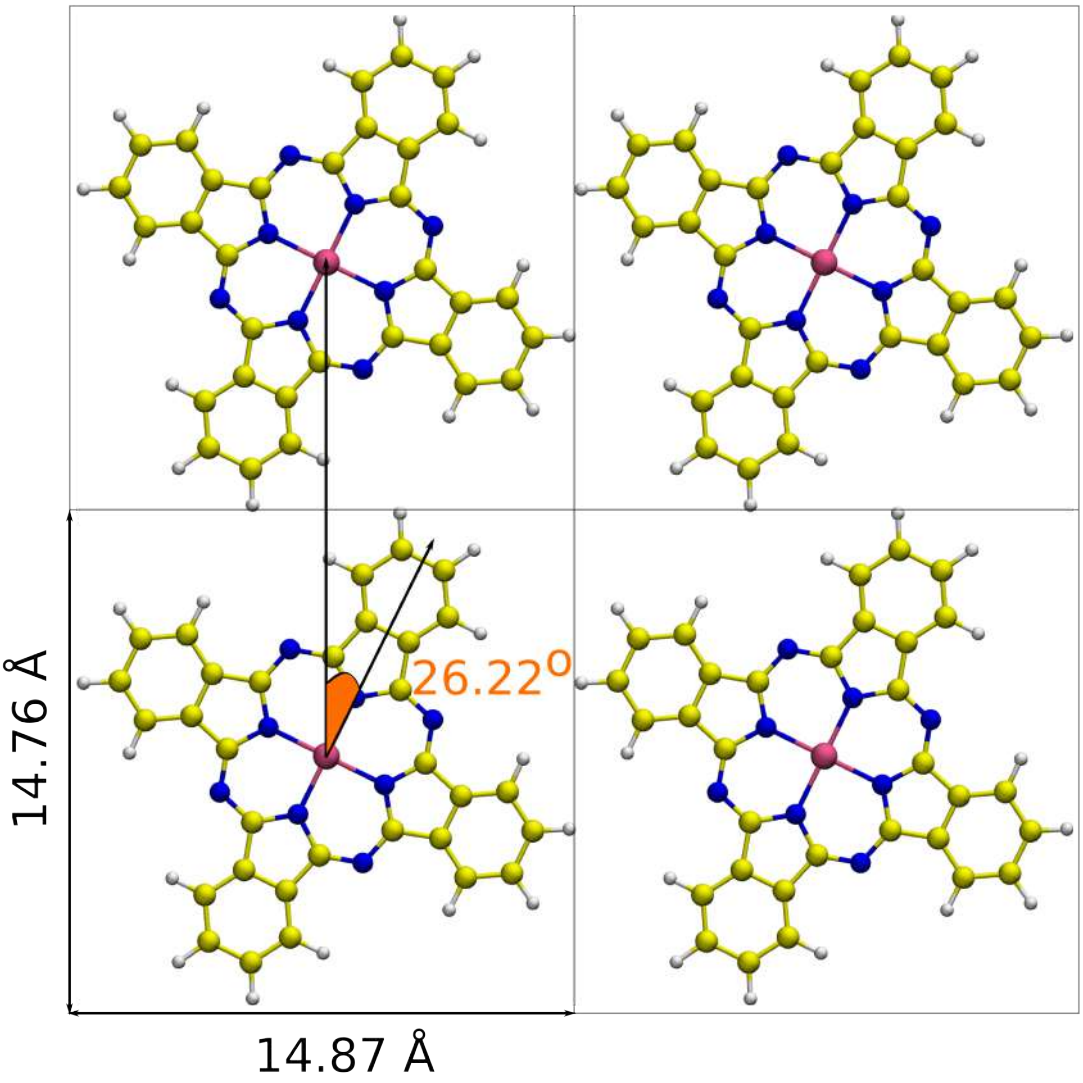

Figure 5.9: Optimized structure of FePc monolayer. Dimension of the cell is shown in solid rows (a=14.87Å, b=14.76Å). FePc molecule is oriented with 26.22°.

Table 5.6: Distribution of the additional charge on the Fe atom (q_{Fe}), C atoms (q_C), N atoms (q_N), and H atoms (q_H) of the FePc monolayer. The difference in charge is calculated with respect to the neural FePc. μ_{Fe} is the magnetic moment on Fe atom, and μ_{tot} is the total magnetization on the FePc system.

FePc monolayer	q_{Fe}	q_C	q_N	q_H	μ_{Fe} (μ_B)	μ_{tot} (μ_B)
neutral	0.00	0.00	0.00	0.00	2.00	2.06
$+1e^-$	0.14	0.75	0.06	0.14	-1.67	-1.06
$+2e^-$	0.35	1.29	0.21	0.27	1.51	-0.13

by $0.08e^-$, whereas the charge on N and C was decreased to $0.17e^-$ and $0.22e^-$ respectively.

To better understand the distribution of the additional charge on the FePc

monolayer, we have performed charge analysis of the neutral and charged ($+2e^-$) FePc molecules to know where the additional charges are localized on the charged FePc molecules. The charge difference was calculated as:

$$\Delta q(\mathbf{r}) = q^{charged}(\mathbf{r})_{FePc} - q^{neutral}_{FePc}(\mathbf{r}), \tag{5.3}$$

where $q^{charged}_{FePc}$ is the total charge for charged FePc molecule, and $q^{neutral}_{FePc}$ is the total charge for neutral FePc molecule.
We can see from Figure 5.10 that the additional of $+2e^-$ charge is distributed all over the system. Specifically, there is addition of $0.26e^-$ on the Fe atom for charged FePc molecule, while the additional charges on the C (N) atoms are $1.29e^-(0.21e^-)$. We can see from this analysis that most of the added electrons are distributed on C atoms, which justifies the decrease in total magnetization to 0.13 μ_B.

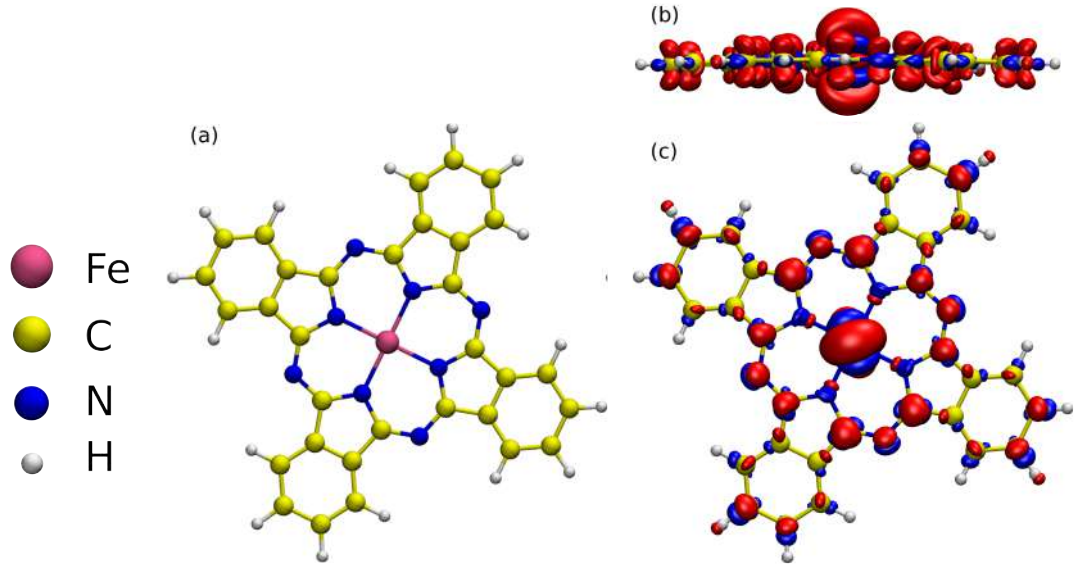

Figure 5.10: (a) Top view for the optimized structure of FePc monolayer. (b,c) side and top views of charge density difference plot between the charged and neutral FePc monolayer respectively. The blue lobes indicate a charge lost, whereas the red lobes indicate a charge gain. The isovalue is set to $\pm$ 0.002 $|e|/a_o^3$

To summarize: We have investigated the effect of negatively charged FePc molecules to the activation of CO_2. The calculations show that the charged (added charge $>$ +1 charge) FePc's molecules are catalytically active for CO_2 capturing more than the neutral (no additional charge) FePc's molecule, consistent with the experimental observation [3]. The CO_2 weakly chemisorbs to the Fe metal center of charged FePc molecules, conversely, CO_2 physisorbs to the neural FePc molecules. In the charged FePc there is effective electron transfer between the FePc and the CO_2 through the interaction between the d and s orbital of Fe atom and the π antibonding orbital of CO_2, such that CO_2 become negatively charged. The formation of covalent bond between CO_2 and Fe was confirmed by analysis of the charge density difference and PDOS, the CO_2 binding to the charged Fe metal center of FePc results in a transfer of charge between Fe and FePc, lead to strong hybridization between CO_2 and Fe,no charge transfer was observed in the case of neutral FePc molecule. Calculations suggest that

in relaxed structures of the CO_2/FePc systems, the initially linear adsorbate molecule bends it is geometry, forming an C-$\hat{O}$-C angle of 143.3°, only when it receives electronic charge from FePc molecule. Furthermore, changes in the simulated vibrational modes of the C−O bond from the isolated to the chemisorbed CO_2 molecule indicate the weekly of this bond. All these results demonstrate that charged FePc is capable for CO_2 activation.
For the future work: The same procedure can be done to test the effect of different metal phthalocyanines on the activation of the CO_2 molecules.

Conclusion and outlook

In this thesis work we have reported an accurate DFT-based investigation on the structure and the properties of some selected representative nanostructured catalysts. Common features of the systems considered were not only the small size of the catalytic centers (aggregates of few atoms, either metallic nanoclusters or organic molecules), but also their structuring in ordered patterns, in order to increase their stability and to limit sintering and deactivation phenomena with the temperature and under the flux of reactants. Such ordering can be obtained through self-assembly, mainly driven by the interaction with an underlying substrate.

On one side, we have considered very small Platinum nanoclusters. Platinum is one of the most efficient catalysts, and the possibility of using nanoclusters is very convenient in terms of size and above all cost. Nanoclusters have a large exposed surface for chemical reactions, and therefore allow the same efficiency of standard catalysts to be obtained with a much smaller amount of material. We studied Platinum nanoclusters ordered in regular arrays obtained using the moirè pattern of graphene on Ir(111) as template. DFT simulations allows the interpretation of experimental results concerning the size and shape distribution of such clusters, their stability and mobility: few-atom nanoclusters are flat (i.e., they show a tendency to wet the substrate), whereas larger nanoclusters are multilayered; few-atom nanoclusters are very mobile, whereas larger nanoclusters stabilize in specific regions of the moirè pattern. We studied the interaction of such nanoclusters with carbon monoxide. We find that both terminally and bridge bonded CO species populate nonequivalent sites of the clusters, spanning from first to second-layer terraces (in larger clusters) to borders and edges. A progressively lower Pt-Pt coordination is observed upon CO adsorption for increasing coverage, accompanied by a significant restructuring of the clusters: therefore, although the moirè template tends to keep an ordered nanoclusters pattern, CO adsorption seems to promote particle sintering for small clusters and reshaping for large ones. In conclusion, our DFT investigation, combined with a series of experiments and characterization with different spectroscopy and microscopy techniques, indicate that further investigation is needed to design more efficient Platinum-based nanostructured catalysts and overcome the problem of their restructuring under the flux of reactants. The results have been published in Ref. [1].

On the other side, we have investigated nanocatalysts constituted by organic

molecules, inspired by Nature. In particular, we have considered Iron phthalocyanines (FePc). Two kinds of templates have been considered: $Al_2O_3/Ni_3Al(111)$ substrate, and the moirè pattern of graphene/Ir(111).

A high-density nanostructured catalyst is obtained by depositing FePc molecules on $Al_2O_3/Ni_3Al(111)$ substrate, resulting in a commensurate molecular superstructure with the same periodicity of the substrate. The superstructure is characterized by a hexagonal arrangements of "missing" FePc (corresponding to the "holes", i.e., oxygen vacancies, in the substrate), where every "hole" is surrounded by a hexagonal ring of FePc molecules. The adsorption energy of an individual FePc molecule varies by more than 2 eV on different sites of the substrate, being in particular very weak in correspondence to its oxygen vacancies. This explains the absence of a FePc on the "hole" site in the self-assembled layered structure. The overall structure is a regular patterns of Fe ions embedded in the self-assembled FePc layer. However, experiments indicate that a perfect long-range order is never achieved, and the growth of multilayers of alternated chirality starts before the first layer is completed. DFT calculations give a rationale about that, in terms of layer-layer interaction and hence of energetics.

Cu deposition on $Al_2O_3/Ni_3Al(111)$ substrate flattens the surface potential and allows the molecules to fully cover the substrate. A long-range order is adopted with an almost square structure, which is also typical of FePc assemblies on other substrates. Calculations suggest that Cu atoms, filling the "holes", allow adsorption of the FePc's also at the oxygen vacancies. Furthermore, this action is better performed by Cu nanoclusters with small size (less or equal to about 6 atoms). The DFT optimized superstructures perfectly match the experimental observations. Remarkably, we conclude that by Cu surface treatment we can tune the formation of different self-assembled layered FePc structures.

Finally, in the highly compact, square structure, a few molecules exhibit a completely different bias-dependence appearance with respect to the majority of the FePc. We proposed different models for these "strange" molecules, and, on the basis of the comparison between simulated and experimental STM images and other DFT results, we exclude that such molecules are CuPc, and we ascribe their different bias-dependence appearance to demetalation.

A 2D crystal of FePc can also be supported by graphene/Ir(111). Whereas neutral FePc's are inert with respect to CO_2 capturing, DFT calculations, combined with experiments, have demonstrated that negatively charged FePc molecules can capture and activate CO_2 through the Fe center. The stabilization of the CO_2-Fe chemical bond is obtained experimentally by governing the charge transfer across the graphene-metallorganic layer interface upon oxidation of graphene. We simulated the effect of graphene oxidation on the 2D FePc layer by adding a negative charge on the molecules. Carbon dioxide chemisorbs in an activated ("V"-shape) configuration, thus lowering the barrier for further reaction. DFT shows that both adsorption and activation are due to charge transfer and in particular exploits a molecular trans-effect, since the FePc's, in turn, transfer electrons to the CO_2. In this way, we are able to turn a weakly binding site

into a strong one in an artificial structure that mimics many features of complex biological systems.

The results on FePc have been reported in three papers, one already published [3], one under review [4], and a third one in preparation [2].

In conclusion, this thesis work has given the opportunity of deeply learning the DFT method and its application to nanostructures. Several issues concerning some peculiar properties and the self-assembling of few representative systems have been afforded and understood. Still, the fascinating question of the balance between the molecule-molecule (or cluster-cluster) lateral interaction and the molecule (or cluster)-substrate interaction, that is on the basis of ordered structure formation, remains open.

The continuous interaction with the experimental colleagues constituted an extremely positive experience of how the synergy between experimental, theoretical, computational efforts can be successful in understanding some aspects of chemical/physical processes and systems in Nature: an appealing, marvellous, neverending adventure.

Acknowledgements to:

- The PhD fellowship has been offered by *ICTP* in the framework of the cooperation with the University of Trieste.
- This first part of the research concerning nanoclusters was supported by the Italian Ministry of Foreign Affairs and International Cooperation (MAECI), MIUR, and the University of Trieste under the program *Finanziamento di Ateneo per progetti di ricerca scientifica -FRA2015* (P.I.: M. Peressi).
- The study about the self-assemblies of metal phthalocyanines was supported by the University of Trieste through the program *Finanziamento di Ateneo per progetti di ricerca scientifica −FRA 2016* (P.I.: E. Vesselli).
- Computational high performance computing resources have been obtained from *CINECA* through the ISCRA initiative and the agreement with the University of Trieste.

Bibliography

[1] N. Podda, M. Corva, F. Mohamed, Z. Feng, C. Dri, F. Dvorák, V. Matolin, G. Comelli, M. Peressi, and E. Vesselli. *Experimental and Theoretical Investigation of the Restructuring Process Induced by CO at Near Ambient Pressure: Pt Nanoclusters on Graphene/Ir(111).* ACS Nano 2017, **11**, 1041−1053.

[2] F. Mohamed, M. Corva, E. Tomsic, Z. Feng, T. Skala, G. Comelli, N. Seriani, M. Peressi, E. Vesselli. *A self-assembled lattice of single metal atom catalysts on an ultra-thin alumina film: structure of a 2D crystal of Iron Phthalocyanines*, in preparation.

[3] M. Corva, F. Mohamed, E. Tomsic, Z. Feng, T. Skala, G. Comelli, N. Seriani, M. Peressi, E. Vesselli. *Substrate- to Laterally-Driven Self-Assembly Steered by Cu Nanoclusters: The Case of FePcs on an Ultrathin Alumina Film.* ACS Nano 2018, **12**, 10755−10763.

[4] M. Corva, F. Mohamed, E. Tomsic, M. Rinaldi, C. Cepek, N. Seriani, M. Peressi, E. Vesselli. *Learning from Nature: Charge Transfer and Carbon Dioxide Activation at Single, Biomimetic Fe Sites in Tetrapyrroles on Graphene*, accepted.

[5] P. Kunwar, J. Hassinen, G. Bautista, R. H. A. Ras, J. Toivonen. *Sub-micron scale patterning of fluorescent silver nanoclusters using low-power laser.* Sci. Rep. 2016, **6**, 23998.

[6] S. Vajda, M. J. Pellin, J. P. Greeley, C. L. Marshall, L. A. Curtiss, G. A. Ballentine, J. W. Elam, S. Catillon-Mucherie, P. C. Redfern, F. Mehmood, P. Zapol. *Subnanometre platinum clusters as highly active and selective catalysts for the oxidative dehydrogenation of propane.* Nat. Mater. 2009, **8**, 213−216.

[7] M. Valden. *Onset of Catalytic Activity of Gold Clusters on Titania with the Appearance of Nonmetallic Properties.* Science 1998, **281**, 1647−1650.

[8] T. Ioannides, X. Verykios. *Influence of the Carrier on the Interaction of H2 and CO with Supported Rh.* J. Catal. 1993, **140**, 353−369.

[9] J. A. Olmos-Asar, E. Vesselli,A. Baldereschi, and M. Peressi. *Self-seeded nucleation of Cu nanoclusters on Al2O3/Ni3Al(111): an ab initio investigation.* Phys. Chem. Chem. Phys. 2014, **16**, 23134−23142.

[10] M. Schmid, G. Kresse, A. Buchsbaum, E. Napetschnig, S. Gritschneder, M. Reichling and P. Varga. *Nanotemplate with Holes: Ultrathin Alumina on $Ni_3Al(111)$.* Phys. Rev. Lett. 2007, **99**, 196104.

[11] S. Gritschneder, C. Becker, K. Wandelt, and M. Reichling. *Disorder or Complexity? Understanding a Nanoscale Template Structure on Alumina*. J. Am. Chem. Soc. 2007, **129**, 4925−4928.

[12] R. P. Feynman. *Force in Molecules*. Phys. Rev. 1939, **56**, 840−843.

[13] P. Hohenberg and W. Kohn. *Inhomogeneous Electron Gas*. Phys. Rev. B 1964, **136**, B864−B871.

[14] W. Kohn and L. J. Sham. *Self-consistent Equations including Exchange and correlation Effects*. Phys. Rev B 1965, **140** A1133−A1138.

[15] D. M. Ceperley, B. J. Alder. *Ground State of the Electron Gas by a Stochastic Method*. Phys. Rev. Lett. 1980, **45**, 566−569.

[16] J. P. Perdew, K. Burke, M. Ernzerhof. *Generalized Gradient Approximation Made Simple*. Phys. Rev. Lett. 1996, **77**, 3865−3868.

[17] M. Cococcioni, and S. de Gironcoli *Linear response approach to the calculation of the effective interaction parameters in the LDA+U method*. Phys. Rev. B 2005, **71**, 035105.

[18] V. I. Anisimov, J. Zaanen, O. K. Andersen, *Band theory and Mott insulators: Hubbard U instead of Stoner I*. Phys. Rev. B 1991, **44**, 943.

[19] V. I. Anisimov, F. Aryasetiawan, and A. I. Lichtenstein. *First-principles calculations of the electronic structure and spectra of strongly correlated systems: the LDA + U method*. J. Phys.: Condens. Matter, 1997, **9**, 767−808.

[20] R. M. Martin. *Electronic Structure Basic Theory and Practical Method*. Cambridge University press 2012.

[21] P. Giannozzi, S. Baroni, N. Bonini, M. Calandra, R. Car, C. Cavazzoni, D. Ceresoli, G. L. Chiarotti, M. Cococcioni, I. Dabo, A. Dal Corso, S. Fabris, G. Fratesi, S. de Gironcoli, R. Gebauer, U. Gerstmann, C. Gougoussis, A. Kokalj, M. Lazzeri, L. Martin-Samos, N. Marzari, F. Mauri, R. Mazzarello, S. Paolini, A. Pasquarello, L. Paulatto, C. Sbraccia, S. Scandolo, G. Sclauzero, A. P. Seitsonen, A. Smogunov, P. Umari and R. M. Wentzcovitch. *QUANTUM ESPRESSO: a Modular and Open-Source Software Project for Quantum Simulations of Materials*. J. Phys. Condens. 2009, Matter **21**, 395502.

[22] D. H. Hamalm, M. Schluter and C. Chiange. *Norm-conserving Pseudopotentials*. Phys. Rev b 1979, **43**, 1494−1497.

[23] D. Vanderbilt. *Soft Self-Consistent Pseudopotentials in a Generalized eigenvalue Formalism*. Phys. Rev b 1990, **41**,7892−7895.

[24] K. Laasonen, A. Pasquarello, R. Car, C. Lee, D. Vanderbilt. *Car-Parrinello molecular dynamics with Vanderbilt ultrasoft Pseudopotentials*, Phys. Rev B 1993, **47**, 10142−10153.

[25] A. Baldereschi. *Mean-Value Point in the Brillouin Zone*, Phys. Rev. B 1973, **7**, 5212−5215.

[26] D. L. Chadi and L. Cohen. *Special Points in the Brillouin Zone*, Phys. Rev. B 1973, **8** 5747−5753.

[27] H. J. Monkhorst and J. D. Pack *Special points for Brillouin-zone integrations*. Phys. Rev. B 1976, **13**, 5188.

[28] J. Tersoff and D. R. Hamann *Theory of the Scanning Tunneling Microscope*. Phys. Rev. B 1985, **31**, 805−813.

[29] M. Corva, A. Ferrari, M. Rinaldi, Z. Feng, M. Roiaz, C. Rameshan, G. Rupprechter, R. Costantini, M. Dell'Angela, G. Pastore, G. Comelli, N. Seriani, and E. Vesselli. *Vibrational fingerprint of localized excitons in a two-dimensional metal-organic crystal*. Nat. Commun. 2018, **9**, 4703.

[30] B. Brena, C. Puglia, M. de Simone, M. Coreno, K. Tarafder, V. Feyer, R. Banerjee, E. Göthelid, B. Sanyal, P. M. Oppeneer, O. Eriksson. *Valence-band electronic structure of iron phthalocyanine: an experimental and theoretical photoelectron spectroscopy study*. J. Chem. Phys. 2011, **134**, 074312.

[31] C. Kittel. *Introduction to Solid State Theory*. Wiley, New York 2005, 8th edition.

[32] P. Giannozzi, S. de Gironcoli, P. Pavone, and S. Baroni. *Ab initio calculation of phonon dispersions in semiconductors*. Phys. Rev. B 1991, **43**, 7231.

[33] X. Gonze, D. C. Allan, and M. P. Teter. *Dielectric tensor, effective charges, and phonons in α-quartz by variational density-functional perturbation theory*. Phys. Rev. Lett. 1992, **68**, 3603.

[34] H. -J. Freund. *Model Systems in Heterogeneous Catalysis: Selectivity Studies at the Atomic Level*. Top Catal. 2008, **48**, 137−144.

[35] I. E. L. Stephens, J. S. Elias, Y. Shao-Horn. *The Importance of Being Together*. Science 2015, **350**, 164−165.

[36] K. Ding, A. Gulec, A. M. Johnson, N. M. Schweitzer, G. D. Stucky, L. D. Marks, P. C. Stair. *Identification of Active Sites in CO Oxidation and Water-Gas Shift over Supported Pt Catalysts*. Science 2015, **350**, 189−192.

[37] C. R. Henry. *2D-Arrays of Nanoparticles as Model Catalysts*. Catal. Lett. 2015, **145**, 731−749.

[38] A. T. NDiaye, T. Gerber, C. Busse, J. Myslivecek, J. Coraux, T. Michely. *A Versatile Fabrication Method for Cluster Superlattices*. New J. Phys. 2009, **11**, 103045.

[39] S. Linas, F. Jean, T. Zhou, C. Albin, G. Renaud, L. Bardotti, F. Tournus. *Moiré Induced Organization of Size-Selected Pt Clusters Soft Landed on Epitaxial Graphene*. Sci. Rep. 2015, **5**, 13053.

[40] J. Knudsen, P. J. Feibelman, T. Gerber, E. Grånäs, K. Schulte, P. Stratmann, J. N. Andersen, T. Michely. *Clusters Binding to the Graphene Moiré on Ir(111): X-Ray Photoemission Compared to Density Functional Calculations*. Phys. Rev. B: Condens. Matter Mater. Phys. 2012, **85**, 35407.

[41] P. J. Feibelman. *Pinning of graphene to Ir(111) by flat Ir dots*. Phys. Rev. B 2008, **77**, 165419.

[42] T. Gerber, J. Knudsen, P. J. Feibelman, E. Grånäs, P. Stratmann, K. Schulte, J. N. Andersen, T. Michely. *CO-Induced Smoluchowski Ripening of Pt Cluster Arrays on the Graphene/Ir(111) Moiré* . ACS Nano 2013, **7**, 2020−2031.

[43] , D. Franz, N. Blanc, J. Coraux, G. Renaud, S. Runte, T. Gerber, C. Busse, T. Michely, P. J. Feibelman, U. Hejral, and A. Stierle. *Atomic Structure of Pt Nanoclusters Supported by graphene/Ir(111) and Reversible Transformation under CO Exposure*. Phys. Rev. B: Condens. Matter Mater. Phys. 2016, **93**, 45426.

[44] K. Gotterbarm, ; F. Späth, U. Bauer, C. Bronnbauer, H.-P. Steinrück, C. Papp. *Reactivity of Graphene-Supported Pt Nanocluster Arrays*. ACS Catal. 2015, **5**, 2397−2403.

[45] K. C. Chou, S. Westerberg, Y. R. Shen, P. N. Ross, G. A. Somorjai. *Probing the Charge-Transfer State of CO on Pt(111) by Two-Dimensional Infrared-Visible Sum Frequency Generation Spectroscopy*. Phys. Rev. B: Condens. Matter Mater. Phys. 2004, **69**, 153413.

[46] H. Aizawa, S. Tsuneyuki. *First-Principles Study of CO Bonding to Pt(111): Validity of the Blyholder Model*. Surf. Sci. 1998, **399**, L364−L370.

[47] X. Su, P. S. Cremer, Y. R. Shen, G. A. Somorjai. *High-Pressure CO Oxidation on Pt(111) Monitored with Infrared− Visible Sum Frequency Generation (SFG)*. J. Am. Chem. Soc. 1997, **119**, 3994−4000.

[48] B. Hayden, A. Bradshaw. *The Adsorption of CO on Pt (111) Studied by Infrared-Reflection-Adsorption Spectroscopy*. J. Electron Spectrosc. Relat. Phenom. 1983, **30**, 51.

[49] B. E. Hayden, K. Kretzschmar, A. M. Bradshaw, R. G. Greenler. *An Infrared Study of the Adsorption of CO on a Stepped Platinum Surface*. Surf. Sci. 1985, **149**, 394−406.

[50] C. Klünker, M. Balden, S. Lehwald, W. Daum. *CO Stretching Vibrations on Pt(111) and Pt(110) Studied by Sumfrequency Generation*. Surf. Sci. 1996, **360**, 104−111.

[51] K. McCrea, J. S. Parker, P. Chen, G. Somorjai. *Surface Structure Sensitivity of High-Pressure CO Dissociation on Pt(557), Pt(100) and Pt(111) Using Sum Frequency Generation Surface Vibrational Spectroscopy*. Surf. Sci. 2001, **494**, 238−250.

[52] M. J. Kappers, J. H. van der Maas. *Correlation between CO Frequency and Pt Coordination Number. A DRIFT Study on Supported Pt Catalysts*. Catal. Lett. 1991, **10**, 365−373.

[53] A. Crossley, D. A. King. *Infrared Spectra for Co Isotopes Chemisorbed on Pt(111): Evidence for Strong Absorbate Coupling Interactions*. Surf. Sci. 1977, **68**, 528−538.

[54] E. Schweizer, B. N. J. Persson, M. Tü shaus, D. Hoge, A. M. Bradshaw. *The Potential Energy Surface, Vibrational Phase Relaxation and the Order-Disorder Transition in the Adsorption System Pt111-CO*. Surf. Sci. 1989, **213**, 49−89.

[55] E. H. G. Backus. *Real-Time Observation of Molecular Motion on a Surface*. Science 2005, **310**, 1790−1793.

[56] M. Corva, Z. Feng, C. Dri, F. Salvador, P. Bertoch, G. Comelli, E. Vesselli. *Carbon Dioxide Reduction on Ir(111): Stable Hydrocarbon Surface Species at near-Ambient Pressure*. Phys. Chem. Chem. Phys. 2016, **18**, 6763−6772.

[57] E. Grånäs, M. Andersen, M. A. Arman, T. Gerber, B. Hammer, J. Schnadt, J. N. Andersen, T. Michely, J. Knudsen. *CO Intercalation of Graphene on Ir(111) in the Millibar Regime*. J. Phys. Chem. C 2013, **117**, 16438−16447.

[58] S. Grimme. *Semiempirical GGA-Type Density Functional Constructed with a Long-Range Dispersion Correction*. J. Comput. Chem. 2006, **27**, 1787-1799.

[59] J. Andersen, D. Hennig, E. Lundgren, M. Methfessel, R. Nyholm, M. Scheffler. *Surface Core-Level Shifts of Some 4d-Metal Single-Crystal Surfaces: Experiments and Ab Initio Calculations*. Phys. Rev. B: Condens. Matter Mater. Phys. 1994, **50** , 17525-17533.

[60] A. T. NDìaye, S. Bleikamp, P. J. Feibelman, T. Michely. *Two-Dimensional Ir Cluster Lattice on a Graphene Moiré on Ir(111)*. Phys. Rev. Lett. 2006, **97**, 215501.

[61] A. T. NDìaye, J. Coraux, T. N. Plasa,C. Busse, T. Michely. *Structure of Epitaxial Graphene on Ir(111)*. New J. Phys. 2008, **10**, 043033.

[62] F. Mohamed, M. Pividori, M. Peressi. *Transition metals nanoparticles supported on graphene: insight from ab-initio simulations*. Master Thesis 2016.

[63] D. De-en. Jiang, Z. Chen. *Graphene Chemistry: Theoretical Perspectives*. John Wiley and Sons, Ltd 2013, 8th edition.

[64] S. Bromley S. Woodley. *Computational Modelling of Nanoparticles*. Elsevier 2018.

[65] K. Okazaki-Maedaa, Y.Morikawab, S.Tanakac, M.Kohyamac. *Structures of Pt clusters on graphene by first-principles calculations*. Surf. Sci. 2010, textbf604, 144−154.

[66] M. Kiskinova, A. Szabo, and J. T. Yates. *Compressed CO overlayers on Pt (111)−evidence for tilted CO species at high coverages by digital ESDIAD.* Jr., Surf. Sci. 1988, **205**, 215−229.

[67] J. A. Steckel, A. Eichler, and J. Hafner. *CO adsorption on the CO-precovered Pt(111) surface characterized by density-functional theory.* Phys. Rev. B 2003 **68**, 085416.

[68] J. B. A. Davis, F. Baletto, R. L. Johnston. *The Effect of Dispersion Correction on the Adsorption of CO on Metallic Nanoparticles.* J. Phys. Chem. A 2015, **119**, 9703−9709.

[69] M. C. Figueiredo, M. Melander, J. Solla-Gullón, T. Kallio, K. Laasonen. *Bismuth and CO Coadsorption on Platinum Nanoparticles.* J. Phys. Chem. C 2014, **118**, 23100−23110.

[70] B. Shan, Y. Zhao, J. Hyun, N. Kapur, J. B. Nicholas, and K. Cho. *Coverage-Dependent CO Adsorption Energy from First-Principles Calculations.* J. Phys. Chem. C 2009, **113**, 6088−6092.

[71] F. N. Ribeiro and S. Fabris *Role of cluster morphology in the dynamics and reactivity of sub-nm Pt clusters supported on ceria surfaces* J. Phys. Chem. C 2014, **118**, 21014.

[72] B. Eren, D. Zherebetskyy, L. L. Patera, C. H. Wu, H. Bluhm, C. Africh, L.-W. Wang, G. A. Somorjai, M. Salmeron. *Activation of Cu(111) Surface by Decomposition into Nanoclusters Driven by CO Adsorption.* Science 2016, **351**, 475−478.

[73] J. A. Olmos-Asar, E. Vesselli,A. Baldereschi, and M. Peressi. *Towards optimal seeding for the synthesis of ordered nanoparticle arrays on alumina/Ni3Al(111)* . Phys. Chem. Chem. Phys. 2015, **17**, 28154−28161.

[74] A. Lehnert, A. Krupski, S. Degen, K. Franke, R. Decker, S. Rusponi, M. Kralj, C. Becker, H. Brune, K. Wandelt. *Nucleation of ordered Fe islands on Al 2 O 3 /Ni 3 Al(111).* Surface Science, 2006, **600**, 1804-1808.

[75] M. Moors, A. Krupski, S. Degen, M. Kralj, C. Becker, K. Wandelt. *Scanning tunneling microscopy and spectroscopy investigations of copper phthalocyanine adsorbed on Al2O3/Ni3Al(111).* Applied Surface Science 2008, **254**, 4251−4257.

[76] A. B. P. Lever. *Advances in Inorganic Chemistry and Radiochemistry.* Adv. Inorg. Chem. Radiochem 1965, **7**, 27.

[77] M. K. Engel. *Single-Crystal and Solid-State Molecular Structures of Phthalocyanine Complexes.* Report Kawamura Inst. Chem. Res. 1997, **8**, 11.

[78] J. M. Berg, J. L. Tymoczko, L. Stryer. *Biochemistry, 5th edition.* New York, NY, U. S. A: W. H. Freeman and company 2002.

[79] Xiao-Feng Yang , Aiqin Wang , Botao Qiao , Jun Li , Jingyue Liu , and Tao Zhang. *Single-Atom Catalysts: A New Frontier in Heterogeneous Catalysis.* Acc. Chem. Res. 2013, **46**, 1740−1748.

[80] X. F. Chen, J. M. Yan, Q. Jiang. *Single Layer of Polymeric Metal-Phthalocyanine: Promising Substrate to Realize Single Pt Atom Catalyst with Uniform Distribution.* Phys. Chem. C 2014 **118**, 2122−2128.

[81] A. B. Sorokin. *Phthalocyanine Metal Complexes in Catalysis.* Chem. Rev. 2013, **113**, 8152−8191.

[82] J. Blochwitz, M. Pfeiffer, T. Fritz, K. leo. *Low voltage organic light emitting diodes featuring doped phthalocyanine as hole transport material.* Appl. Phys. Lett. 1998, **73**, 729−731.

[83] G. Bottari, G. de la Torre, D.M. Guldi, T. Torres. *Covalent and Noncovalent Phthalocyanine-Carbon Nanostructure Systems: Synthesis, Photoinduced Electron Transfer, and Application to Molecular Photovoltaics.* Chem. Rev. 2010, **110**, 6768−6816.

[84] W.R. Cao, J.G. Xue. *Recent progress in organic photovoltaics: device architecture and optical design. Energy Environ.* Energy Environ. Sci. 2014, **7**, 2123−2144.

[85] A.W. Hains, Z.Q. Liang, M.A. Woodhouse, B.A. Gregg. *Molecular semiconductors in organic photovoltaic cells.* Chem. Rev. 2010, **110**, 6689−6735.

[86] M. Ince, J.H. Yum, Y. Kim, S. Mathew, M. Grätzel, T. Torres, M. K. Nazeeruddin. *Molecular Engineering of Phthalocyanine Sensitizers for Dye-Sensitized Solar Cells.* J. Phys. Chem. C 2014, **118**, 17166−17170.

[87] C.D. Dimitrakopoulos, P.R.L. Malenfant. *Organic Thin Film Transistors for Large Area Electronics.* Adv. Mater. 2002, **14**, 99−117.

[88] M. Bevilacqua, J. Filippi, A. Lavacchi, A. Marchionni, H. A. Miller, W. Oberhauser, E. Vesselli, and F. Vizza. *Energy Savings in the Conversion of CO_2 to Fuels using an Electrolytic Device.* Energy Technol. 2014, **2**, 522−525.

[89] R. Burkitt, T.R. Whiffen, E. H. Yu. *Iron phthalocyanine and MnOx composite catalysts for microbial fuel cell applications.* Applied Catalysis B: Environmental 2016, **181** 279−288.

[90] Z. H. Cheng, L. Gao, Z. T. Deng, N. Jiang, Q. Liu, D. X. Shi, S. X. Du, H. M. Guo, H.-J. Gao. *Epitaxial Growth of Iron Phthalocyanine at the Initial Stage on Au(111) Surface.* J. Phys. Chem. C 2007, **111**, 2656−2660.

[91] M. Casarin, M. Di Marino, D. Forrer, M. Sambi, F. Sedona, E. Tondello, A. Vittadini, V. Barone, and M. Pavone. *Coverage-Dependent Architectures of Iron Phthalocyanine on Ag(110): a Comprehensive STM/DFT Study.* J. Phys. Chem. C, 2010 **114**, 2144-2153.

[92] F. Petraki, H. Peisert, U. Aygül, F. Latteyer, J. Uihlein, A. Vollmer, and T. Chasse. *Electronic Structure of FePc and Interface Properties on Ag(111) and Au(100).* J. Phys. Chem. C 2012, **116**, 11110−11116.

[93] Y. Y. Zhang, S. X. Du, and H.-J. Gao. *Binding configuration, electronic structure, and magnetic properties of metal phthalocyanines on a Au(111) surface studied with ab initio calculations.* Phys. Rev. B 2011, **84**, 125446.

[94] T. G. Gopakumar, T. Brumme, J. Kröger, C. Toher, G. Cuniberti, and R. Berndt. *Coverage-Driven Electronic Decoupling of Fe-Phthalocyanine from a Ag(111) Substrate.* J. Phys. Chem. C 2011, **115**, 12173−12179.

[95] P. Gargiani, M. Angelucci, C. Mariani, and M. G. Betti. *Metal-phthalocyanine chains on the Au(110) surface: Interaction states versus d-metal states occupancy.* Phys. Rev. B 2010, **81**, 085412.

[96] K. Manandhar, K.T. Park, S. Ma, J. Hrbek. *Heteroepitaxial thin film of iron phthalocyanine on Ag(111).* Surface Science 2009, **603**, 636−640.

[97] Z. Hu, B. Li, A. Zhao, J. Yang and J. G. Hou. *Electronic and Magnetic Properties of Metal Phthalocyanines on Au(111) Surface: A First-Principles Study.* J. Phys. Chem. C 2008, **112**, 13650−13655.

[98] A. Mugarza, R. Robles, C. Krull, R. Korytár, N. Lorente, and P. Gambardella. *Electronic and magnetic properties of molecule-metal interfaces: Transition-metal phthalocyanines adsorbed on Ag(100).* Phys. Rev. B 2012, **85**, 155437.

[99] Y. H. Jiang, W. D. Xiao, L. W. Liu, L. Z. Zhang, J. C. Lian, K. Yang, S. X. Du, and H.-J. Gao. *Self-Assembly of Metal Phthalocyanines on Pb(111) and Au(111) Surfaces at Submonolayer Coverage.* J. Phys. Chem. C 2011, **115**, 44, 21750−21754.

[100] . Xing Lu, and K. W. Hipps *Scanning Tunneling Microscopy of Metal Phthalocyanines: d6 and d8 Cases.* J. Phys. Chem. B 1997, **101**, 5391−5396.

[101] Y. Bai, F. Buchner, M. T. Wendahl, I. Kellner, A. Bayer, H-P. Steinrck,H. Marbach, and J. M. Gottfried. *Direct Metalation of a Phthalocyanine Monolayer on Ag(111) with Coadsorbed Iron Atoms.* J. Phys. Chem. C 2008 **112**, 6087−6092.

[102] P. S. Deimel, R. M. Bababrik, B. Wang, P. J. Blowey, L. A. Rochford, P. K. Thakur, T-L Lee, M-L Bocquet, J. V. Barth, P. Woodruff, D. A. Duncan, and F. Allegretti. *Direct quantitative identification of the "surface trans-effect".* Chem. Sci. 2016, **7**, 5647−5656.

[103] W. Hieringer, K. Flechtner, A. Kretschmann, K. Seufert, W. Auwärter, J. V. Barth, A. Görling, H. Steinrück, and J. M. Gottfried. *The Surface Trans Effect: Influence of Axial Ligands on the Surface Chemical Bonds of Adsorbed Metalloporphyrins.* J. Am. Chem. Soc. 2011, **133**, 6206−6222.

[104] M. Gottfried, and H. Marbach. *Surface-Confined Coordination Chemistry with Porphyrins and Phthalocyanines: Aspects of Formation, Electronic Structure, and Reactivity.* Zeitschrift für Phys. Chemie 2009, **223**, 53−74.

[105] C. Isvoranu, B. Wang, E. Ataman, J. Knudsen, K. Schulte, J. N. Andersen, M-L. Bocquet, and J. Schnadt. *Comparison of the Carbonyl and Nitrosyl Complexes Formed by Adsorption of CO and NO on Monolayers of Iron Phthalocyanine on Au(111).* J. Phys. Chem. C 2011, **115**, 24718−24727.

[106] C. Isvoranu, B. Wang, E. Ataman, K. Schulte, J. Knudsen, J. N. Andersen, M-L. Bocquet, and J. Schnadt. *Ammonia adsorption on iron phthalocyanine on Au(111): Influence on adsorbate-substrate coupling and molecular spin.* J. Chem. Phys. 2011, **134**, 114710.

[107] M. Scardamaglia, S. Lisi, Silvano Lizzit, A. Baraldi, R. Larciprete, C. Mariani, and M. G. Betti. *Graphene-Induced Substrate Decoupling and Ideal Doping of a Self-Assembled Iron-phthalocyanine Single Layer.* J. Phys. Chem. C 2013, **117**, 3019−3027.

[108] J. D. Baran, J. A. Larsson, R. A. J. Woolley, Yan Cong, P. J. Moriarty, A. A. Cafolla, K. Schulte, and V. R. Dhanak. *Theoretical and experimental comparison of SnPc, PbPc, and CoPc adsorption on Ag(111).* Phys. Rev. B 2010, **81**, 075413.

[109] M. Bazarnik, J. Brede, R. Decker, R. Wiesendanger. *Tailoring Molecular Self-Assembly of Magnetic Phthalocyanine Molecules on Fe- and Co-Intercalated Graphene.* ACS Nano 2013, **7**, 11341−11349.

[110] F. Sedona, M. Di Marino, D. Forrer, A. Vittadini, M. Casarin, A. Cossaro, L. Floreano, A. Verdini, M. Sambi. *Tuning the Catalytic Activity of Ag(110)-Supported Fe Phthalocyanine in the Oxygen Reduction Reaction.* Nat. Mater. 2012, **11**, 970−977.

[111] Z. H. Cheng, L. Gao, Z. T. Deng, N. Jiang, Q. Liu, D. X. Shi, S. X. Du, H. M. Guo, H.-J. Gao. *Epitaxial Growth of Iron Phthalocyanine at the Initial Stage on Au(111) Surface.* J. Phys. Chem. C, 2007, **111**, 2656-2660.

[112] N. Neé l, M. Lattelais, M. L. Bocquet, J. Kröger. *Depopulation of Single-Phthalocyanine Molecular Orbitals upon Pyrrolic-Hydrogen Abstraction on Graphene.* ACS Nano 2016, 10, 2010−2016.

[113] T. Sakakura, J.-C. Choi, H. Yasuda. *Transformation of carbon dioxide.* Chem. Rev. 2007, **107**, 2365−87.

[114] W. Wang, S. Wang, X. Ma, J. Gong. *Recent advances in catalytic hydrogenation of carbon dioxide.* Chem. Soc. Rev. 2011, **40**, 7, 3703−3727.

[115] G. Centi, S. Perathoner. *Opportunities and prospects in the chemical recycling of carbon dioxide to fuels.* Catal. Today 2009, **148**, 191−205.

[116] W. Taifan, J.F. Boily, J. Baltrusaitis. *Surface chemistry of carbon dioxide revisited.* Surf. Sci. Rep. 2016, **71**, 4, 595−671.

[117] J. Shen, M. J. Kolb, A. J. Göttle, and M. T. M. Koper. *DFT Study on the Mechanism of the Electrochemical Reduction of CO2 Catalyzed by Cobalt Porphyrins*. J. Phys. Chem. C 2016, **120**, 15714−15721.

[118] D. Santos-Carballal, A. Roldan, NY. Dzade, NH. de Leeuw. *Reactivity of CO_2 on the surfaces of magnetite (Fe_3O_4), greigite (Fe_3S_4) and mackinawite (FeS)*. Phil. Trans. R. Soc. 2017, **A376**.

[119] R.J. Hooley. *Biomimetic catalysis: Taking on the turnover challenge*. Nat. Chem. 2016, **8**, 202−204.

[120] S. Tongming, Q. Zuzeng, H. Guan, J. Hongbing, J. Yuexiu, C. Jianhua. *Density functional theory study on the interaction of CO_2 with Fe_3O_4(111) surface*. Appl. Surf. Sci. 2016, **378**, 270−276.

[121] S. K. Iyemperumal and N. A. Deskins. *Activation of CO_2 by supported Cu clusters*. Phys. Chem. Chem. Phys. 2017,**19**, 28788−28807.

[122] Z. Wang, J.-X. Zhao, Q. Cai. *CO2 Electroreduction Performance of Single Transition Metal Atom Supported on Porphyrin-Like Graphene: A Computational Study*. Phys. Chem. Chem. Phys. 2017, **19**, 23113−23121.

[123] I. Pletikosic, M. Kralj, P. Pervan, R. Brako, J. Coraux, A. T. NĎiaye, C. Busse, and T. Michely. *Dirac Cones and Minigaps for Graphene on Ir(111)*. Phys. Rev. Lett. 2009,**102**, 056808.

[124] R. Larciprete, S. Ulstrup, P. Lacovig, M. Dalmiglio, M. Bianchi, F. Mazzola, et al. *oxygen Switching of the Epitaxial Graphene Metal Interaction*. ACS Nano. 2012, **6**, 9551−9558.

[125] N.A. Vinogradov, K. Schulte, M.L. Ng, A. Mikkelsen, E. Lundgren, Ma, N. M artensson, and A. B. Preobrajenski. *Impact of atomic oxygen on the structure of graphene formed on Ir(111) and Pt(111)*. J. Phys. Chem. C 2011, 115, 9568−9577.

[126] K. Schulte, N.A. Vinogradov, M.L. Ng, N. Mårtensson, A.B. Preobrajenski. *Bandgap formation in graphene on Ir(1 1 1) through oxidation*. Appl. Surf. Sci. 2013, **267**, 74−76.

[127] J. Bartolomé, C. Monton, I. K. Schuller. *Magnetism of metal phthalocyanines*, Molecular Magnets, Springer 2014, 221-245.

[128] J. F. Kirner, W. Dow, and W. Robert. Scheidt. *Molecular stereochemistry of two intermediate-spin complexes. Iron(II) phthalocyanine and manganese(II) phthalocyanine*. Inorg. Chem. 1976, **15**, 1685−1690.

[129] M.S. Liao, S. Scheiner. *Electronic structure and bonding in metal phthalocyanines, Metal=Fe, Co, Ni, Cu, Zn, Mg*. J. Chem. Phys. 2001, **114**, 9780-9791.

[130] Y. Wang, H. Yuan, Y. Li, Z. Chen. *Two-Dimensional Iron-Phthalocyanine (Fe-Pc) Monolayer As a Promising Single-Atom-Catalyst for oxygen Reduction Reaction: A Computational Study*. Nanoscale 2016, **27**, 11633−41.

[131] G. Herzberg. *Infrared and Raman spectra.*Van Nostrand, New York 1945.